Dynamics of three-dimensional excitation waves

Dissertation

zur Erlangung des akademischen Grades

doctor rerum naturalium

(Dr. rer. nat.)

genehmigt durch die Fakultät für Naturwissenschaften
der Otto-von-Guericke-Universität Magdeburg

von   **M.Sc. Chaiya Luengviriya**

geb. am   15.02.1973   in   Bangkok, Thailand

Gutachter: Prof. Dr. Marcus Hauser

                       Prof. Dr. Kenneth Showalter

eingereicht am: 28.04.2008

verteidigt am: 03.11.2008

Acknowledgements

Finally, I express my gratitude to my family for their encouragement and support throughout my study.

<div style="text-align: right">Chaiya Luengviriya</div>

Abstract

The dynamics of scroll waves and scroll rings in a three-dimensional (3D) excitable chemical medium, the Belousov-Zhabotinsky (BZ) reaction, have been studied. Note that scroll rings are scroll waves with a ring-shaped filament. The investigation is devided into two parts. In part I, two kinds of scroll wave instabilities in homogeneous excitable media, namely 3D meandering and negative line tension instabilities, were studied. In part II, a study of the external control of the dynamics of scroll rings is presented. The control was achieved by an applied electrical current.

Part I: Scroll wave instabilities

Experiments on the dynamics of scroll waves in the BZ reaction have been carried out in an optical tomography setup. This allows for the reconstruction of the 3D structures of the scroll waves and their filament. Using a chemical recipe where the BZ reaction shows meandering waves, the scroll waves with an initially straight filament adopted a flat zig-zag form of constant length. This deformation describes a 3D meandering instability. In this closed system, the reagents were continuously consumed so the system aged. Thus, the second kind of instability, the negative line tension instability, emerged in the long time limit, i.e., at low excitability. Here the filament lengthened substantially and the scroll wave assumed a snaking geometry. Numerical simulations using the generic Barkley model that takes into account the decrease in excitability of the reaction medium due to ageing corroborate the experimental findings and their interpretation.

Part II: Scroll rings in an advective field

In the absence of any external field, scroll rings in the BZ reaction contracted and subsequently self-annihilated at approximately the same orientation and location. The scroll rings were forced to reorient by an applied electrical current, except for two cases – the parallel and anti-parallel orientations, where the orientation is the angle θ between the scroll ring unit vector and the applied current. The parallel orientation ($\theta = 0°$) is unstable against perturbations while the anti-parallel orientation ($\theta = 180°$) is a stable stationary state. The influence of an applied electrical current on the lifetime of scroll rings depends on the initial alignment (θ_0) of the scroll rings. When $0° \leq \theta_0 < 90°$, the lifetime of the scroll rings was shortened otherwise prolonged, compared to that in the absence of electrical current. At the stable stationary orientation ($\theta = 180°$), small scroll rings still contracted, however, larger scroll rings expanded under a given applied current. Numerical simulations using the Oregonator model with an additional advective term accounting for the electric field reproduced the experimental results and provided insights on the deformation of the structure of the filament during the reorientation. Delicate adjustments caused a scroll ring to propagate with a constant radius in an advective field.

Zusammenfassung

Gegenstand der vorliegenden Dissertation ist die Untersuchung von grundlegenden Aspekten der Dynamik von dreidimensionalen (3D) Mustern in erregbaren Systemen. Im Gegensatz zur Musterbildung in erregbaren Systemen in zwei Dimensionen (2D) ist die Musterbildung in 3D experimentell kaum untersucht. Dabei ist die Dynamik von räumlich und zeitlich ausgedehnten Systemen in 3D deutlich vielfältiger als in 2D. Neben der dynamischen Vielfalt in 3D kommt 3D-Untersuchungen von erregbaren Systemen eine wichtige physiologische Rolle zu, da 3D Erregungsstrukturen (die sog. Scroll-Wellen) und deren Instabilitäten als Auslöser für gewisse Arten von Herzrhythmusstörungen (wie dem Hauptkammerflattern und Hauptkammerflimmern) gelten, die zu plötzlichem Herztod führen können.

In der Dissertation wird die Dynamik von Scroll-Wellen und Scroll-Ringen untersucht. Eine Scroll-Welle ist eine dreidimensionale Erweiterung einer Spiralwelle, die in 2D ausgiebig untersucht worden ist. Das Oragnisationszentrum der Scrollwelle ist das Filament, das die Spitzen der einzelnen Spiralen eines Spiralenstapels verbindet. Scroll-Ringe sind Scroll-Wellen, deren Filamente geschlossen sind.

Für gerade Scrollwellen sind aus theoretischen Betrachtungen und numerischen Simulationsrechnungen drei unterschiedliche Instabilitäten vorhergesagt, nämlich die verdrillungsinduzierte Instabilität (twist-induced instability), die 3D-Mäanderinstabiltät und eine Instabilität, die durch das Auftreten einer negativen Linienspannung auftritt (negative line tension instability). Von diesen drei Instabilitäten wurde nur die erste bereits experimentell nachgewiesen; der Nachweis der verbleibenden zwei Instabilitäten ist Gegenstand des ersten Teils der vorliegenden

Arbeit.

Im <u>ersten Teil</u> der Promotionsarbeit werden die 3D-Mäanderinstabilität und die negative Linienspannungs-Instabilität experimentell nachgewiesen. Als erregbares Modellsystem wird die Belousov-Zhabotinsky-Reaktion in einem zylinderförmigen Reaktor mittels optischer Tomographie untersucht. Aus den tomographischen Projektionen wird die dreidimensionale Struktur der Scrollwellen rekonstruiert und deren Filamente ermittelt. Während der Reaktion altert die Reaktionslösung, d.h. ihre Erregbarkeit nimmt ständig ab. Nach ca. 3 Stunden beobachtet man, dass das ursprünglich gerade Filament sich zick-zack-förmig verformt während dessen Länge in etwa konstant bleibt. Dies deutet auf das Auftreten der 3D-Mäanderinstabiltät hin. Gegen Ende der Experimente (nach ca. 8 Stunden) ist die Erregbarkeit des geschlossenen Reaktionssystems deutlich abgesunken und es kommt zur negative Linienspannungs-Instabilität. Diese zeichnet sich dadurch aus, dass das Filament sich plötzlich und kontinuierlich ausdehnt und sich dabei verdrillt. Ein ähnliches Szenario wird auch in numerischen Simulationsrechnungen gefunden, die am Barkley-Modell durchgeführt wurden. Dabei wird das Altern der Reaktionslösung als Abnahme der Erregbarkeit des Systems modelliert. Die gute Übereinstimmung von experimentellen und numerischen Ergebnissen unterstreicht das Auftreten der 3D-Mäanderinstabilität und der negativen Linienspannungs-Instabilität in unserem chemischen Modellsystem. Damit konnten diese Instabilitäten unseres Wissens erstmalig experimentell nachgewiesen werden.

Im <u>zweiten Teil</u> dieser Arbeit wird über die Ergebnisse einer experimentellen und numerischen Untersuchung der Dynamik von Scrollringen, die einem externen Strom ausgesetzt sind, berichtet. In Abwesenheit des externen Feldes schrumpfen die Scrollringe und löschen sich schliesslich aus, wobei ihre Lage und Orientierung im Reaktor unverändert bleiben.

Wird ein Gleichstrom an das Reaktionsmedium mit den Scrollringen angelegt, so driften die Scrollringe immer in Richtung Anode. Der angelegte Gleichstrom bewirkt eine Drehung der Scrollringe, wobei sich ihre Einheitsvektoren schliesslich entgegengesetzt zu der Stromflussrichtung anordnen (d.h. der Winkel zwischen dem Einheitsvektor des Scrollrings und dem Vektor des Stromflusses ist $\theta = 180°$).

Es wurde gezeigt, dass diese antiparallele Anordnung zum Stromfluss eine stabile stationäre Orientierung darstellt. Die parallele Anordnung von Stromflussrichtung und Einheitsvektor der Scrollringe ($\theta = 0°$) ist ebenfalls ein stationärer Zustand, der jedoch instabil ist, da kleine Abweihungen von der parallelen Anordnung dazu führen, dass sich die Scrollringe umorientieren und sich letztendlich entgegengesetzt zur Stromflussrichtung anordnen (falls sie sich nicht vorher - wegen ihrer intrinsischen Kontraktion - auf dem Weg dahin selbst auslöschen).

Der angelegte Strom hat ebenfalls einen Einfluss auf die Lebensdauer der Scrollringe, wobei der Effekt von der anfänglichen Orientierung des Scrollrings (d.h. vom Winkel θ_0) abhängt. Für $90° \leq \theta_0 \leq 180°$ kommt es zu einer Verlängerung der Lebensdauer der Scrollringe im Vergleich zur ihrer Lebensdauer im ungestörten Fall. Für Anfangswinkel $0° \leq \theta_0 < 90°$ verkürzt sich hingegen die Lebensdauer der Scrollringe.

Betrachtet man das Schicksal von Scrollringen, die antiparallel zur Stromrichtung angeordnet sind ($\theta = 180°$), bei einer konstanten Stromdichte in Abhängigkeit des Durchmessers der Scrollringe, so stellt man fest, dass kleine Scrollringe schrumpfen während grosse anwachsen. Damit exisitert auch ein kritischer Radius r_c, bei dem sich Scrollringe mit zeitlich unveränderten Filamenten ausbilden. Dieser kritische Radius trennt die Domänen von schrumpfenden ($r < r_c$) und anwachsenden ($r > r_c$) Scrollwellen voneinander.

Es wurde experimentell gezeigt, dass sich die Dynamik von Scrollringen kontrollieren lässt. Dazu wurde ein antiparallel zur Stromrichtung angeordneter Scrollring (d.h. $\theta = 180°$) beobachtet. Bei niedrigen Stromdichten kontrahiert der Ring intrinsisch, während er sich bei ausreichend hohen Stromdichten ausweitet. Neben dem Durchmesser des Rings kann auch seine Lebensdauer extern beeinflusst werden. Diese Experimente zeigen, dass ein externer Stromfluss zur kontrollierten Manipulation von Scrollringen verwendet werden kann. Dies eröffnet weitreichende Möglichkeiten für zukünftige Experimente.

Das experimentell beobachtete Verhalten von Scrollringen im elektrischen Strom stimmt gut mit den durchgeführten Simulationsrechnungen überein. Als Modellsystem für die Belousov-Zhabotinksy-Reaktion wurde der sog. Oregonator verwen-

det und das Reaktions-Diffusions-Gleichungssystem mit Advektionstermen versehen, die den Einfluss des Stroms auf die ionischen Komponenten des Reaktionssystems beschreiben. Zusätzlich zur Reproduktion der experimentellen Ergebnisse konnten in den Simulationsrechnungen Scrollwellen mit zeitlich konstantem Radius erhalten werden. In diesem Fall wirkt der Effekt des Stromes der intrinsischen Kontraktion der Scrollwellen genau entgegen. Wie für ein Bifurkationspunkt üblich, ist der kritische Radius r_c gegenüber Störungen instabil.

Contents

I　Scroll wave instabilities　　　　　　　　　　53

5　Methods　　　　　　　　　　　　　　　　　55

6　Results and Discussion　　　　　　　　　　69

II　Scroll rings in an advective field　　　　83

7　Methods　　　　　　　　　　　　　　　　　85

List of Figures

List of Tables

Chapter 1

Introduction and goals

Pattern formation is common in nature. Patterns can be observed everywhere around us ranging from physical, chemical, to biological systems such as clouds, sand, water, chemical reactions, skin of animals and plants, etc. Modern research on pattern formation is usually associated with the publication "The Chemical Basis of Morphogenesis" by the mathematician Alan Turing [1] in 1952. It is one of the most influential works on self-organization in non-equilibrium systems. In the theory, morphogenetic patterns, including stationary and travelling waves, develop due to an instability of the initial homogeneous state triggered by random disturbances. In fact, they are derived from reactions of chemical substrates coupling with diffusion. Such reaction-diffusion systems are used to describe phenomena occuring in excitable media. These media can be characterized by three states: The excitable state is stable to small perturbations, however, perturbations larger than a threshold induce a pronounced response by the system, which becomes excited. Subsequently, the system relaxes through an unexcitable refractory state and becomes excitable again. In distributed systems, the excitations spread as travelling waves.

Travelling excitation waves known as spiral waves, which are extremely robust spatiotemporal self-organizing patterns, are generally exhibited in thin layers (in two dimensions, 2D) of many different excitable media as shown in Fig. 1.1(a)–(f): (a) a single crystal platinum single crystal surface, (b) the Belousov-Zhabotinsky
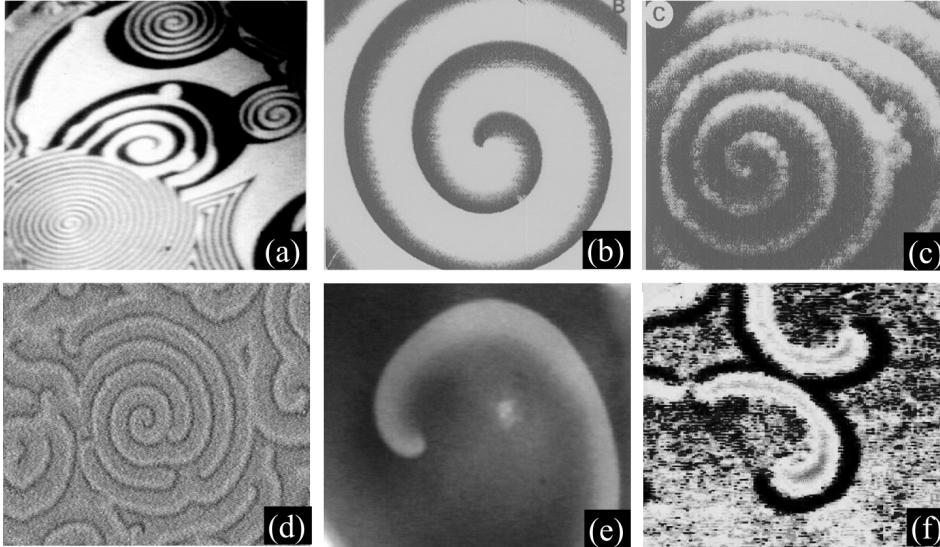
Figure 1.1: Rotating spiral waves in various excitable media: (a) Spiral waves in the catalytic CO-oxidation on a platinum single crystal surface [2], (b) spiral waves in the BZ reaction [3], (c) Ca^{2+} waves in *Xenopus laevis* oocyte [4], (d) aggreation patterns of the slime mould *Dictyostelium discoideum* [5], (e) spreading depression waves on chicken retina [6], (f) spiral waves propagating during glycolysis in yeast extract [7].
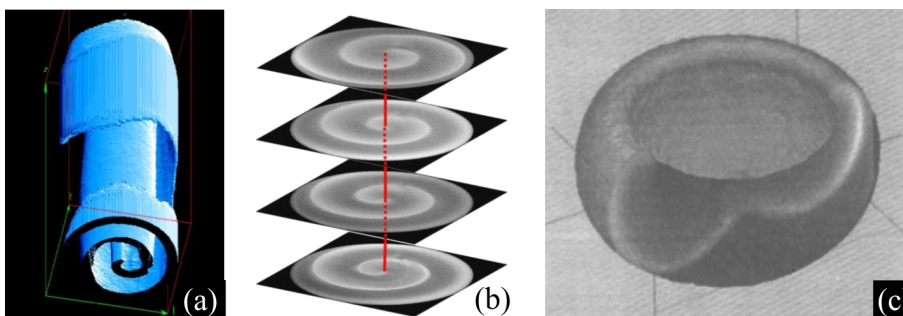
Figure 1.2: Scroll waves in the Belousov-Zhabotinsky reaction. 3D wave structures were observed using optical tomography. (a) A straight scroll wave whose (b) filament is linear [8]. (c) When the filament forms a closed loop, the structure is called scroll ring [9].

(BZ) reaction, (c) *Xenopus laevis* oocytes, (d) the cell aggregation of the slime mould *Dictyostelium discoideum*, (e) chicken retina, and (f) yeast extract. Even though they occur in very different systems, the wave patterns are governed by similar reaction-diffusion mechanisms. The BZ reaction is one of the most popular model systems to study the dynamics of wave patterns experimentally because of both its easy preparation and the convenient detection of the wave patterns in this reaction system.

In three dimensions (3D), analogous forms to spiral waves are called scroll waves. In these 3D cases, the organizing centers of the wave patterns extend from a point of the spiral tip (for the 2D cases) to a line of filament around which the scroll waves rotate [10, 11, 12]. A straight scroll wave [Fig. 1.2(g)] whose filament is linear [Fig. 1.2(h)] is the simplest structure. When the filament forms a closed loop (e.g., a circle) the scroll wave is called a "scroll ring" [Fig. 1.2(i)]. Dynamics of scroll waves are of interest due to their intrinsic complication and elegance. Furthermore, it is conjectured that scroll waves of electrical excitation in heart and their instabilities are involved in causing certain types of cardiac arrhythmia [13], such as ventricular tachycardia and fibrillation which can potentially lead to a sudden cardiac death.

Figure 1.3 illustrates the electrocardiogram and its corresponding electrical signals at different dynamic states. In a normal situation, the sinus node emits electrical signals, which propagate as truncated form of spherical waves, causing muscular contraction. In response to unusual stimuli, e.g., dead cells, the muscle contract is driven pathological ways by scroll waves which are found to have a frequency ≈ 4 times higher than that in the normal state [14, 15, 16]. If the waves are subjected to instabilities leading to spiral turbulence, the heart contracts in an uncoordinated fashion and it cannot effectively pump blood to the body anymore. Many experiments (reviewed in reference [17]) provide support that rotating waves in mammalian heart may be essentially 3D phenomena. In addition, thin cuts of cardiac tissues did not exhibit wave turbulence [13] which derived from scroll wave instabilities. Therefore, a good understanding of both the dynamics and the instabilities of scroll waves, is particularly important in order to avoid or to
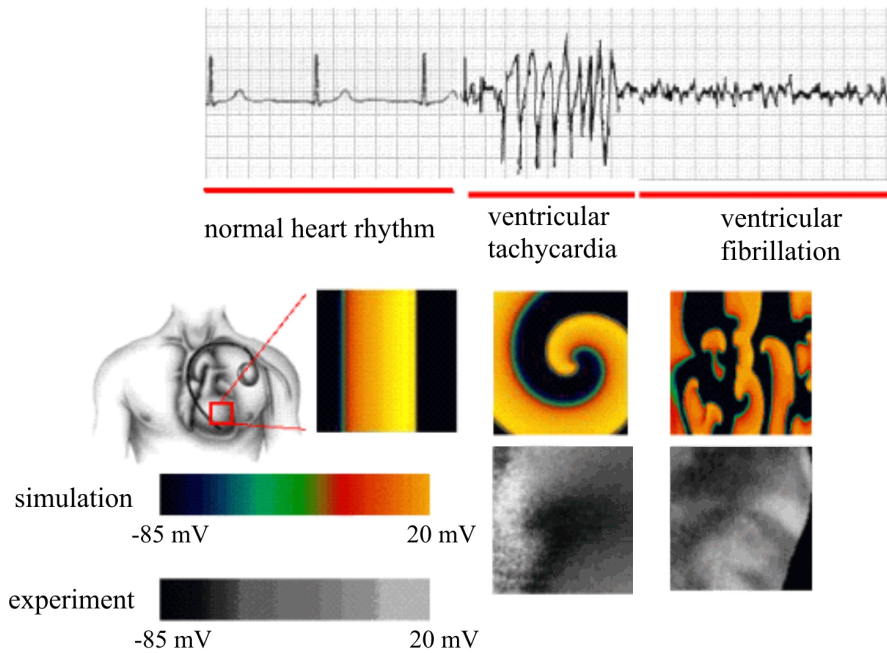
Figure 1.3: Electrical signals in the ventricle of the heart during normal, tachycadia, and fibrillation states [19]. From top to bottom rows: electrocardiogram (EEG), simulations of electrical waves [15, 16], and experiments on electrical waves on the ventricular surface of rabbit and sheep [14]. For normal heart rhythm, electrical waves, produced by the pacemaker, spread throughout the heart and induce heart contractions. These waves normally occur about every 0.8 s. When a spiral wave of electrical activity occurs in the heart, its period is generally about 0.2 s which can produce fast oscillations corresponding to an arrhythmia called tachycardia, which often directly precedes the onset of fibrillation. Multiple spiral waves (turbulence), produced by the breakup of a spiral wave, lead to the fast irregular oscillations characteristic of fibrillation.

suppress such cardiac arrhythmias. Probably due to this impact to humans, control of both 2D spiral waves and 3D scroll waves and suppression of the wave turbulence [18] have been being topics investigated widely over the last two decads.

In theory, scroll waves instabilities were predicted in different situations. The wave instabilities can be caused by the anisotropy of the excitable media such as fiber rotation in heart structures [20, 21, 22, 15, 16, 23, 24]. However, bifurcation analysis and numerical simulations showed that three kinds of scroll waves instabilities – 3D meandering, negative line tension, and twist-induced instabilities – can occur in homogeneous media. The first aim of our study is to investigate the existence of scroll wave instabilites in experiments using a homogeneous BZ

medium.

The control of scroll wave dynamics and suppression of 3D wave turbulence are particular important in solving problems of cardiac arrhythmias. Experiments in this direction, however, are so far scant. Our second aim is therefore to investigate the dynamics of scroll rings in the ionic BZ reaction subjected to an external electrical forcing. We chose scroll rings due to their simple structure and well-known intrinsic dynamics while both direction and strength of the electrical current can be rapidly changed giving possibilities for very efficient manipulations.

In this thesis, we present a research work on the intrinsic dynamics and external forcing of 3D excitation waves in the BZ reaction. To better account for the different types of studies conducted with scroll waves and scroll rings, we divided the description of the experimental methods and results into two parts. Part I deals with our findings on scroll waves instabilities, i.e., deformations of initial straight scroll waves. 3D wave patterns were observed by optical tomography. The reconstruction of the scroll waves and the evaluation of their filaments, i.e., the organizing center, were utilized to characterize different types of the observed instabilities. Numerical simulations using a generic model, namely the Barkley model [25, 26], for excitable media reproduced qualitatively the 3D instabilities found in the experiments.

Part II reports on an investigation of scroll ring dynamics under an applied electrical forcing. Due to the necessity to apply an electrical current to the scroll rings, we have simplified the monitoring technique: The scroll rings were only observed from the top and lateral projections of the system instead of using the complicated optical tomography. Finally, we reproduced these experiments using the Oregonator model with an additional advective term accounting for the applied electric field.

Chapter 2

Active media

In this chapter, we review some important properties of active media including excitable media which we used in our work. As an example of active media in the real world, the Belousov-Zhabothinsky reaction and its related model are described. This is, in fact, the excitable medium investigated in the present thesis.

2.1 Reaction-diffusion mechanism

Active media are often described using a system of two-variable differential equations:

$$
\begin{aligned}
\frac{\partial u}{\partial t} &= \frac{f(u, v)}{\epsilon} + D_u \nabla^2 u, \\
\frac{\partial v}{\partial t} &= g(u, v) + D_v \nabla^2 v,
\end{aligned}
\tag{2.1}
$$

where u and v are called "activator" and "inhibitor" (or "controller") variables, respectively. $f(u, v)$ and $g(u, v)$ describe the kinetics of the reaction system. The parameter $\epsilon << 1$ which accounts for the markedly different characteristic timescales of the two variables u and v. ∇^2 is the Laplacian operator, D_u and D_v are diffusion coefficients of u and v, respectively. In the Oregonator model (see the next section for details) for the BZ reaction, bromous acid, $HBrO_2$, plays the role of the activator while the oxidized form of the metal-ion catalyst is the controller (u and v correspond to the concentration of $HBrO_2$ and the catalyst). In the FitzHugh-

6
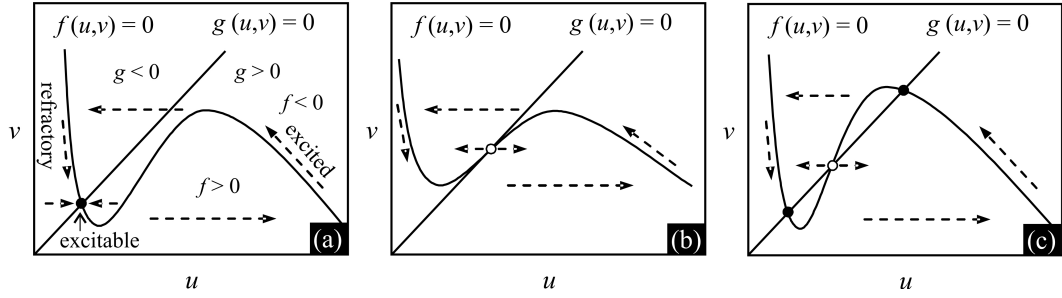
Figure 2.1: Phase diagram of local dynamics in active media. Curves and straight lines represent the u-nullcline ($f(u, v) = 0$) and the v-nullcline ($g(u, v) = 0$), respectively. Arrows indicate the direction of the dynamics. (a) Excitable media have a steady state (filled circle) which is located alone to the unstable manifold. The steady state is stable to any perturbation smaller that a theshold. A sufficiently large perturbation leads to an overshoot of u and the system is in an excited state. Before the system recovers to the excitable state, it stays in a refractory state where the system is unexcitable. (b) For oscillating media, the only one stationary state of the dynamics is unstable (open circle) so, except for this state, u and v always oscillate. (c) For bistable media, there are three fixed states, one unstable in between two others stable. The system switches from one stable state to another when a perturbation is applied.

Nagumo model [27, 28] for a nerve axon, the membrane potential and the ionic conductance play the roles of the activator and the inhibitor, respectively. The idea is also implemented in generic models such as the Barkley model [25, 26].

Active media can be classified as excitable, oscillating, and multi-stable. Figure 2.1 illustrates the local dynamics of the two variables when the reaction terms $f(u, v)$ and $g(u, v)$ are cubic and linear functions, respectively. The fast variable, the activator u, has a u-nullcline ($f(u, v) = 0$, i.e., $du/dt = 0$) consisting of three branches with a maximum and a minimum while the slow controller v has a linear v-nullcline ($g(u, v) = 0$, so $dv/dt = 0$). The intersections between the two nullclines are the stationary solutions (both u and v do remain unchanged). Now we consider the dynamics of the variables in the phase diagram as indicated by the arrows (Fig. 2.1). In the domain under the u-nullcline, $f > 0$ so u always increases. By contrast, when the state of the system is located above the u-nullcline, $f < 0$ and u always decreases. Similarly, in the domain at the right of the v-nullcline, $g > 0$ and v increses but the left of the v-nullcline, $g < 0$ and v decreases. The changes of u and v in different domains specify the trajectory in the system state (u, v) as

shown by the arrows.

For excitable media [Fig. 2.1(a)], the stationary state is stable. It is called *excitable state* since a small perturbation of u from this point would decay, however, a perturbation larger than a theshold results in an overshoot of u and the system is in an *excited state*. The system makes a great excursion through the phase space. Before recovering to the excitable state, the system is in an unexcitable *refractory* in which no further excitation can occur. In the oscillating case [Fig. 2.1(b)], an intersection of the nullclines occurs on the middle branch of u-nullcline and the fixed point is unstable. Except for this single point, both u and v oscillate all time. In contrast, there are three fixed states for bistable media [Fig. 2.1(c)]. Again, the stationary point on the middle branch is unstable. The two others are stable. A sufficient perturbation will cause u and v to change and the system switchs from one stationary state to the other.

In spatially extended media, travelling waves of excitation result from the coupling of local dynamics (described above) and the diffusion process. From a point with high concentration, u spreads and excites the neighbors causing a propagation of the excitation. Unlike other kinds of waves, e.g., sound and light, the excitation waves propagate without attenuation of amplitude. Moreover, waves annihilate upon collision, thus no interference of waves occurs. The wave velocity increases with the period – the longer period allows the system to recover closer to the excitable state – yielding a *dispersion relation* [29, 30]:

$$c(T) = c_0 \tanh\left(T/T^*\right),\tag{2.2}$$

where $c(T)$ is the wave velocity at period T while c_0 is the velocity of a single pulse $(T \to \infty)$ travelling in an absolute excitable media. T^* is the possible shortest period which waves can propagate in the excitable media.

Furthermore, it is found theoretically [31, 32] and experimentally [33] that the wave velocity $c(\kappa)$ depends on the shape of wave fronts (represented by the

curvature) as described by the *eikonal equation*:

$$c(\kappa) = c_0 - D_u \kappa, \tag{2.3}$$

where $c(\kappa)$ is the velocity of the curved wave front with a curvature κ while and c_0 is the velocity of a planar wave front. D_u is the diffusion coefficient of the propagator u. Due to this curvature effect, a concave wave propagates faster than a convex wave. For a given distance from the front, a thin area in front of the convex wave is larger so it takes a longer time until the points in this area becomes excited.

In three dimensions, excitation waves propagate as fronts of surface and their local velocity determined by the eikonal equation [34]:

$$c(\kappa) = c_0 - D_u \left(\kappa + \tau \right), \tag{2.4}$$

where κ and τ are, respectively, curvature and torsion which is defined clearly in section 4.2.

2.2 The Belousov-Zhabotinsky reaction

In this section, we consider an excitable chemical medium – the Belousov-Zhabotinsky reaction and its corresponding mathematical model – the Oregonator model, which have been used in our study.

The name Belousov-Zhabotinsky (BZ) reaction was coined after two russian scientists who discovered the interesting dynamics of the reaction. During his research on the Krebs cycle, B.P. Belousov discovered that at very low pH (pH $\leq$ 1) the color of the reaction of citric acid (with acidified bromate and ceric ions as catalyst) oscillated between colorless and yellow for an hour. In 1951, Belousov wrote an article describing this reaction, however, it was rejected. His work appeared only as an abstract in a symposium [35]. At that time, scientists believed that oscillations in closed homogeneous systems were impossible because that would

imply that the reaction did not go to thermodynamic equilibrium smoothly. In fact, the system does not reach a stable state while it oscillates but it does drift slowly to the equilibrium, where the oscillation ceases. In 1962, A.M. Zhabotinsky [36] continued the work of Belousov. He modified the reaction by replacing citric acid by malonic acid ($CH_2(COOH)_2$). Since then the BZ reaction was improved for specific purposes. By changing the catalyst from cerium to ferroin, oscillations and propagating waves in the BZ reaction can be observed much earsier due to better contrast images. When the ruthenium(II)-tris(2,2'-bipyridyl) complex is utilized as the catalyst, the reaction is photosensitive [37, 38] opening possibilities for external control and perturbation by light.

In 1972, Field, Körös, and Noyes [39] proposed a reaction mechanism, now known as FKN mechanism, for the temporal oscillations in the BZ reaction. The overall reaction reads

$$2BrO_3^- + 3CH_2(COOH)_2 + 2H^+ \rightarrow 2BrCH(COOH)_2 + 3CO_2 + 4H_2O. \quad (2.5)$$

The skeleton mechanism is divided into three groups of reactions labelled as Processes A, B, and C as shown in Table 2.2.

The number of chemical processes in the BZ reaction is very large. However, from the dynamic point of view, the most important chemical species involved in the chemical oscillations (and wave propagations) are $HBrO_2$, Br^-, and the oxidized catalyst, Cat_{ox}, acting as activator, inhibitor, and controller, respectively. Their concentrations, $[HBrO_2]$, $[Br^-]$, and $[Cat_{ox}]$ change through out three processes, namely, process A, B, and C as in (Table 2.2). The effect of process A is to decrease $[Br^-]$ and to regulate $[HBrO_2]$. When $[Br^-]$ is low enough, process B, the autocatalytic process (i.e., $HBrO_2$ which is a product in reaction (3) is also a reactant), begins so that $[HBrO_2]$ and $[Cat_{ox}]$ increase rapidly. Process B stops when almost all of the catalyst is oxidized. The Cat_{ox} then becomes a reactant in process C to generate Br^- and the reduced form of the catalyst, Cat_{re}. When sufficient $[Br^-]$ is produced, and almost the entire catalyst is in the reduced form, process C stops and process A starts again. All processes repeat

Table 2.1: The FKN mechanism of the Belosov-Zhabotinsky reaction [39].

Process A

$$BrO_3^- + Br^- + 2H^+ \rightleftharpoons HBrO_2 + HOBr \qquad (1a)$$
$$HBrO_2 + Br^- + H^+ \rightarrow 2HOBr \qquad (1b)$$
$$3(HOBr + Br^- + H^+ \rightleftharpoons Br_2 + H_2O) \qquad (1c)$$

$$BrO_3^- + 5Br^- + 6\,H^+ \rightarrow 3Br_2 + 3H_2O \qquad (1)$$
$$3(Br_2 + CH_2(COOH)_2 \rightarrow BrCH(COOH)_2 + Br^- + H^+ \qquad (2)$$

$$BrO_3^- + 2Br^- +$$
$$3CH_2(COOH)_2 + 3H^+ \rightarrow 3BrCH(COOH)_2 + 3H_2O \qquad (1+2)$$

Process B

$$BrO_3^- + HBrO_2 + H^+ \rightleftharpoons 2BrO_2^\bullet + H_2O \qquad (3a)$$
$$2(BrO_2^\bullet + Cat_{re} + H^+ \rightleftharpoons HBrO_2 + Cat_{ox} \qquad (3b)$$

$$2(BrO_3^- + HBrO_2 + 2Cat_{re} + 3H^+ \rightleftharpoons 2HBrO_2 + 2Cat_{ox} + H_2O) \qquad (3)$$
$$2HBrO_2 \rightarrow HOBr + BrO_3^- + H^+ \qquad (4)$$

$$BrO_3^- + 4Cat_{re} + 5H^+ \rightleftharpoons HOBr + 4Cat_{ox} + 2H_2O \qquad (3+4)$$

Process C

$$HOBr + 2CH_2(COOH)_2 +$$
$$2Cat_{ox} + BrCH(COOH)_2 + 2H_2O \rightarrow 2Cat_{re} + 3HOCH(COOH)_2 +$$
$$2Br^- + 4H^+ \qquad (5)$$

Table 2.2: The Oregonator model of the Belosov-Zhabotinsky reaction [40]. A = BrO_3^-, B = $BrCH(COOH)_2 + CH_2(COOH)_2$, P = HOBr, U = $HBrO_2$, V = Cat_{ox}, W = Br^-. k_1 to k_5 are rate constants and f is a stoichiometric factor.

Oregonator model	FKN mechanism	characteristic dynamics
Process A		
A + W $\xrightarrow{k_1}$ U + P	(1a)	slow reaction
U + W $\xrightarrow{k_2}$ 2P	(1b)	fast reaction, when low [$HBrO_2$]
Process B		
A + U $\xrightarrow{k_3}$ 2U + 2V	(3)	autocatalysis of $HBrO_2$
2U $\xrightarrow{k_4}$ A + P	(4)	limitation of [$HBrO_2$]
Process C		
B + V $\xrightarrow{k_5}$ f W	(5)	regeneration of Br^-

periodically leading to oscillations, however, the reactants are gradually converted to the products as shown in the overall reaction. Ultimately, the oscillations die out and the system approaches chemical equilibrium.

2.3   The Oregonator model

Based on the FKN mechanism, Field and Noyes [40] proposed a simplified version called the Oregonator (after their working place, the University of Oregon). The model contains 5 reactions and 6 chemical components as shown in table 2.3.

The dynamics of the activator U, the inhibitor W, and the controller V are obtained by applying the law of mass action to the reactions (1a) – (5). Their concentrations change with time as

$$
\begin{aligned}
\frac{dU}{dt} &= k_1AW - k_2UW + k_3AU - 2k_4U^2, \\
\frac{dW}{dt} &= -k_1AW - k_2UW + k_5fBV, \\
\frac{dV}{dt} &= 2k_3AU - k_5BV.
\end{aligned}
\tag{2.6}
$$

The concentrations of A and B are present in large stoichiometric excess and are

therefore taken as constant. Using dimensionless variables and parameters:

$$u = \frac{2k_4}{k_3 A} U, \quad v = \frac{k_4 k_5 B}{(k_3 A)^2} V, \quad w = \frac{k_2}{k_3 A} W,$$

$$t' = k_5 B \, t, \quad \epsilon = \frac{k_5 B}{k_3 A}, \quad \acute{\epsilon} = \frac{2k_4 k_5 B}{k_2 k_3 A}, \quad \hat{f} = 2f, \quad q = \frac{2k_1 k_4}{k_2 k_3}, \tag{2.7}$$

a dimensionless version of Eq. (2.6), known as the three-variable (u, v, w) Oregonator model, reads

$$\begin{aligned}
\frac{du}{dt} &= \frac{1}{\epsilon}(qw - uw + u - u^2), \\
\frac{dv}{dt} &= u - v, \\
\frac{dw}{dt} &= \frac{1}{\acute{\epsilon}}(-qw - uw + fv),
\end{aligned} \tag{2.8}$$

with a replacement of t' and $\hat{f}$ with t and f, respectively. The parameters ϵ and $\acute{\epsilon}$ are smaller than 1. In fact, $\acute{\epsilon} << \epsilon << 1$ [41] which causes the dynamics of w to be extremely fast in comparison to the dynamics of u and v. This allows us to assume that $[Br^-]$ (w) is stationary relative to $[HBrO_2]$ (u):

$$-qw - uw + fv = \acute{\epsilon}\frac{dw}{dt} \approx 0 \tag{2.9}$$

$$w = \frac{fv}{u + q} \tag{2.10}$$

and consequently it leads to the simplified two-variable (u, v) Oregonator model as

$$\begin{aligned}
\frac{\partial u}{\partial t} &= \frac{1}{\epsilon}\left(u - u^2 - fv\frac{u - q}{u + q}\right), \\
\frac{\partial v}{\partial t} &= u - v.
\end{aligned} \tag{2.11}$$

In spatially extended systems, the BZ reaction exhibits propagating waves. For the ferroin-catalysted BZ reaction as used in our experiments, unstirred systems exhibit blue waves propagating on a red background. The phenomenon originates from the oupling of reaction with diffusion which can be modelled by a Fick diffu-

sion term. In this case, the two-variable Oregonator model reads

$$
\begin{aligned}
\frac{\partial u}{\partial t} &= \frac{1}{\epsilon}\left(u - u^2 - fv\frac{u - q}{u + q} \right) + D_u\nabla^2 u, \\
\frac{\partial v}{\partial t} &= u - v + D_v\nabla^2 v.
\end{aligned}
\tag{2.12}
$$

Chapter 3

Spiral waves and external control

3.1 Target patterns and spirals

Rotating spiral waves of excitation can be found in many excitable media as shown in Fig. 1.1. Systematic experimental studies of the spiral dynamics have been done mostly using the Belousov-Zhabotinsky (BZ) reaction [42, 43, 44, 45, 46, 47, 48]. In a thin layer of the ferroin-catalysted BZ reaction, traveling waves are visible as blue excited fronts of the oxidized state of the catalyst, ferriin. The fronts propagate through a quiescent red background which contains the reduced form of the catalyst, ferroin. The light transmission (at wavelength $\approx$ 490 nm giving the maximal difference between the fronts and the background) through the reaction layer is recorded using 2D spectophotometry [42]

Expanding circular waves triggered by a pacemaker (e.g., an impurity such as dust) are often observed in experiments using the BZ reaction. For each pacemaker, the circular waves are produced periodically yielding a target pattern [as at bottom right in Fig. 3.1(a)–(b)]. When a circular wave front is broken, e.g., by pushing an air blast from a pipette to the front, the two open ends of the front. Due to the fact that the velocity of wave front depends on the local curvature [according to the eikonal relation Eq. (2.3)], the open ends of the front, thus, curl in and form a pair of counter-rotating spiral waves [at the top left in 3.1(a)–(b)]. The position of the spiral tip is typically defined as the point of highest curvature along

15
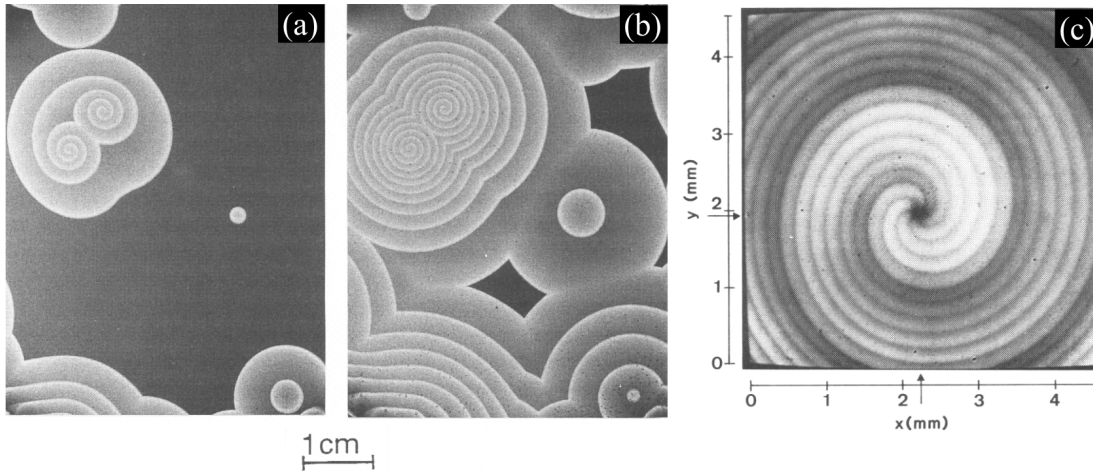
Figure 3.1: Target pattern and spiral waves in a thin layer of the BZ reaction at (a) early and (b) later stages [52]. Top left: a pair of counter-rotating spirals, bottom right: a target pattern. (c) a superposition of six subsequent images of a spiral wave [42]. The spiral core appears as a small circular dark region (at $x = 2.25$ mm, $y = 1.95$ mm) in the image.

an isoconcentration line of the spiral wave [49, 50] and the tip rotates around the spiral core which is a small quiescent area appearing as a dark region in a superposition of spiral wave images [3.1(c)]. When wave fronts collide together or reach the walls of the container, they annihilate [the line in between the two spirals in 3.1(a)–(b)] without interference or reflection.

It has been shown in both experiments and simulations that the dynamics of the spiral tip, which is the organizing center of the wave pattern, depend on the system parameters. In the simplest case, the spiral tip rotates around a circular core [3.1(c)] with a single frequency so it is called *rigidly rotating* spiral wave. The shape of a rigidly rotating spiral wave is approximatly an Archimedean spiral – in polar coordinates, the radius vector of the position on the spiral wave is a linear function of the angle. However, complicated motions of the spiral tip, so-called *meandering* [51], are more often exhibited in excitable media. The motion of the spiral tip has been systematically studied using the BZ reaction and numerical simulations as presented in the next section.
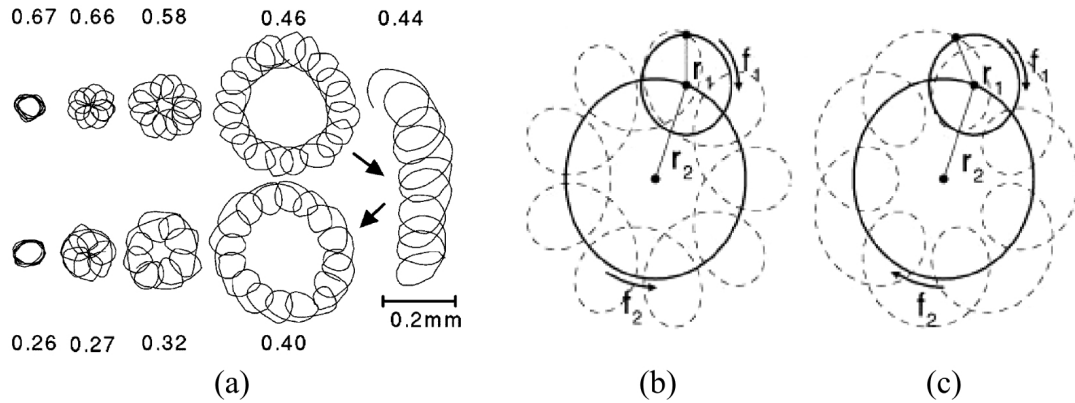
Figure 3.2: Trajectory of a ionspiral wave in the BZ reaction as a function of H_2SO_4 concentration [46]. (a) In an open system, the concentration of the reactants was kept constant except for H_2SO_4. At 0.67 M H_2SO_4, the spiral tip rotated on a circle. As the concentration of H_2SO_4 and hence also the excitability decreased, the spiral tip meandered: outward-petal meandering (0.66 – 0.46 M), travelling meandering (0.44 M), and inward-petal meandering (0.40 – 0.27 M). Finally, the spiral tip rotated on a circle at 0.26 M. The meandering patterns can be describe as (b) a hypercycloid for outward petals or (c) epicycloid for inward petals.

3.2 Meandering spirals

Experiments [43, 44, 45, 46, 47, 48] showed that the dynamics of spiral waves depend on the parameters of the excitable media. Figure 3.2(a) shows various kinds of trajectories of spiral tip in the BZ reaction [46]. The reactants were continuously fed through the reactor to keep the system at stationary conditions during the observations. The concentration of H_2SO_4 which is linked to the excitability of the system(the excitability of the system decreases with decreasing H_2SO_4 concentration) was varied stepwise during the experiments. At 0.67 M H_2SO_4, the spiral rotated rigidly around a circle. When the H_2SO_4 concentration was lowered, the spiral wave became meandering with outward petals. At 0.44 M H_2SO_4, the petals lied along a straight line. Further decrease in the H_2SO_4 concentration (0.40 – 0.27 M) caused the spiral tip to rotate with inward petals and, finally, the trajectory became a circle at 0.26 M H_2SO_4. The meandering trajectories in Fig. 3.2(a) can be approximated as hypercycloids [for outward petals, Fig. 3.2(b)] or epicycloids [for inward petals, Fig. 3.2(c)] which are a superposition of two independent circular motions [44, 46]. The spiral tip is a point fixed on a primary rotating circle

(with radius r_1, frequency f_1) whose center is on a secondary spinning circle (with radius r_2, frequency f_2). If the two circles rotate in opposite directions, the tip meanders with outward petals [Fig. 3.2(b)], otherwise, inward petals are obtained [Fig. 3.2(c)]. More complicated motions of the spiral tip called hypermeandering [53, 47] were also observed and they are not yet well characterized.

The effect of ageing on the temporal evolution of the spiral tip in the BZ reaction has been investigated using a closed system. In ageing process, the moderate consumption of the reagents in a closed BZ system causes a continuous change of the composition of the solution with time. As shown in Fig. 3.3(a) [45], the initial form of the tip trajectory can be either simply a circle or meandering patterns depending on the concentration of H_2SO_4, [H_2SO_4. Subsequently, different forms of the spiral tip motion developed. An initial circular spiral tip trajectory may become meandering with time ([$H_2SO_4 = 0.4$ M). The meandering patterns varied from outward petals to inward petals ([$H_2SO_4 = 0.21$ M and 0.16 M). In the end of experiments or at low H_2SO_4 concentration ([$H_2SO_4 = 0.11$ M), the tip moved along an open curve showing a shrinkage of wave fronts.

Changing of meandering patterns to approximately a circle has been also observed [48] as shown in Fig. 3.3(b). During the experiment, the initial meandering with four outward petals changed to three outward petals and eventually to circles with a small drift. As indicated by the interval time for each plotted pattern, the spiral wave in this experiment propagated very slowly giving a possibility to study 3D structures of scroll waves in thick media using tomography. Such an extremely low wave velocity is crucial for a tomographic study of scroll waves in a 3D BZ reaction [54, 9, 8, 55] since the wave velocity should be sufficiently low to be considered quasi-stationary as compared to the time required to rotate the reaction cuvette by 180° while taking a series of images. Only in such cases, reasonable tomographic reconstructions of the wave structures are possible.
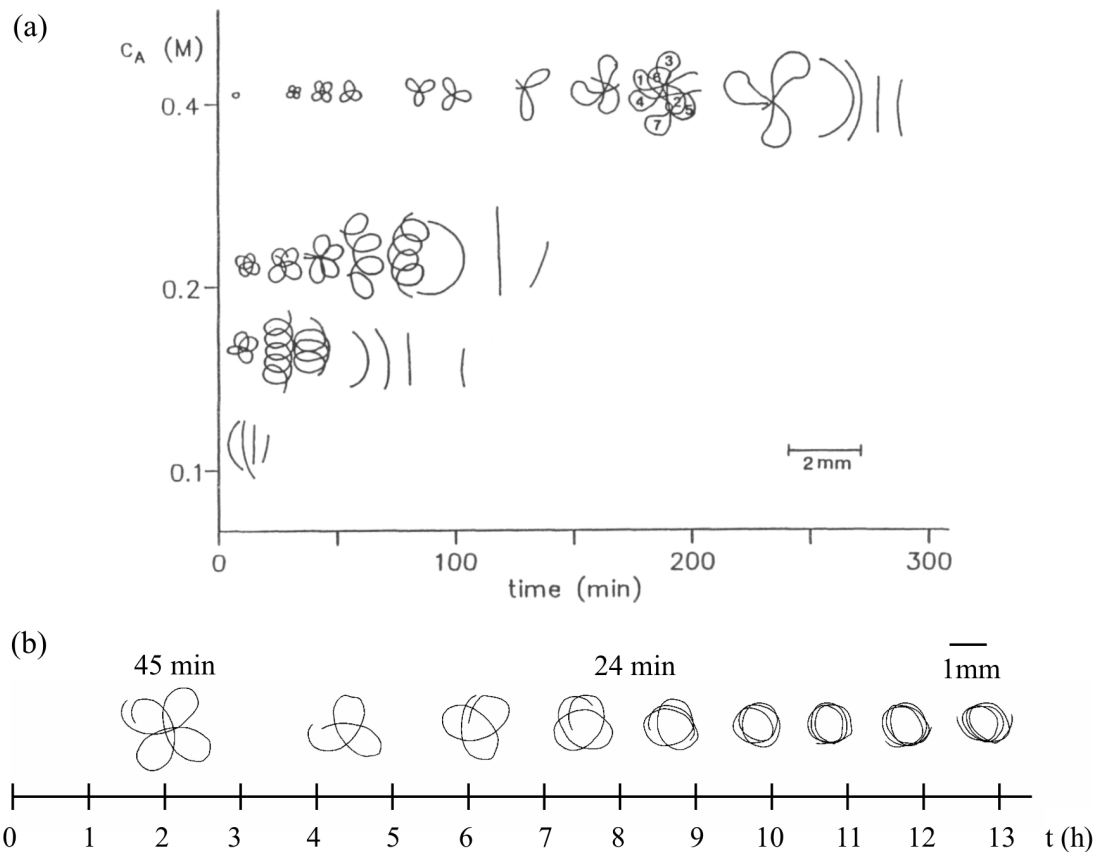
Figure 3.3: Ageing effect on the dynamics of spiral waves in the BZ reaction. (a) Trajectory of the spiral tip, for four different initial concentration of H_2SO_4 (C_A), as a function of time [45]. The initial form of the tip trajectory depends on the concentration: a circle at 0.4 M or meandering patterns at 0.21 M and 0.16 M H_2SO_4. Due to ageing, the pattern of the tip motion changed with time and finally the spiral tip propagated on an open curve indicating a shrinkage of the wave fronts. (b) The pattern of the spiral tip trajectory changed subsequently from four outward petals to three outward petals and eventually to a slightly drifting circle [48]. The interval that the spiral tip needs to complete most of the shown trajectories is 24 min except for the first trajectory which takes 45 min.

Spiral waves in the Barkley model

Meandering spiral waves have been found to be common in different model systems e.g., the Oregonator [56, 57, 58], FitzHugh-Nagumo [53], and the Barkley models [59, 60, 61, 62]. As an example, we will consider the dynamics of spiral waves in the Barkley model since this model has been also used in a study of scroll wave instabilities as presented in the next chapter. The reaction-diffusion system of the Barkley model reads:

$$
\begin{aligned}
\frac{\partial u}{\partial t} &= -\frac{1}{\epsilon}u(u-1)(u-\frac{v+b}{a}) + \nabla^2 u, \\
\frac{\partial v}{\partial t} &= u - v + D_v\nabla^2 v,
\end{aligned}
\tag{3.1}
$$

where u and v are the activator and the inhibitor, respectively. a, b, and ϵ are parameters, with $\epsilon << 1$. The length scale is chosen such that the diffusion coefficient for u is unity so D_v is the ratio of diffusion coefficients.

The bifurcation diagram for spiral waves in the Barkley model at $\epsilon = 0.02$ and $D_v = 0$ are shown in Fig. 3.4. The diagram has been derived from a bifurcation analysis: First, Eq. (3.1) is rewritten in a rotating frame with angular velocity ω_1. Then a steady solution (at a point (a, b) in the diagram) in the rotating frame, corresponding to a rigidly rotating spiral with angular velocity ω_1 in the rest frame, is determined by solving the non-linear eigenvalue problem which yield fields of u and v and also the eigenvalue ω_1. Finally, the stability of the steady solution is analysed. If the tested solution is stable, the considered point (a, b) exhibits rigidly rotating spirals. If it is unstable, then this point supports meandering spirals. In fact, a second angular velocity ω_2 emerges and leads to meandering spirals with two frequencies. The relation between two angular velocities determines the type of meandering: $\omega_2 > \omega_1$: outward petals; $\omega_2 < \omega_1$: inward petals; and $\omega_2 = \omega_1$: straight-line petals. The boundary between the periodic regime (rigidly rotating spirals) and the meandering regime is a bifurcation locus where the system bifurcates via a supercritical Hopf bifurcation.
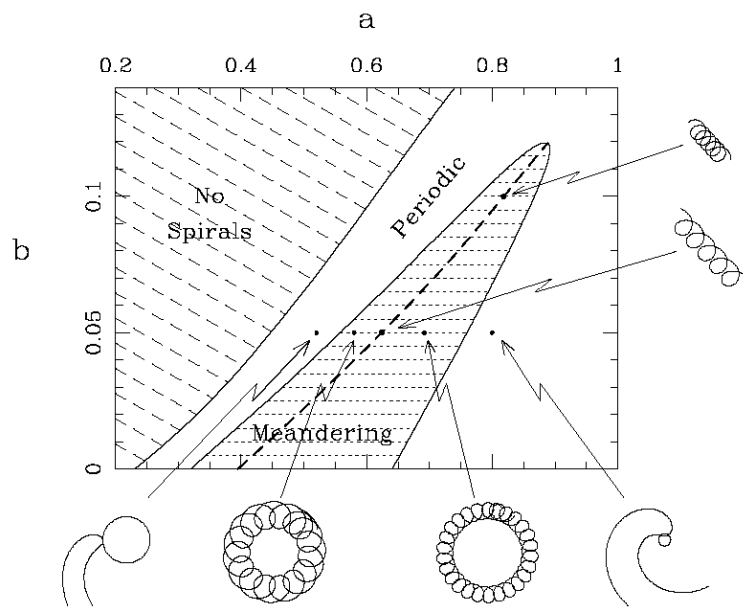
Figure 3.4: Phase diagram of spiral dynamics in the Barkley model with parameters $\epsilon = 0.02$ and $D_v = 0$ [62]. There are three main parameter regimes: No spirals, periodic rotating spirals, and meandering spirals. Examples of spiral tip trajectory at 6 points in different regimes are given. For rigidly rotating spirals, the diameter of the circular core varies with the parameters. The meandering regime is divided into outward petals (right part) and inward petals (left part) regions. On the separation line (dashed line), the petals lie along a straight line.

3.3   Control of spiral waves

In this section, we consider the two kinds of external perturbations, by light and by electrical current, which have been extensively used to the control of spiral waves in the BZ reaction.

3.3.1   Manipulation by electrical current

Excitation waves propagating in the BZ reaction result from the autocatalytic process of the activator $HBrO_2$, which is controlled by the concentation of Br^- and the catalsyt, coupling with the diffusion. The main species which control the onset of the autocatalytic reaction are the inhibitor Br^- and the metalic catalyst, e.g., ferroin. Both of them are ionic, thus, electrical forcing can alter their motion and consequently affect the dynamics of the excitation waves.

In the presence of electrical current, wave fronts which were moving towards the anode (+) were accellerated while those propagating to the cathode (−) were slowed down [63, 64, 65]. When the applied field was sufficiently high, propagating fronts towards the cathode were completely suppressed [63]. This result can be used to produce spiral waves from a circular wave [66]. The front facing the cathode is stopped and disappears, thus, the former circular wave becomes a curve with two free ends which later curl in and form two counter-rotating spiral waves. Reversal and spliting [67, 68] of wave fronts due to the applied current have also been observed.

The influence of elecrical current on the dynamics of spiral waves in a thin BZ medium in a gel have been studied by applying either a radial electric field or a field in one direction (e.g., in the x direction), as shown in Fig. 3.5. For the case of a constant radial field [69] [Fig. 3.5(a)], the period, the core size, and the wavelength of a spiral wave increased when the anode (+) was placed in the spiral core. However, the field which points towards the spiral core did not affect the spiral wave, i.e., the wave period does not decrease, since spiral structures are known as the highest-frequency wave source existing in excitable media. A rigidly rotating spiral became meandering and resulted in a super-spiral structure in an

(a)

(b)

water cooling

thermocouple
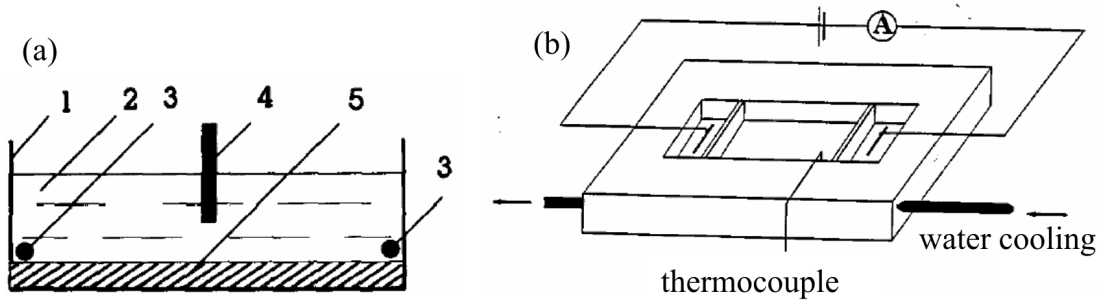
Figure 3.5: Schematic representation of the reactors used in experiments with electric field effect. (a) For an application of a radial electrical field [69], a silica gel layer with immobilized ferroin was placed into a Petri dish (1) while the other ingradients (2) of BZ reaction were on the top. A circular (3) and a needle shaped (4) electrode were immersed in the solution. (b) For the case of an electrical current in one direction [70], the BZ reaction in a gel was placed in the middle part of the reactor whose longitudinal ends were connected to electrolytic compartments filled with the aqueous BZ reaction or K_2SO_4 solution. The electrolytic compartments were separated from the main part by porous glass filters. An electrical current was applied via two electrodes. The temperatue was kept constant by water cooling.

alternating radial field [72].

The drift of spiral waves under a constant electrical current applied in one direction has been investigated [73, 71, 74, 70] using the reactor in Fig. 3.5(b) (or with some modification for feeding fresh reactants [73]). Similar to the electrical effect in the 1D case, the spiral tip was accellerated when it moved towads the anode and vise versa. However, the electrical current does effect the tip velocity. It affects not only the component parallel to the current but also the perpendicular component. As shown in Fig. 3.6(a), spiral waves, which were rigidly rotating in the absence of forcing, drifted linearly to the anode (+) with a velocity that can be separated into two components: one parallel v_x , the other perpendicular v_y to the electrical current. The perpendicular direction also depended on the chirality of the spirals. The clockwise rotating spiral [left in Fig. 3.6(c)] drifed to the bottom left while the counter-clockwise rotating spiral [right in Fig. 3.6(c)] drifted to the bottom right. The velocity and angle of drift (measured from v_x) increased with the applied current [Fig. 3.6(b)] [73, 71, 74]. In the absense of external forcing, the spiral waves in these experiments rotated rigidly and their shape was approximatly that of Archimedian spirals. While the spiral drifted, its shape deformed, as shown
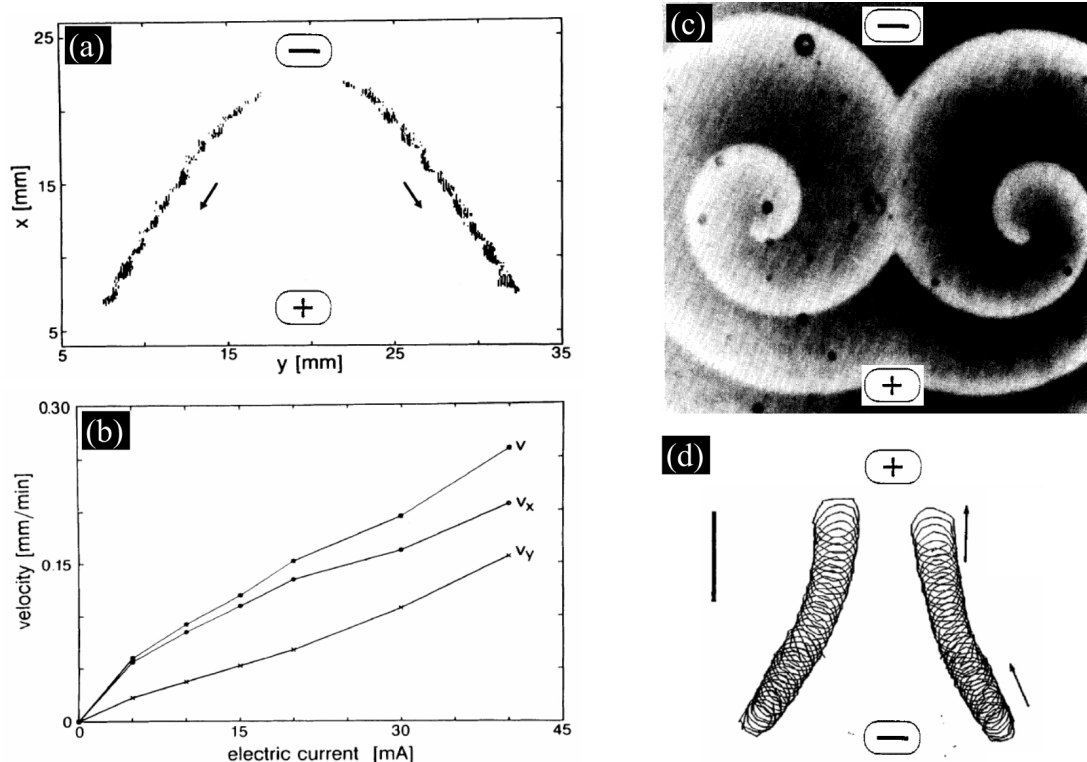
Figure 3.6: Drift of spiral waves in an electric field. (a) Locations of the cores of two counter-rotating spirals, in (c), drifting to the anode (towards the bottom) with two component velocity, parallel v_x and perpendicular v_y to the field. The direction of v_y depended on the chirality of spirals. (b) The two components of the drift velocity increased with the applied electrical current. (c) The deformation of spirals during the drift to the anode (+) [71]. (d) Two counter-rotating spiral tips drifted anti-parallel to the electrical current when they approached each other [70].

in Fig. 3.6(c).

When the direction of the field was inverted, the counter-rotating spirals in Fig. 3.6(c) drifted transversally towards the top so they approximated each other. As the distance between the spiral cores decreased, the perpendicular velocity v_y deminished until it eventually vanished, so that both of the cores drifted anti-parallel to the electrical current [70] as shown in Fig. 3.6(d). This results suggests the existence of a spiral repulsion causing the perpendicular velocity v_y to vanish. For a sufficiently strong electrical current, the two spiral waves were forced to self-annihilate and the final position of the spiral cores acted as a pacemaker emiting circular waves periodically [75].

Electrical field induced drifting of spiral waves in experiments has been reproduced in numerical simulations using the reaction-diffusion equation 2.1, e.g., the Barkley model [71, 76, 77, 78] and the Oregonator model [76, 79, 74, 70], with an additional advection term accounting for the effect of the electric field. In the three-variable (u, v, w) Oregonator model [Eq. (2.8)], there are two variables accounting for ionic species, v (ferroin) and w (Br^-), while u ($HBrO_2$) is neutral. The dynamics of u and w are approximately anticorrelated [Eq. (2.9)] and thus the electric field affects also the dynamics of the neutral species u. It has been shown that both reduced two- (u, v) and three-component versions of the Oregonator including the advection terms can reproduce the experimenally observed effect of an electrical field on the dynamics of 2D spiral waves [76, 79, 74, 70]. The two-variable Oregonator model with advection terms for both u and v accounting for the electric field E (field strength $E = |\mathbf{E}|$) in the x direction reads

$$
\begin{aligned}
\frac{\partial u}{\partial t} &= \frac{1}{\epsilon}\left(u - u^2 - fv\frac{u - q}{u + q}\right) + D_u \nabla^2 u - M_u E \frac{\partial u}{\partial x}, \\
\frac{\partial v}{\partial t} &= u - v + D_v \nabla^2 v - M_v E \frac{\partial v}{\partial x}
\end{aligned}
\tag{3.2}
$$

A parameter set which reproduces rigidly rotating spirals in the absence of electric field has the following values [56, 70]: $q = 0.002$, $f = 1.4$, $\epsilon = 0.01$, the diffusion coefficients $D_u = 1$ and $D_v = 0.6$. The ionic mobilities $M_u = -1.0$ and $M_v = 2.0$ [70] correspond to the charge of Br^- and ferroin, respectively.

3.3.2 Manipulation by light

The light sensitive ruthenium-catalyzed BZ reaction is problably the most exten-
sively used tool for studying external forcing of the dynamics of spiral waves in
excitable media. Light with a specific wave length of around 460 nm can reduce or
even completely suppress the excitability of the medium. Under illumination, the
photochemical process at the ruthenium catalyst promotes the production of the
inhibitor Br^-, thus the excitablity of the system decreases [37, 38]. As mentioned
in the last section, the dynamics of spiral waves depend on the system parame-
ters that are connected to the excitability. Therefore, light can be used to control
spirals in the ruthenium-BZ reaction.

Different kinds of light-induced perturbations on spiral waves have been in-
vestigated (as reviewed in references [80, 18]). The motion of a spiral tip can be
affected by the application of a single light pulse [81, 50], by periodic perturbations
[81, 50], or by a more elaborated control using a feedback mechanism [49].

Experiments with feedback control have been done by selecting an area in the
medium called sensory domain and the wave activity in the domain later deter-
mined the intensity of the light perturbation (feedback) to the medium. Under a
feedback control, the BZ reaction was illuminated with a time dependent intensity
$I(t)$ [82]

$$I(t) = I_0 + k_{fb} \left[B(t - \tau) - B_0 \right], \tag{3.3}$$

where I_0 is the background intensity corresponding to a spiral located in the center
of the sensory domain with an average gray level B_0. k_{fb} is an adjustable gain of
the feedback and τ is a delay time between the gray level measurement and the
illumination. The trajectory of a spiral tip under a feedback perturbation was
found to depend on the shape and size of the sensory domain, the strength of the
feedback gain k_{fb}, the delay time τ and the initial position of the spiral tip in the
medium [82, 80, 83], e.g. as shown in Fig. 3.7.
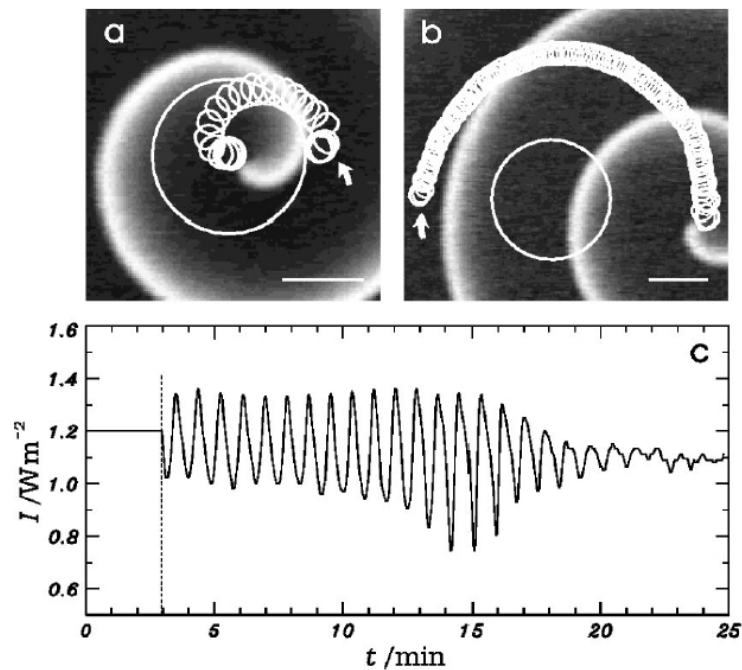
Figure 3.7: Light control of a spiral wave in the ruthenium-BZ reaction. Under a feedback control Eq. (3.3) with a circular sensory domain (circles in (a) and (b)), the spiral tip trajectory depends on the initial position of the spiral wave(arrows). In (a) the tip moved into the circle and was stabilized there while in (b) the spiral tip moved around the circle. Parameters: the feedback gain $k_{fb} = -0.5$ and no delay time $\tau = 0$. (c) The feedback illumination as a function of time for experiment in (a) [82].

Chapter 4

Scroll waves and external control

4.1 Scroll wave dynamics

As we have seen in the previous chapter, thin layers of excitable media often exhibit target patterns or rotating spital waves. In 3D media, the corresponding structures are expanding spherical waves and rotating scroll waves, respectively. A scroll wave can be considered as a stack of many spiral waves [see Fig. 1.2(a) and (b)]. The scroll wave rotates around a line of its filament which is the organizing center of the wave structure. The two simplest cases are a straight scroll wave [Fig. 1.2(a)], whose filament is linear, and a scroll ring [Fig. 4.1(a)] with a circular filament. Winfree and Strogatz [84, 85, 86, 87, 88] have investigated the anatomy on various exotic forms of rotating scroll waves when twists, links, and knots are imposed to the structures. They also provided suggestions for experimental implementation to realize such presented structures.

The dynamics of scroll waves are determined not only by the system parameters as in the case of spiral waves but also by the topology of the scroll waves – i.e., the shape of the filament and the twist of wave. We now consider some examples from simulations. In media with a sufficiently high excitability, both rotating spirals in 2D and straight scroll waves (in 3D) are stable [61, 91], however, scroll rings drift and contract until they disappear [89, 92], [Fig. 4.1(b)]. For low excitability, spiral waves may rotate stably (with a larger core) while straight scroll waves are
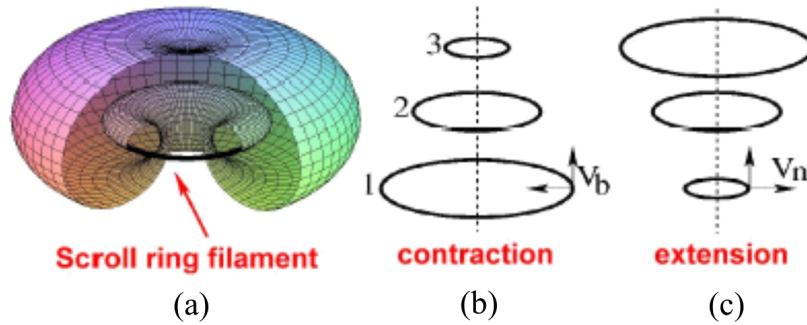
Figure 4.1: Contraction and expansion of scroll rings. (a) Schematic representation of a scroll ring and its filament. Scroll rings (b) contract at high excitability, however, (c) exapand at low excitability. In both cases the scroll rings drift along the axis of symmetry [89, 90].

unstable to a small perturbation [61, 91] and scroll rings drift and expand [89, 92], [Fig. 4.1(c)]. A twist of the wave in the additional third dimension can cause a formerly stable straight scroll wave (at high excitability) to deform [93, 91, 94] like a DNA ribbon. These phenonema will be revisited, in detail, in the following sections.

Figure 4.2 shows some examples of the dynamics of scroll waves in the BZ reaction. When observed from the top of the medium, a typical elongated spiral, which is a scroll wave with an inclined filament, becomes symmetric [51] [Fig. 4.2(a)]. An elongated ring, whose filament bends and terminates at the same wall, changes to a circular form and eventually disappears [51] [Fig. 4.2(b)]. A scroll ring may either contract and self-annihilate [95] [Fig. 4.2(c)] or expand [98]. An eight-shaped ring splits into two rings which subsequently shrink and disappear [95] [Fig. 4.2(d)]. Under a temperature gradient, a straight simple scroll wave becomes twisted and eventually its linear filament deforms to a helix [96, 97] [Fig. 4.2(e)].

In the next section, we will consider a *scroll ribbon* as a model for the shape of the scroll wave filament and the twist of a wave. Then we consider the temporal evolution of the scroll wave which is influenced by local properties of the scroll wave.

(a)

(b)

(c)

(d)

(e)
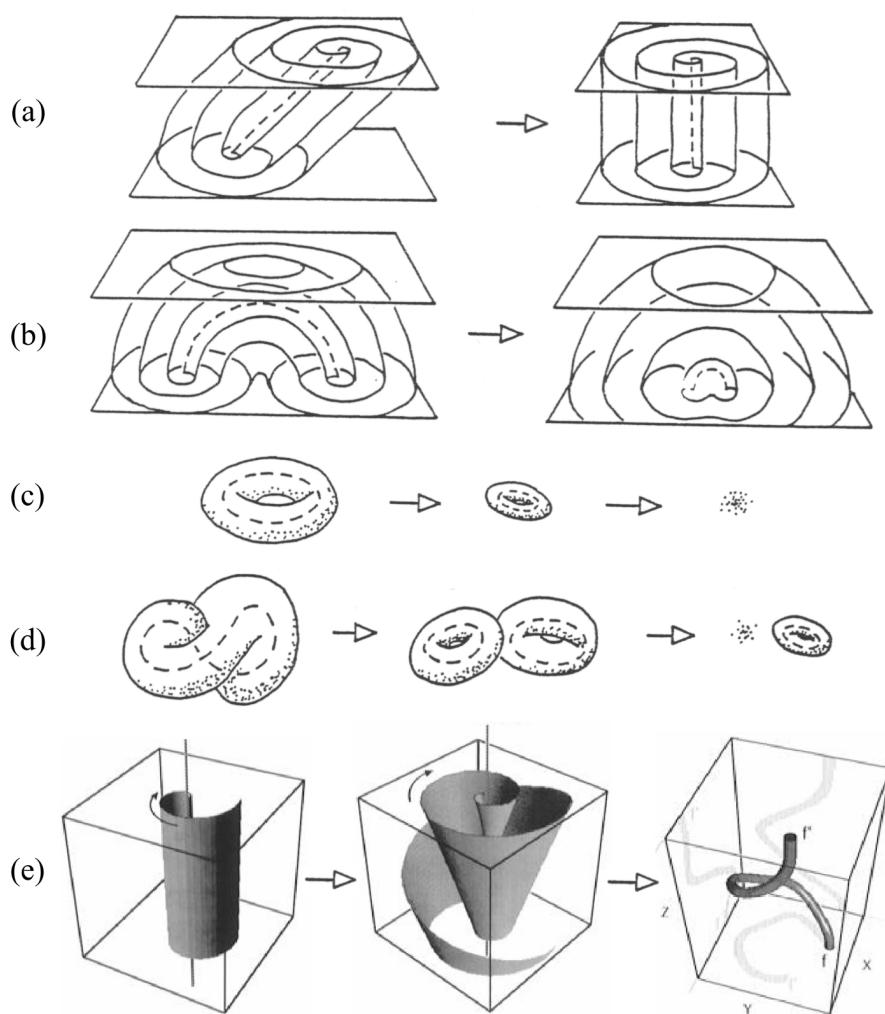
Figure 4.2: Examples of scroll wave dynamics in the BZ reaction observed in the laboratory. In (a) – (d) the dashed line represents the filament. (a) An elongated spiral becomes symmetric [51] and (b) an elongated ring becomes circular and then disappears [51]. (c) A scroll ring shrinks and disappears [95] and (d) an eight-shaped ring separates into two circular rings which contract and self-annihilate [95]. (e) In the presence of a temperature gradient, a simple scroll wave becomes twised and then the filament deforms to a helix [96, 97].

4.2 Theory of local filament dynamics

Since the filament of a scroll wave (in 3D Cartesian coordinates) is viewed as a one dimensional curved line [10, 11, 12], it is convenient to consider its geometry and dynamics using the *Frenet frame* which provides a natural orthogonal coordinate system. Suppose that the space curve of the filament is given by a position vector $\mathbf{R}(s) = (x(s), y(s), z(s))$ where s is the position along the filament with a length L so $0 \leq s \leq L$. To each point s, we attach orthogonal coordinates, called the *Frenet trihedron*, defined by the unit vectors $\mathbf{T}(s)$, $\mathbf{N}(s)$, and $\mathbf{B}(s)$, where

$$\mathbf{T}(s) = \frac{d\mathbf{R}}{ds}, \quad \mathbf{N}(s) = \frac{d\mathbf{T}/ds}{|d\mathbf{T}/ds|}, \quad \mathbf{B}(s) = \mathbf{T}(s) \times \mathbf{N}(s). \tag{4.1}$$

As we travel along the curve $\mathbf{R}(s)$, the Frenet trihedron rotates according to the *Frenet-Serret equations*

$$\frac{d\mathbf{T}}{ds} = \kappa \mathbf{N}, \quad \frac{d\mathbf{N}}{ds} = \kappa \mathbf{T} + \tau \mathbf{B}, \quad \frac{d\mathbf{B}}{ds} = \tau \mathbf{N}, \tag{4.2}$$

where $\kappa(s)$ and $\tau(s)$ are the curvature and torsion at the position s, respectively. In fact, the cuvature $\kappa(s)$ is the rotation rate of the Frenet trihedron around the $\mathbf{B}$ axis while the torsion $\tau(s)$ is the rotation rate around the $\mathbf{T}$ axis. At this point, we can characterize the shape of the filament using the Frenet trihedron together with the curvature and torsion.

To complete the description of the structure of a scroll wave, we need to specify the local phase of the wave around the filament. As shown in Fig. 4.3(a), the phase of a spiral wave in each cross-section perpendicular to the filament, can be defined as the angle ϕ between a unit vector $\mathbf{V}$ which is tangential to the spiral tip, and some fixed reference direction, e.g., the vector $\mathbf{N}$. As we move along the filament, this phase angle may change with a *relative twist rate* $= d\phi/ds$ with respect to the Frenet frame.

The idea of a scroll ribbon [Fig. 4.3(b)] was introduced to describe the structure of a filament including the twist of a wave. The local twist rate can be defined directly as the change in the orientation of the vector $\mathbf{V}$ yielding the *actual twist*
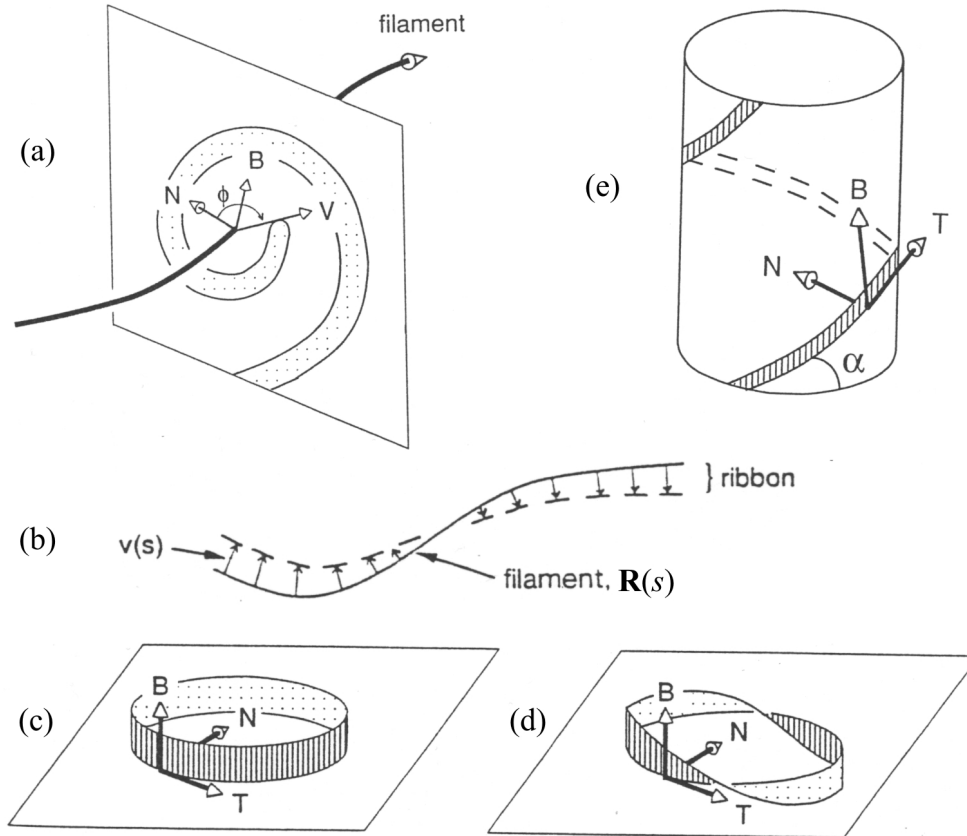
Figure 4.3: Scroll waves as represented by scroll ribbons [11]. (a) A cross-section of a scroll wave in the normal plane. $\mathbf{V}$ is a unit vector pointing from the filament to the spiral tip. ϕ is the phase angle of the spiral. $\mathbf{N}$ and $\mathbf{B}$ (and not shown $\mathbf{T}$) are unit vectors in the Frenet frame. (b) A scroll ribbon is composed of the filament $\mathbf{R}(s)$ and the unit vector $\mathbf{V}(s)$ to specify the wave twist. (c) An untwisted scroll ring has curvature, but neither torsion nor twist. (d) A twisted scroll ring has curvature but no torsion. The total twist of the twisted scroll ring must be an interger. (e) A helical scroll wave has both curvature and torsion but no phase gradient $(d\phi/ds = 0)$ so the twist rate is simply the torsion.

rate ω:

$$\omega = \tau(s) + \frac{d\phi}{ds}, \tag{4.3}$$

and the *total twist* T_ω (per turn) of the ribbon is

$$T_\omega = \frac{1}{2\pi} \int_0^L \omega(s)ds. \tag{4.4}$$

In other words, the twist rate of a scroll wave, as observed in a resting frame, is simply the sum of the torsion of the filament and the relative twist rate with respect to the Frenet frame.

Examples of scroll wave structures represented by the scroll ribbon are shown in Fig. 4.3(c)–(e). In Fig. 4.3(c), an untwisted ($\omega = 0$) scroll ring with a circular filament has a uniform curvature $\kappa = r^{-1}$, where r is the radius, and no torsion $\tau = 0$. As seen from Fig. 4.3(d), a twisted scroll ring with a closed loop filament lying in a flat plane also has no torsion, $\tau = 0$ so the twist rate $\omega = d\phi/ds$. Note that the total twist T_ω must be an interger due to the continuity of the rotation phase ϕ along the filament. The last example is a symmetrical helical scroll wave shown in Fig. 4.3(e). The ribbon wraps around a cylinder. Both curvature and and torsion exist in the helix. If the ribbon is in smooth contact with the ideal cylinder (the ribbon does not spin around itself), meaning that there is no local phase gradient $d\phi/ds = 0$, the twist rate is simply the torsion, $\omega = \tau$.

In 1988, Keener [10] has published a description of scroll wave dynamics, which is known as the *theory of local filament dynamics*, based on reaction-diffusion equations [Eq. (2.1)] and a sigular perturbation. The theory predicts the velocity of points along the filament and the phase of the wave (around the filament) from the local properties – the curvature κ and the twist rate ω [Eq. (4.3)], which includes the torsion τ and the local phase gradient $d\phi/ds$. It excludes nonlocal effects, e.g., interactions between segments of scroll waves which approch each other closely as well as the effect of the boundaries. Furthermore, it is assumed that a scroll wave is constructed as a stack of 2D rigidly rotating spiral waves and the filament has a small curvature and small twist rate. Therefore, the adjacent spirals are allowed to shift infinitesimally in 2D position and to have a small phase gradient. The

temporal evolution of such a scroll wave is described as

$$\frac{\partial \phi}{\partial t} = c_1 \kappa + b_1 \frac{\partial \omega}{\partial s} - a_1 \omega^2 + \frac{\partial \mathbf{R}}{\partial t} \cdot \mathbf{T} \omega - \frac{\partial \mathbf{N}}{\partial t} \cdot \mathbf{B}, \qquad (4.5)$$

$$\frac{\partial \mathbf{R}}{\partial t} \cdot \mathbf{N} = b_2 \kappa + c_2 \frac{\partial \omega}{\partial s} - a_2 \omega^2, \qquad (4.6)$$

$$\frac{\partial \mathbf{R}}{\partial t} \cdot \mathbf{B} = c_3 \kappa + c_4 \frac{\partial \omega}{\partial s} - a_3 \omega^2, \qquad (4.7)$$

where a_i, b_i, and c_i are constants. The details of their derivative are shown in [34, 11, 12]. As in Eq. (4.5), the local frequency $\partial \phi / \partial t$ of the scroll wave is higher or lower than the rotation frequency (ϕ) of a 2D spiral wave (in the same medium). The first three terms depict the local influence of the curvature κ, the twist rate ω, and the twist rate gradient $\partial \omega / \partial s$ while the last two terms take into account changes in the Frenet coordinate system. Eqs. (4.6) and (4.7) show that the filament drifts with a 2-component velocity – a normal $\partial \mathbf{R} / \partial t \cdot \mathbf{N}$ and a binomal $\partial \mathbf{R} / \partial t \cdot \mathbf{B}$ component. Note that the temporal dynamics of local phase ϕ and the filament position $\mathbf{R}$ are coupled since the twist rate ω is a function of ϕ as $\omega = \partial \phi / \partial t + \tau$.

Biktashev and colleagues [99] have refined Keener's theory by considering the symmetry of the problems and found that some constants vanish: $a_2 = a_3 = c_1 = c_2 = c_4 = 0$ which leads to a simpler form of the equations:

$$\frac{\partial \phi}{\partial t} = b_1 \frac{\partial \omega}{\partial s} - a_1 \omega^2 + \frac{\partial \mathbf{R}}{\partial t} \cdot \mathbf{T} \omega - \frac{\partial \mathbf{N}}{\partial t} \cdot \mathbf{B}, \qquad (4.8)$$

$$\frac{\partial \mathbf{R}}{\partial t} \cdot \mathbf{N} = b_2 \kappa, \qquad (4.9)$$

$$\frac{\partial \mathbf{R}}{\partial t} \cdot \mathbf{B} = c_3 \kappa \qquad (4.10)$$

The important property of Eqs. (4.8)–(4.10) in comparison to Eqs. (4.5)–(4.7) is that now the motion of the filament position $\mathbf{R}$ is independent of the rotation phase ϕ and the change of the length of the filament depends only on its curvature κ and the coefficient b_2, according to

$$\frac{dL}{dt} = -b_2 \int_0^L \kappa^2(s) ds \qquad (4.11)$$

The coefficient b_2 denotes as the *filament tension* and it plays a very special role in the dynamics of scroll wave filaments. When b_2 is positive, the filament length L decreases with time – e.g., elongated spirals become symmetric and scroll rings shrink and subsequently disappear. For the case of a negative tension $b_2 < 0$, the filament length increases irrespective to the initial form of the filament. Many numerical simulations [89, 100, 92, 58, 90] show that high excitability corresponds to positive tension. For low excitability, the tension becomes negative and causes an instability of scroll waves as described in the next section.

Untwisted circular scroll rings

Untwisted circular scroll rings are a simple case where there is no torsion and no twist rate. The curvature of the filament is also uniform, indepedent from the position along the filament, thus, $\kappa = 1/r$. In this case, the normal and binormal velocities of the filament are

$$\frac{dr}{dt} = -\frac{b_2}{r} \qquad , \qquad \frac{dz}{dt} = \frac{c_3}{r}, \tag{4.12}$$

which imply that the scroll ring shrinks ($b_2 > 0$) or expands ($b_2 < 0$) and possibly drifts along its axis of symmetry. Both components of the velocity are inversely propotional to the radius, in good agreement with numerical simulations [89] as illustrated in Fig. 4.1 and experiments using the BZ reaction [101, 102, 103, 55]. In fact, the experiments showed that b_2 equals to the diffusion coefficient of the activator $HBrO_2$ which is 0.12 mm^2 min^{-1}.

4.3 Scroll wave instabilities

Numerical simulations have shown that instabilities of scroll waves can happen in serveral situations. In the context of cardiac physiology, the wave instabilities can occur from the anisotropic orientation of the *Purkinije fibers* in the heart structure leading to a variation of wave speed in different propagating directions [20, 21, 22, 15, 16, 23, 24]. Even in simple homogeneous media, deformation of
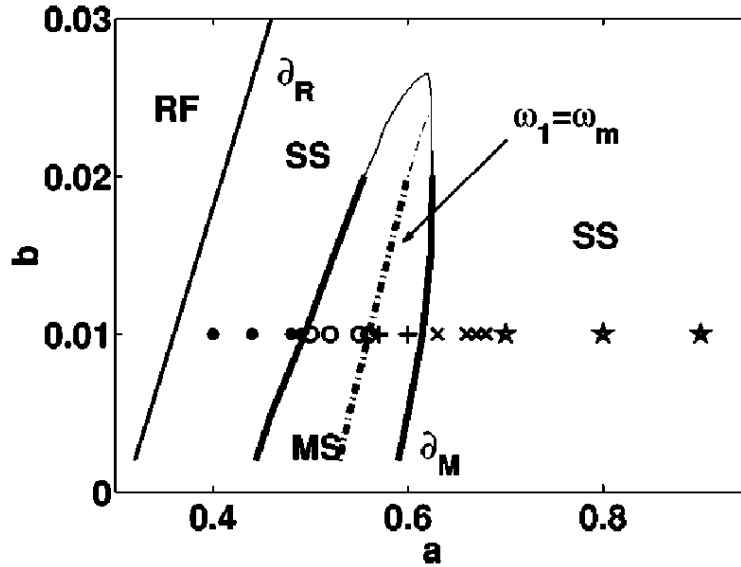
Figure 4.4: Scroll bifurcation diagram for the Barkley model Eq. (3.1) with $\epsilon =$ 0.025. SS: 2D steady rotating spirals, ∂_M: 2D meandering threshold instability, MS: meandering spirals with outward petals (+) and inward petals (○), ∂_R: the boundary of spiral wave existence, RF: the wave tip retracts. For scroll waves (3D); (⋆): stable scroll waves, (×) and (+): meandering-unstable scroll waves, (○) and (●): scroll waves with negative line tension.

scroll wave have been observed in many regime of system parameters.

Using the generic Barkley model Eq. (3.1), Henry and Hakim [104, 91], have analyzed systematically the different possible deformations of straight scroll waves in homogeneous excitable media. Based on linear stability analysis and fully 3D simulations, they characterized three different instabilities: 3D meandering, negative line tension and twist-induced instabilities.

Figure 4.4 shows the bifurcation diagram of the Barkley model, for both spiral waves in 2D and scroll waves in 3D, obtained from linear stability analysis. For 2D cases, the diagram Fig. 4.4 is qualitatively the same as the one shown in Fig. 3.4) (ϵ was changed from 0.02 to 0.025). The systems with the parameter values in the region labelled RF do not support spiral waves. In the MS area, spirals meander with outward or inward petal patterns. In the rest of the diagram, spiral waves rotate rigidly around a core with different sizes (labelled SS).

Now we consider different types of deformations of straight untwisted scroll waves while the parameters are varied – e.g., a variation of the parameter a from

high to low at $b = 0.01$. For 3D systems, straight scroll waves are stable at high values of a (labelled $\star$ in Fig. 4.4). The *3D meandering instability* ($\times$ and $+$) occurs when a decreases as found in a 2D system, however, the onset of meandering scroll waves happens at higher values of a as compared to the 2D case. In fact, a meandering scroll wave can be found outside of MS regime (on the right of MS, $\times$). As the values of a decreases further ($\circ$ and $\bullet$), the filament length of the scroll waves increases with time corresponding to the *negative line tension instability*. In contrast to rigidly rotating spirals, straight scroll waves become unstable in a wider area of the system parameters. While spiral waves are stable in the SS region, an instability of scroll waves occurs at low values of a ($\bullet$) in the same SS region.

Another scroll wave instability know as *twist-induced instability* or *sproing instability* [93] has been revealed when a sufficient twist was imposed to a straight scroll wave. This instability occurs even at high values of a ($\star$) where an untwisted straight scroll wave is stable.

In the following, some examples of the nonlinear evolution of these instabilities obtained from 3D numerical simulations are presented. Available experiments in the literature corresponding to the instabilities are also mentioned.

4.3.1   3D meandering instability

The third dimension induces the meandering instability at higher excitability (high a, ($\times$) in Fig. 4.4) comparing to the 2D case. Numerical simulations showed that a straight scroll wave (with a slightly perturbation by a sinusoidal function along its filament) deformed and, consequently, the filament length became larger than the system height. However, when the system was in a weakly 3D meandering regime (e.g., ($\times$) in Fig. 4.4), the filament restabilized to a zig-zag or a helical form depending on the boundary conditions as shown in Fig. 4.5. When periodic boundary conditions were imposed at the top and bottom, a preturbed straight filament deformed to a uniform helix [105, 91, 58] [Fig. 4.5(a)] , i.e., its top projection appeared as a circle [Fig. 4.5(c)]. For no–flux boundary conditions, the restabilized structure showed a flat zig-zag [91] and its top view showed a straigh

line [Fig. 4.5(d)]. Both forms of the filament also spined and moved around a vertical axis [Fig. 4.5(c) and (d)].

The thickness of the system also plays a role in the stability of scroll waves in the meandering regime. Rusakov *et al.* [106], using the Aliev-Panfilov model [107] for cardiac tissue, found that even in a strong meandering case the perturbation of a straight scroll wave decayed when the thickness of the simulation system was small. Figure 4.6 shows the temperal evolution of a strong meandering scroll wave and its filament length. In a thick system [12.7 mm, Fig. 4.6(a)–(c)], the filament deformed to a complicated structure and the spiral tips in horizontal sections were nonsynchronized – i.e., the trajectory of spiral tips varied along the z direction. The filament length oscillated quite strongly with high and low frequencies [black curve in Fig. 4.6(d)]. For an intermediate thickness (3.1 mm), the low frequencies of the filament length oscillation disappeared [gray curve in Fig. 4.6(d)]. When the thickness was lower than a critical value (2.5 mm), the relative filament length approached the height of the system [dashed line in Fig. 4.6(d)]. In this case, the filament was simply approximated a straight line, however, it still meandered in space.

Restabilization of meandering scroll waves was also observed in the Oregonator model [58] for the parameters corresponding to 2D outward petal meandering. In the case of inward petals, the negative line tension also occurs and causes the filament to expand so that no restabilized filament can exist in this meandering regime [58].
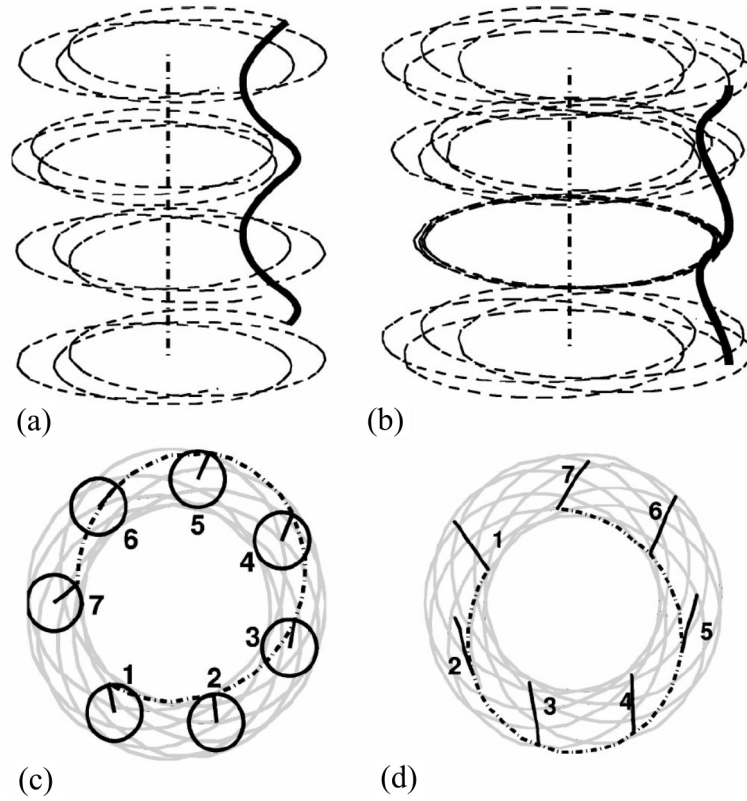
Figure 4.5: Restabilization of meandering scroll waves [91] in the Barkley model Eq. (3.1). Parameters: $a = 0.684$, $b = 0.01$, and $\epsilon = 0.025$. (a) and (b) represent the filaments (black lines) and the trajectories of spirals in horizontal cross-sections while (c) and (d) are the top projection of (a) and (b), respectively. For periodic boundary conditions [(a) and (c)], an initial straight scroll wave (with a slightly sinusoidal amplitude perturbation) deformed to a stable helical scroll wave. The helical filament (a) appeared as a circle in the top projection (c). When no-flux boundary conditions were used [(b) and (d)], the perturbed straight filament deformed to a stable a zig-zag shaped filament so its top view appeared as a straight line. Both forms of the filaments spined (around themselves) and rotated around a vertical axis [(c) and (d)].
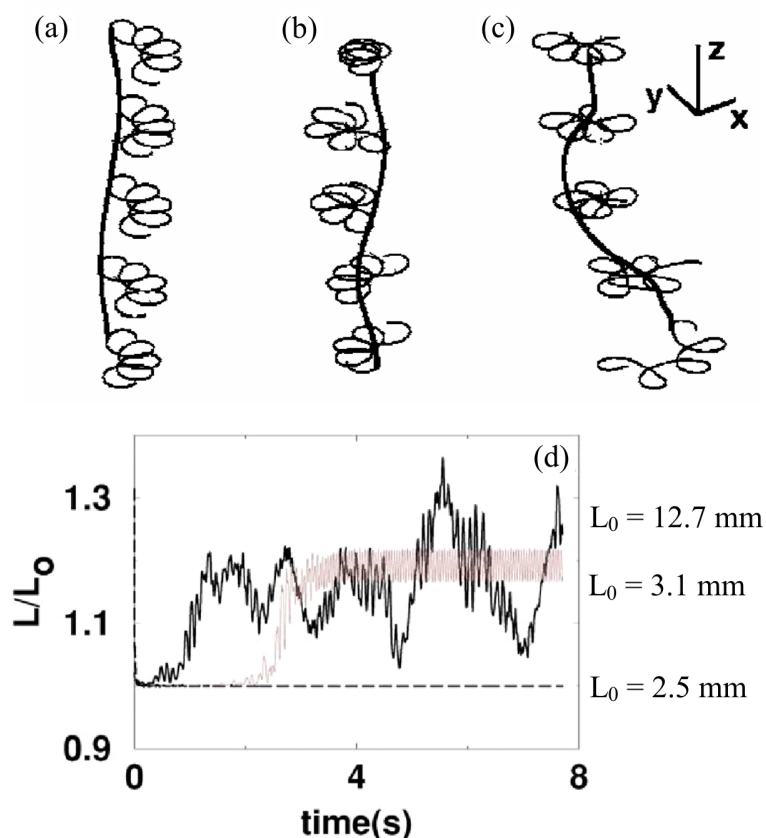
Figure 4.6: Influence of the medium thickness on meandering scroll waves [106]. (a–c) Temporal evolution of a strong meandering scroll wave in the Aliev-Panfilov model with a thickness of 12.7 mm. In such thick media, the initial, almost straight filament strongly meandered and deformed causing its length to oscillate aperiodically [black curve in (d)] with low and high frequencies. For an intermediate thickness of 3.1 mm [gray curve in (d)], the perturbed straight filament also deformed so its length was longer than the system height, however, the low frequency component of the filament length oscillation disappeared. When the system was very thin, (2.5 mm), the perturbation on the filament decayed so the filament became straight in vertical direction. Its length equaled to the thickness of the medium [dashed line in (d)] even if it still meandered.
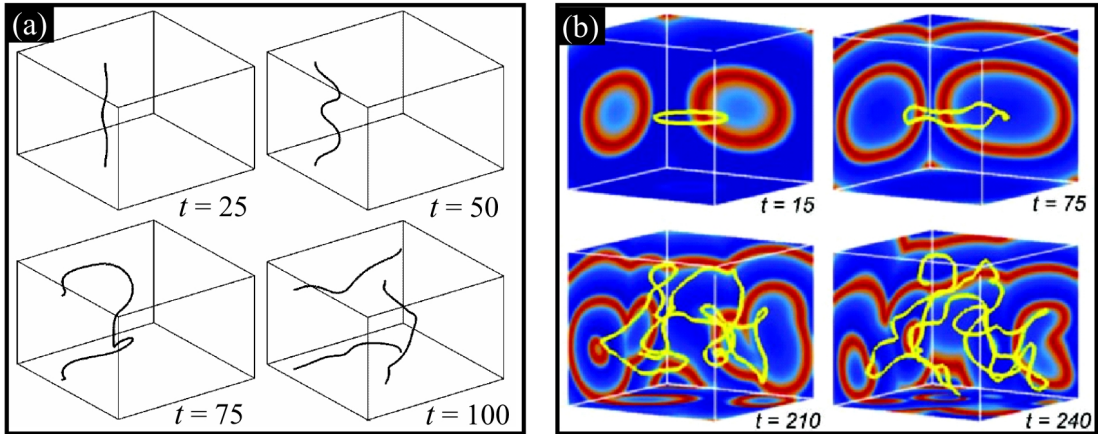
Figure 4.7: Dynamics of scroll waves in the negative line tension regime. The Barkley model Eq. (3.1) was used in simulations started with (a) a slightly perturbed straight scroll wave (parameters: $a = 0.44$, $b = 0.01$, and $\epsilon = 0.025$) [91] and (b) a uniform scroll ring (parameters: $a = 1.1$, $b = 0.19$, and $\epsilon = 0.02$) [100]. In both cases, the filament deformed and its length increased in the course of time. When the filament touched the walls, it broke into parts and grew further, thus, filling up the volume leading to the occurrence of *Winfree turbulence*.

4.3.2 Negative line tension instability

The negative line tension instability was found to happen in weakly excitable media where 2D systems exhibited large core stable spirals [99, 91, 100, 92, 58, 90] or meandering spirals with inward petals [58]. In the negative line tension regime, the filament of a scroll wave deforms and lengthens regardless of its initial form. As shown in Fig. 4.7, a perturbed straight filament [Fig. 4.7(a)] and a uniform scroll ring [Fig. 4.7(b)] deformed and lengthened. When their bent parts break at the boundary, the filaments split and continuously fill up the volume leading to 3D chaotic wave patterns known as *Winfree turbulence*. This kind of turbulence occurs exclusively in 3D excitable media and is currently considered as one of the principal mechanisms of cardiac fibrillation [13]. Alonso *et al.* have shown that the negative line tension instability and the subsequent Winfree turbulence are common features of many models of excitable media [100, 92, 58, 90]. They also demonstrated that Winfree turbulence can be suppressed by temporal periodic modulations of the excitability of the system.
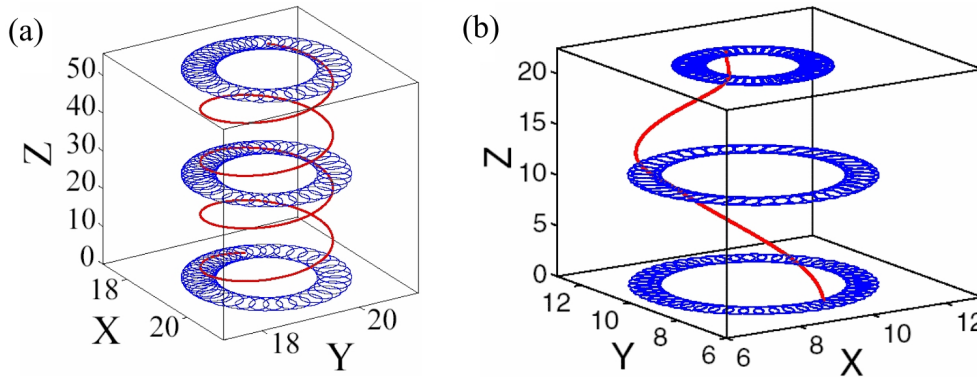
Figure 4.8: Deformation of scroll waves induced by a twisted wave [94]. A straight filament was found to deform to a helix when a sufficiently high twist rate was applied to the scroll wave. (a) For a homogeneous medium with periodic boundary conditions in the z direction, the helix was symmetric and its number of turns was an integer. (b) For no–flux boundary conditions, the deformation can be observed only in inhomogeneous media. The twist wave was obtained by setting the excitability of the upper part higher than that of the lower part. Such a jump of excitability caused a straight filament to become an asymmetric helix. The filament took a helical shape of constant radius in the less excitable (bottom) part and its radius decreased to zero in the higher excitability (top) portion.

4.3.3   Twist-induced instability

The presence of twist increases the rotation of a wave around the filament. Numerical simulations [93, 91] showed that when a small twist was imposed to a straight scroll wave, the filament remained linear. However, the spin frequency of the (smooth) twisted scroll wave increased with the square of the twist rate ($d\phi/dt \propto \omega^2$) [108, 93] in agreement with Keener's theory (section 4.2). When the twist rate became higher than a threshold, a linear filament *sproings* [93] to a stable helical shape. Note that for a linear filament no torsion is present and the twist rate is simply the local phase gradient ($\omega = d\phi/ds$). The critical twist rate, which causes the sproing instability to occur, depends on the simulation model. The instability can be observed at twist rates $\omega > 0.6$ for the Oregonator model [93] and $\omega > 0.35$ in the Barkley model [91].

For homogeneous media where twist was applied only at the beginning of an experiment or simulation, the sproing arose only in simulations using periodic boundary conditions (at the two ends of the filament) due to the continuity of the filament [as top and bottom of Fig. 4.8(a)] while in the case of no–flux boundary
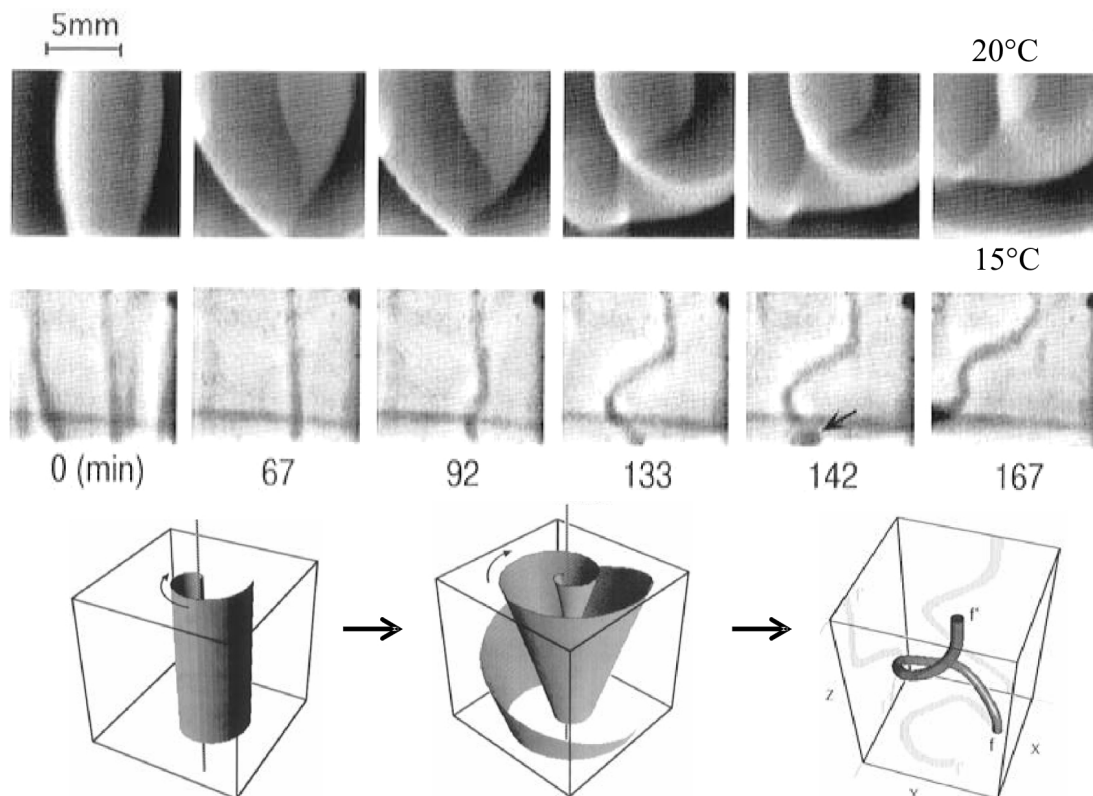
Figure 4.9: Twist-induced instability of a scroll wave in the BZ reaction under a temperature gradient [97]. Top row: Time series of a lateral projection of a scroll wave depict the wave front. Middle row: To estimate the shape of the filament (dark curves), the lateral projections, recorded during one wave rotation, were averaged. Bottom row: Schematic representation of the temporal evolution of the scroll wave and its filament. Under a temperature gradient of 5°C cm^{-1}, a straight untwisted scroll wave (0 min) became twisted (67 min). During the experiment, the twist rate increased continuously and the deformation of the filament from a straight line to a helix became evident (92 – 167 min).
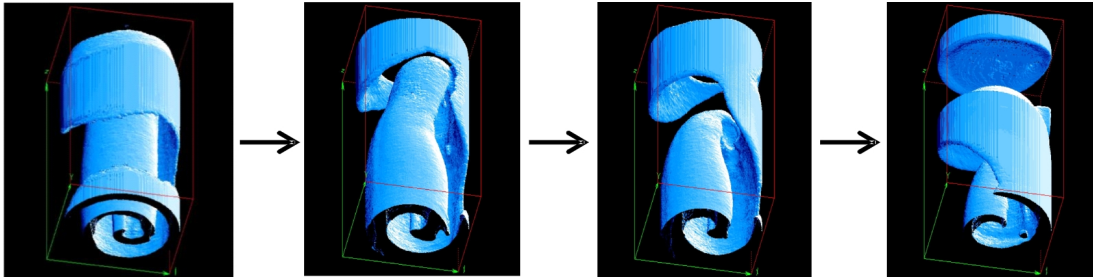
Figure 4.10: Twist-induced instability of a scroll wave in the BZ reaction under a gradient of oxygen concentration [8]. 3D isoconcentration surfaces of the scroll wave were obtained from tomographic reconstruction. During the experiment, the top surface of the medium was exposed to the atmosphere leading to a gradient of oxygen concentration in the vertical direction. Due to the inhibitory effect of oxygen, the wave at the upper part propagated slower than that at the bottom, thus, the twist of wave increased with time. The initial straight filament bent and broke when it touched the wall of the container.

conditions, an initial twisted scroll wave became untwisted [108]. By applying a spatial gradient of excitability along the initial straight filament in inhomogeneous media, a defomation to a helical filament [e.g., Fig. 4.8(b)] was also observed when no flux boundary conditions were imposed in the simulations [94].

Experiments on the twist-induced instability have been realized using the BZ reaction. Twists were imposed by gradients of temperature (Fig. 4.9) [96, 97] or gradients of oxygen concentration (Fig. 4.10) [8]. Both represent spatial gradients of excitability. In Fig. 4.9, a temperature gradient of $5°C$ cm^{-1} was applied to a straight scroll wave. The wave at higher temperature at top rotates faster than the wave at other end. This created a twisted wave around the filament and the scroll wave adopted a cone shape. The twist rate ω also increased with time. The observed twist rate for destabilization to a helical filament is about 0.7 rotation/wavelength.

In other experiments, the top of BZ media were opened to the atmosphere, so that, oxygen from the atmosphere diffused into the upper part of the media. The inhibitory effect of oxygen [109, 110, 30] caused the wave at the top part to propagate slower than that at the bottom. Again, this caused a twisted wave to occur and subsequently the straight filament deformed. A break up of the filament was observed when the bent part touched the wall of the reaction cuvette.
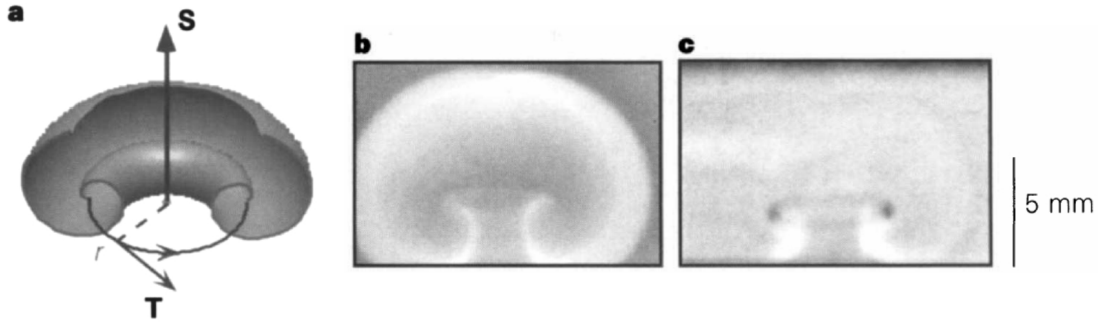
Figure 4.11: Scroll ring and the unit vector defining the orientation [103]. (a) Schematic cross-section of a scroll ring with a circular filament. **T** is the unit tangential vector along the filament. The unit vector **S** specifies the orientation of the scroll ring. **S** is normal to the filament plane and its direction is given by appling the right-hand rule to **T** along the ring. (b) A lateral projection of a scroll ring in the BZ reaction shows two counter-rotation spirals. (c) The spiral cores appear as dark regions in the averaged image of the lateral projections taken during one rotation of the scroll ring.

4.4 Control of scroll rings

We now consider two kinds of experiments on external forcing of scroll rings in the BZ reaction. The dynamics of scroll rings have been controlled by applying temperature or light gradients, both of which caused a inhomogeneous spatial excitability. The theory accounting for the experimental results is also presented.

4.4.1 Manipulation by temperature

Vinson *et al.* [103] have studied the influence of a temperature gradient on the orientation of scroll rings in the ferroin-catalyzed BZ reaction. Figure 4.11(a) shows a sketch of a scroll ring and its unit vector **S**. To describe the orientation of the scroll ring, a unit vector **S** has been defined [103, 111] as the normal vector of the filament plane with an orientation given by applying the right-hand rule to **T** along the ring shaped filament. The unit tangent vector **T** points in the direction of the local angular wave velocity.

Figure 4.11(b) depicts an experimental observation of the lateral projection of a scroll ring which appears as a pair of counter-rotating spirals. The spiral cores emerge as two dark spots in the averaged images, Fig. 4.11(c), of a series of the
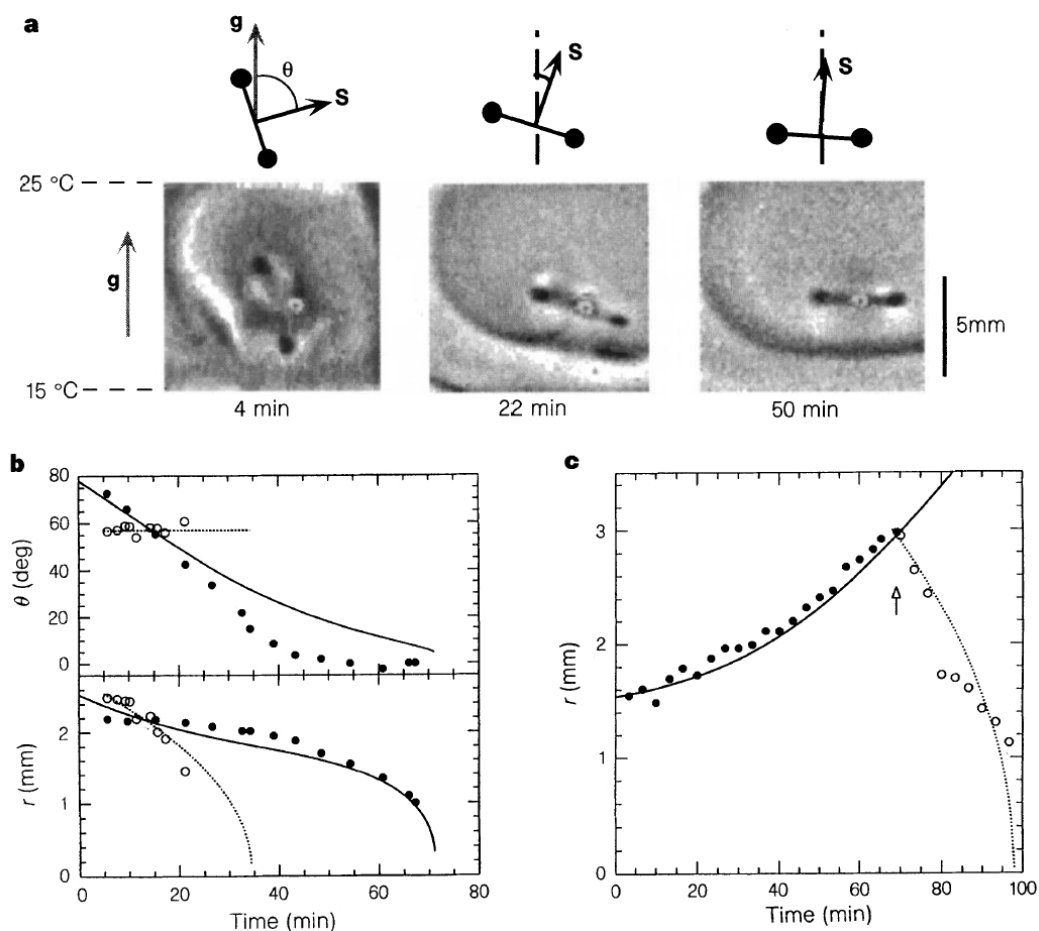
Figure 4.12: Reorientation of a scroll ring in the BZ reaction under a temperature gradient [103]. (a) Under a temperature gradient of $\mathbf{g}$ ($|\mathbf{g}| = 10°C$ cm^{-1}), the ring filament rotates so that the angle θ between the unit vector $\mathbf{S}$ and the gradient $\mathbf{g}$ decreased towards $0°$. (b) Changes in the angle θ and the ring radius r as a function of time. In the absence of any gradient ($\circ$), the scroll ring shrank and no reorientation took place. Due to the temperature gradient ($\bullet$), the scroll ring reoriented and its lifetime was also prolonged almost three times. (c) At $\theta = 0°$, there was no reorientation, however, an expansion of a scroll ring (r increased with time) could be observed under a stronger gradient ($|\mathbf{g}| = 20°C$ cm^{-1}). After the gradient was removed, the scroll ring contracted. The experimental results agreed well with numerical calculations [(lines in (b) and (c)] using the theory of local filament dynamics in parameter gradients presented in section 4.4.3.
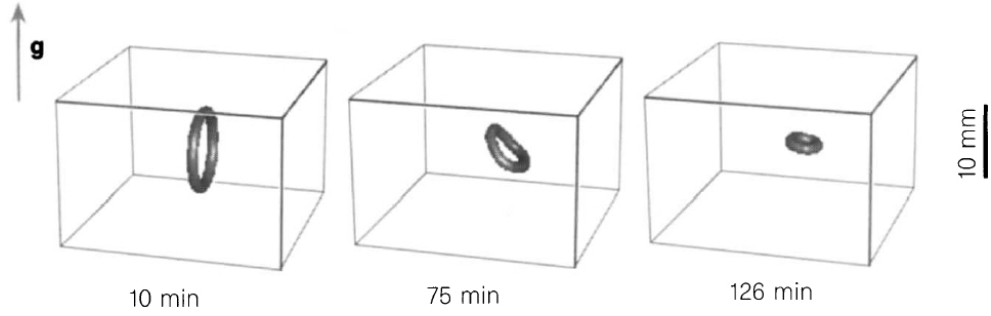
Figure 4.13: Numerical simulations of scroll ring reorientation in a temperature gradient [103]. The Bz model of Aliev and Rovinsky was used. Under a temperature gradient in a vertical direction, an initial circular filament lying in a vertical plane contracted and reoriented. The filament plane turned from vertical to horizontal, i.e., the unit vector **S** was parallel to the gradient **g**.

lateral projections recorded during a single spiral rotation. The filament alignment (in the lateral projection) can be estimated from the line connecting the two spiral cores so that the radius r of the scroll ring and the orientation angle θ [see Fig. 4.12(a)] can be calculated. In the absence of an external field, the BZ reaction used in these experiments supported self-contracting scroll rings, i.e., the radius r of the ring filament decreased with time and no reorientation occurred [∘ in Fig. 4.12(b)].

Under a temperature gradient **g** ($|\mathbf{g}| = 10°C \ cm^{-1}$), a scroll ring reoriented [Fig. 4.12(a)] so that the angle θ between the unit vector **S** and the gradient **g** decreased from $\approx 90°$ to $0°$ [● in Fig. 4.12(b)]. Once **S** and **g** were parallel, the reorientation process stopped. Experiments with initial angles θ_0 of $0°$ and $180°$ showed no reorientation.

The lifetime of the scroll ring was prolonged (from 20 min in the absence of any gradient to 70 min) in the experiments with initial angles $\theta_0 \approx 90°$ [Fig. 4.12(b)]. Expansion of a scroll ring [Fig. 4.12(c)] has been observed when a stronger gradient ($|\mathbf{g}| = 20°C \ cm^{-1}$) was applied in the experiment with initial stationary orientaion $\theta_0 = 0°$. As soon as the gradient was removed, the expansion stopped and the scroll ring rapidly contracted and subsequently self-annihilated. In contrast, when $\theta_0 = 180°$, the temperature gradient accelerated the scroll ring contraction. In experiments using $|\mathbf{g}| = 10°C \ cm^{-1}$ and $\theta_0 = 180°$, scroll rings with initial radius

as in Fig. 4.12(b) collapsed within less than 8 min. Numerical simulations (Fig. 4.13) using the Aliev-Rovinsky [112] model for inhomogeneous excitable media reproduced the dynamics of scroll rings presented in Fig. 4.12(b).

4.4.2   Manipulation by light

Control of scroll ring dynamics in the photosensitive ruthenium-catalyzed BZ reaction using light gradients has been investigated by Amemiya *et al.* [113] both in experiments and numerical simulations. As discussed in the previous chapter, the ruthenium-BZ reaction becomes less excitable when it is illuminated with light of 460 nm wavelength. Such an illumination with this light results in a spatial gradient ($\mathbf{g}$) of excitabity in the transverse direction to the illumination since stronger light intensity causes the medium to be less excitable and the light intensity attenuates through the medium thickness, according to the Beer-Lambert law. This knowledge has been utilized for a well-controlled initiation of scroll waves in such 3D BZ reaction media [114, 113].

Figure 4.14(I) shows an initiation of a scroll ring from a circular wave [(a) in Fig. 4.14(I)] using a light gradient in simulations while the illumination was applied from the bottom of the medium. A sufficiently strong illumination erased the lower part of the circular front [(b) in Fig. 4.14(I)]. When the light intensity was lowered until the whole medium became excitable again, a scroll ring formed [(c)–(h) in Fig. 4.14(I)]. The structure of a scroll the ring appears as target and two counter-rotating spirals in the top and lateral projections, respectively.

Figure 4.14(II) presents the filament velocity, which is the change of scroll ring radius dr/dt in the course of time in dependence of the illumination. For $\theta = 180°$, the ring always shrank. In the case of $\theta = 0°$, the scroll rings contracted at small illumination, however, expanded when the illumination was stronger than a critical value. Note that the rate of contraction and expansion increases with the intensity of the illumination.
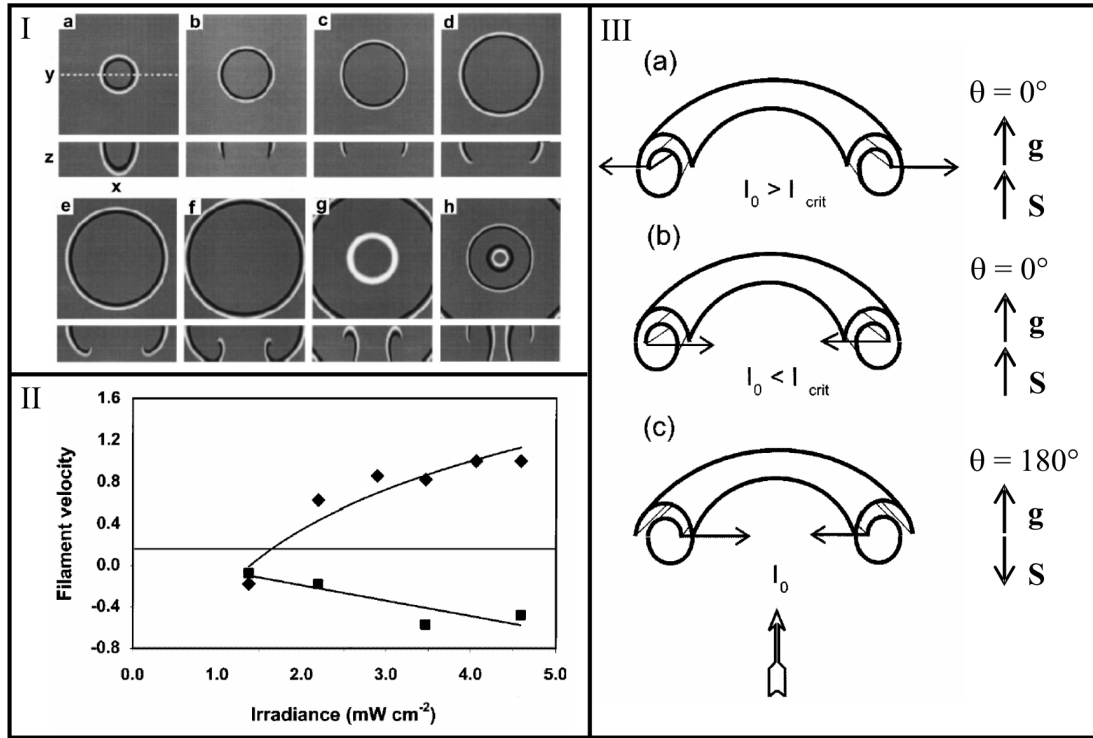
Figure 4.14: Control of scroll rings by a light gradient [113]. (I) Initiation of a scroll ring: xy and xz horizontal and vertical cross-sections, white and black curves depict the front and wake of waves. (Ia) A circular wave was created in a ruthenium-BZ medium. (Ib) The lower part of the circular wave was erased by light with sufficient intensity, (Ic–Ih) a scroll ring occurred after the illumination was lower. (Ih) The vertical sections show a pair of counter-rotating spirals while the horizontal sections show expanding and contracting circular waves. (II) Relative velocity of the scroll filament as a function of illumination intensity. 0.011 mm s^{-1} was scaled to unity. For $\theta = 180°$ (see IIIc for a sketch): squares, the scroll rings always shrank (the velocity < 0). For $\theta = 0°$: diamonds, the scroll rings contracted at low illumination I $<$ I$_{crit}$ (see IIIb). When I $>$ I$_{crit}$ (see IIIa), the scroll rings expanded when the illumination was higher that a critical value I$_{crit}$. The rate of contraction and expansion increased with the illumination intensity. (III) Schematic representation of the expansion (IIIa) and contraction (IIIb–IIIc) of a scroll ring. θ is the angle between the unit vector **S** of the scroll ring and the gradient **g** of the excitability (in the transverse direction to the illumination I$_0$).
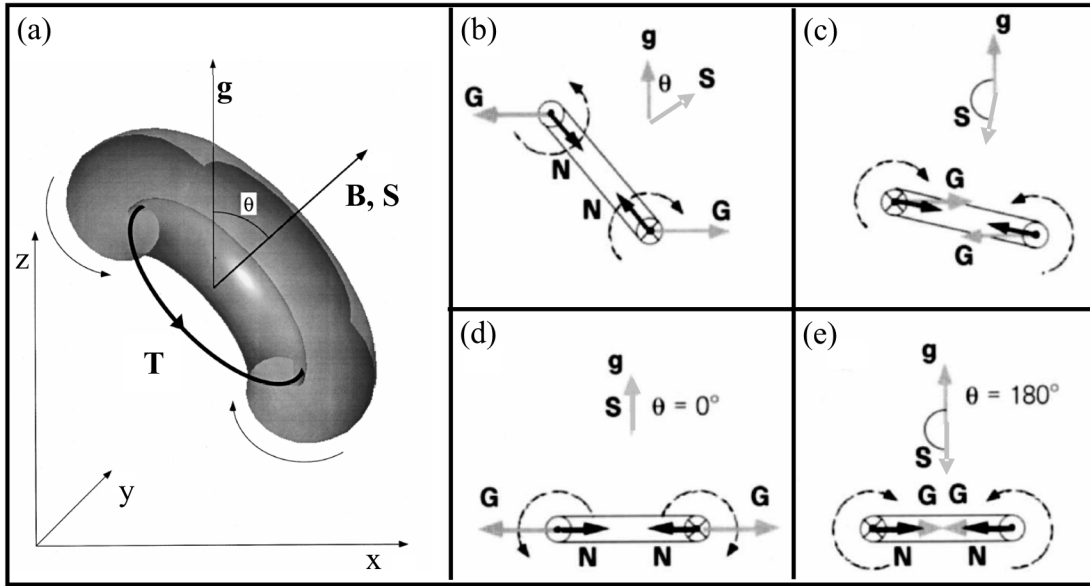
Figure 4.15: Schematic representation of scroll ring reorientation in parameter gradients [103, 111]. **T**, **N**, and **B** are the unit vectors of Frenet trihedal (**T**: tangential, **N**: normal, and **B**: binormal). (a) A scroll ring inclines in an applied gradient **g**. The angle θ between the unit vector **S** and the field **g** specifies the orientation of the scroll ring. The gradient **g** induces an additional velocity **G** which points in opposite direction at opposite points on the filament. (b)–(c) When $\theta \neq 0°, 180°$, the induced velocity **G** causes a net torque that turns the plane of the filament to reduce the angle θ. (d)–(e) There is no reorientation of scroll ring at $\theta = 0°, 180°$. For an intrinsic contracting scroll ring, the velocity **G** deaccellerates the contraction or even causes the scroll ring to expand (d) at $\theta = 0°$ while the contraction is accellerated (e) at $\theta = 180°$.

4.4.3 Theory of scroll ring dynamics under a parameter gradient

Vinson *et al.* [103, 111] have extended the theory of local filament dynamics [34, 99] (presented in section 4.2) for a scroll ring under the influence of a parameter gradient, e.g., a temperature gradient, light gradient, and electrical current. In such inhomogeneous media, it is assummed that weak and smooth inhomogeneities may be accounted for by adding the gradient-induced drift velocity $\mathbf{G}(p)$ to the local filament velocity $d\mathbf{R}(p)/dt$ [the combination of Eqs.(4.9) and (4.10)]:

$$\frac{d\mathbf{R}(p)}{dt} = \alpha\kappa(p)\mathbf{N}(p) + \mu\kappa(p)\mathbf{B}(p) + \mathbf{G}(p), \qquad (4.13)$$

where $\mathbf{N}(p)$ and $\mathbf{B}(p)$ are the local unit vector normal and binormal to the curved filament, with curvature $\kappa(p)$ at location p. α and μ [called, respectively, b_2 and c_3 in Eqs.(4.9) and (4.10)] are constants and depend on the parameters of the medium. For scroll rings, α is the filament tension that describes the contraction or the expansion of the scroll rings and μ describes the drift of scroll rings along the axis of symmetry (along the unit vector $\mathbf{S}$). Similar to the theory of local filament dynamics, Eq. (4.13) is valid for sufficiently small curvatures and twist rates.

Numerical simulations and experiments indicated that spiral waves drifted under an external field with a 2-component velocity, parallel and perpendicular to the field. Therefore, when a gradient is applied in the $\mathbf{Z}$ direction, the local gradient-induced velocity $\mathbf{G}(p)$ can be written as

$$
\begin{aligned}
\mathbf{G}(p) &= \beta g \mathbf{T}(p) \times \mathbf{Z} + \gamma g \mathbf{Z} \\
&\equiv \mathbf{G}(p)_{\perp} + \mathbf{G}(p)_{\parallel},
\end{aligned}
\tag{4.14}
$$

where $\mathbf{T}(p)$ is the local unit vector tangential to the filament at point p, g is the gradient strength, and two coefficients, β and γ describe the components of the drift velocity perpendicular and parallel to the gradient, respectively. In fact, β and γ can be determined from 2D observations.

For a planar and circular scroll ring with radius r, and inclined by an angle θ with respect to the gradient in z direction [4.15(a)], the temporal evolutions are given by

$$
\frac{dr}{dt} = -\frac{\alpha}{r} + \beta g \cos\theta,
\tag{4.15}
$$

$$
\frac{d\theta}{dt} = -\frac{\beta g}{r} \sin\theta,
\tag{4.16}
$$

$$
\frac{dx}{dt} = -\frac{\mu}{r} \sin\theta,
\tag{4.17}
$$

$$
\frac{dz}{dt} = \frac{\mu}{r} \cos\theta + \gamma g
\tag{4.18}
$$

As in Eq. (4.15) the change in the scroll ring radius depends on the combination of the intrinsic normal velocity and the perpendicular component of the induced drift

velocity ($\mathbf{G}_\perp$) while Eq. (4.16) shows that the ring filament reorients due to the presence of the torque on the ring which in turn is due to ($\mathbf{G}_\perp$) when $\theta \neq 0°, 180°$ [Fig. 4.15(b)–(c)]. For $\theta = 0°$ or $180°$, θ remains ($d\theta/dt = 0$) [4.15(b)–(c)]. Eqs. (4.17)–(4.18) describe the translation of the ring due to the binormal velocity and the parallel component of the induced drift velocity ($\mathbf{G}_\parallel$). Note that both r and θ also affect the rate of their own changes and the translation.

Part I

Scroll wave instabilities

Chapter 5

Methods

In this chapter, we first describe the methods employed in the experiments on instabilities of scroll waves in the BZ reaction using optical tomographic observation. The three-dimentional (3D) wave structures were reconstruced and presented using isosurface plots. The filaments of the scroll waves were evaluated for interpreting their instabilities. In the following sections, the procedure for reconstructing tomographic images will be described. The mathematical details are given in the appendix. The experimental studies were accompanied by 3D numerical simulations which were performed by Gert Lindner and Prof. Markus Bär, Physikalisch-Technische Bundesanstalt, Berlin. We explain the numerical methods in the last section.

5.1 Preparation of the Belousov-Zhabotinsky reaction

We used the ferroin-catalyzted Belousov-Zhabotinsky (BZ) reaction embeded in argarose gel as the excitable medium. The BZ solution was prepared from stock solutions of 1.0 M malonic acid (Merck), 1.0 M $NaBrO_3$ (Merck), 5 M H_2SO_4 (Riedel-de Haën), and 25 mM ferroin. The stock solutions of malonic acid and $NaBrO_3$ were prepared by dissolving the solid chemicals with deionized water (conductivity $\approx 0.056\,\mu S\,cm^{-1}$). To produce 50 ml of 25 mM ferroin (in 25 mM H_2SO_4),

Table 5.1: Initial concentrations of the BZ reaction used in the experiments. Recipe I was used for the study of the instabilities of scroll waves. In a thin layer system, it supports a meandering spiral wave with a sufficiently low wave velocity (11 μm s^{-1}) for tomographic observation. Recipe II was used in the experiments on scroll ring dynamics in an advective field presented in part II. A 2D medium of recipe II exibits rigidly rotating spiral waves yielding, in general, a well-known starting condition for study of external forcing in excitable media.

recipe	H_2SO_4 (mM)	$NaBrO_3$ (mM)	malonic acid (mM)	ferroin (mM)
I	130	40	40	0.5
II	200	50	50	0.5

0.3475 g $FeSO_4$ (Riedel-de Haën) and 0.7434 g o-phenanthrolin (Riedel-de Haën) were dissolved in 2.5 ml 0.5 M H_2SO_4 and a suitable volume of distilled water. The mixture was well stirred about half an hour before it was stored in a light-protected bottle.

The initial concentrations of the reactants for different sets of experiments, i.e., I: scroll wave instabilities and II: scroll rings in an advective field (presented in part II), are compiled in table 5.1. To prevent any hydrodynamic perturbation of the chemical wave pattern, the reaction was embedded in a 1.0% w/w agarose gel (Type VII, Sigma) with a low gelling temperature (26°C). Furthermore, a surfactant, 0.05 mM sodium dodecyl sulfate (SDS, Fluka) was added to the reaction medium to reduce the production of CO_2 bubbles by the BZ reaction.

To prepare 10 ml of the reaction mixture, 0.1 g of agarose were mixed with deionized water and boiled until the solution became transparent. When the solution cooled down to $60 - 70$°C, the water lost by evaporation was compensated by addition of suitable volumes of deionized water at room temperature. After water compensation, the gel had cooled down to about 40°C. Then SDS and all of the reactants were mixed with the agarose solution to yield a BZ medium at a temperature of about 36°C. The liquid BZ solution was poured into the reactor before the gel was formed at 26°C.

5.2 Initiation of scroll waves

To study the dynamics of meandering scroll waves, a series of experiments was performed using a BZ reaction with initial concentrations according to recipe I in table 5.1, which in 2D generates meandering spiral waves. Their low propagation velocity (11 μm s^{-1} [48]) makes them suitable for detection by optical tomography [8, 48]. Due to its optical and chemical properties (for details see section 5.3), we chose a fluorinated ethylene propylene (FEP) cylinder as the reaction cuvette. To avoid interaction of adjacent scroll waves, which may affect their intrinsic dymamics, we ignited an isolated scroll wave in the BZ medium.

Initiation of a single scroll wave with straight filament was done using a partition method [96, 97, 8]. A volume of $\approx$ 9 ml of the BZ solution ($28 - 30°$C) was placed into the FEP cuvette (21 mm diameter) yielding a BZ medium of 25 mm height. The medium was partitioned into two parts [Fig. 5.1(a)] by using a thin rectangular plastic plate (0.1 mm in thickness) cut from a flexible transparency (cellulose acetate) which is typically used on overhead projectors. It is crucial to keep the edges along the partition plate in contact with the wall of the cuvette, leaving no gap between them. Otherwise, two (or more) scroll waves would be created if any part of the initiated wave front, described below, could slip through the gap. To avoid any undesired slipping wavefront, the plastic plate was made $0.1 - 0.2$ mm wider than the inner diameter of the reaction cuvette. Due to its stiffness, the plastic plate ensured an absolute separation of the medium into two parts.

One difficulty in the initiation of a single scroll wave comes from the uncontrollable emergence of sponteneous waves and bulk oscillations that typically occur in the BZ reaction. While the sponteneous waves can interact with the initiated wavefront, the bulk oscillations reset the whole medium. However, both potentially destroy the initiated, desired, wave structures. Shortly after the reaction medium was poured into the cuvette and it was still liquid ($> 26°$C), the number of sponteneous waves usually increased with time; however, the bulk oscillations washed out any waves periodically. Therefore, a successful initiation of a single scroll wave
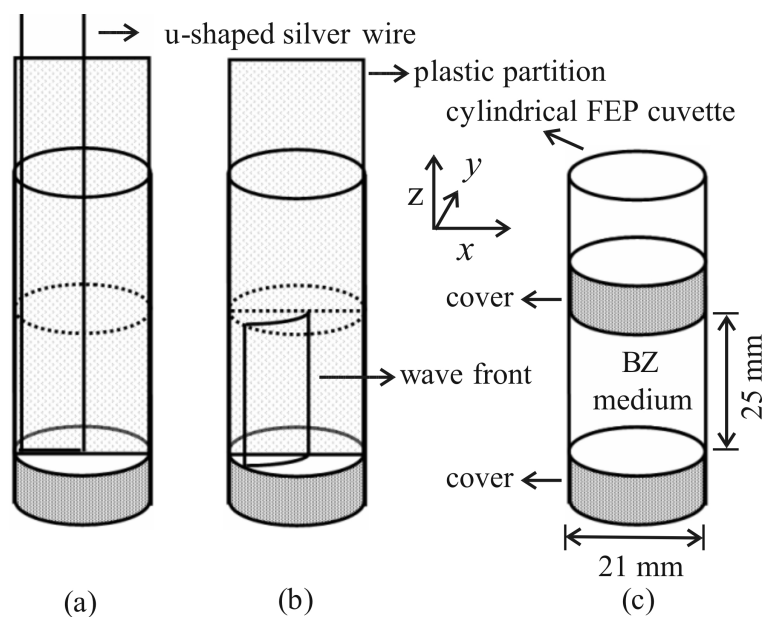
Figure 5.1: Initiation of a single scroll wave. (a) The BZ reaction was poured into cylindrical FEP cuvette and the medium was partitioned by a thin plastic plate. A 1-cm wide wavefront was initiated by using a U-shaped silver wire. (b) The wavefront propagated with one edge touching the wall of the reactor and the other edge was located around the middle of the medium. After removal of the plastic plate, the edge of wavefront at the middle curled in to form a scroll wave. (c) The BZ medium was sealed gas-tightly to prevent inhibitory effects of atmospheric oxygen and resulting spatial gradients of excitability.
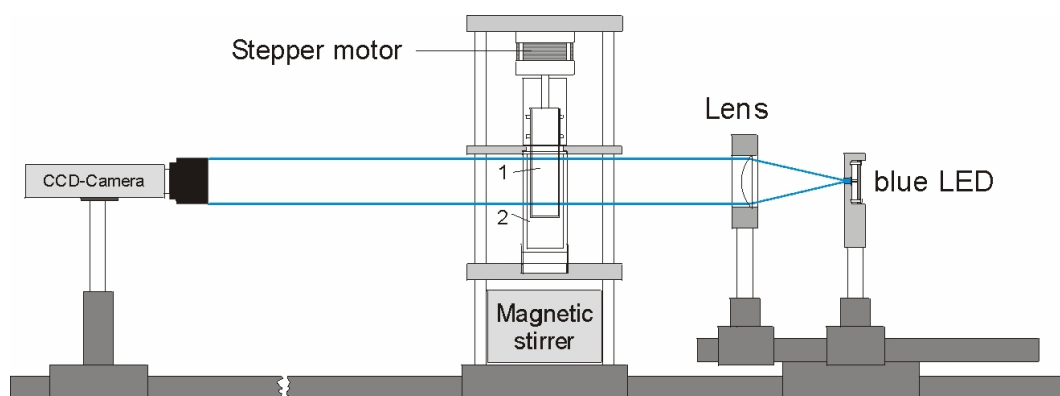
Figure 5.2: Observation setup using optical tomography with a parallel beam technique. The reaction cuvette containing the BZ medium (1) is attached to a stepper motor and placed into a rectangular cuvette (2) filled with a liquid for refractive index matching. A blue light emitting diode (LED) is used as the illumination source and a convex lens provided parallel light shinning through the BZ medium. 2D projections from 100 different angles separated by 1.8° are observed by a CCD camera while the stepper motor is rotating the cuvette synchroneously to the image acquisition.

can be achieved if it is started at a right time (shortly after a bulk oscillation clears the medium) and the initiation takes a short time (before any sponteneous wave destroys the desired structure). Once a scroll wave was created, it emitted wavefronts to the entire medium which, in turn, prevented the occurrence of any sponteneous waves and bulk oscillations.

To make the initiation reliable, a slab of wave front ($\approx$ 1 cm width, 25 mm height) was induced by using a U-shaped silver wire (0.5 mm diameter) [Fig. 5.1(a)], instead of initiating a small cylindrical wave front with a straight silver wire [96, 97, 8]. Using a straight wire, it takes a certain time until one edge of wave front reaches the wall of reactor and the other is located around the middle of the medium. With the method presented here, both horizontal and vertical parts of the U-shaped wire excited a thin slab of the medium where the wire was slowly immersed into and removed from the cuvette. A vertical edge of the wave front touched the wall of the cuvette immediately after it was initiated [Fig. 5.1(b)] while the other was located around the middle of the system. Shortly after the plastic partition was carefully removed, the free edge of wave front curled in to form a scroll wave. To prevent the inhibitory effect of atmospheric oxygen [109, 110, 30] and resulting spatial gradients of excitability [8], the medium was finally sealed gas-tightly shortly after creation of the scroll wave [Fig. 5.1(c)].

5.3 Tomographic observations

The dynamics of the scroll waves were observed in a tomographic setup (Fig. 5.2) which utilized a parallel beam technique (see appendix). The reaction cuvette was attached to a stepper motor which was built in at the upper part of a tower. Then the stepper motor was lowered until the reaction cuvette was immersed into a transparent rectangular cuvette containing a liquid for refractive index matching. The rectangular cuvette was also connected to a thermostate system to keep the temperature of the BZ medium constant at $22.0 \pm 0.1°$C. A blue light emitting diode (LED, wavelength = 470 ± 50 nm where the difference of absorption of ferroin and ferriin is high [42]) was used as the illumination source. A convex lens (focal

length = 10 cm, 4 cm diameter) caused the light to shine parallel through the BZ medium.

In tomography, many 2D projections from different views of an object are acquired to reconstruct a 3D structure. We applied this principle by using a single CCD camera and rotated the sample by a stepper motor to get 2D projections from different angles. During the acquisition, the video signal from a CCD camera (Hamamatsu, C3077, 25 frame s^{-1}) was digitized using a frame grabber card (Pulsar, Matrox, 768×572 pixel^2, 8 bit pixel^{-1}), while the reaction cuvette was rotated by a stepper motor at a rate of 25 steps s^{-1} (synchronized with the image acquisition) and an angular resolution of $1.8°$. Within 4 s, 100 2D projections, each separated by $1.8°$, were continuously acquired and used for the reconstruction of one image of the scroll wave. Then the acquisition was paused for 36 s before the next sampling so the delay time between two different samples of the scroll wave was 40 s. The spatial resolution of the 2D projections and the later reconstructed 3D images was 0.1 mm pixel^{-1}. The software for image acquisition and motor controller was written in C programming language and the graphic user interface was buit using a graphic language LabView (National Instruments).

Because it must be observed from many different angles, the BZ medium was placed in a circular cuvette. Light may refract when it propagates from one medium to another medium with different refractive index. Therefore, a refraction of the illumiation at the circular cuvette may occur and can cause a serious problem in the 3D reconstruction process. Winfree [115] has proposed a solution to overcome this problem by using a transparent circular cuvette which has the same refractive index as that of the BZ medium ($\eta = 1.34$) and immersing the circular cuvette into a transparent rectangular cuvette which is filled with a liquid for matching the refractive index as show in Fig. 5.3. With this technique, parallel light propagates through the system without any refraction problem. Besides its refractive index ($\eta = 1.34$), the cuvette must have both an excellent chemical resistance and a high transparency. Therefore, we chose a cylinder made from fluorinated ethylene propylene (FEP) as the reaction cuvette since the refraction index of this polymer is $\eta = 1.34$. As index matching liquid, we used 0.04 g ml^{-1} K$_2$SO$_4$ solution, which
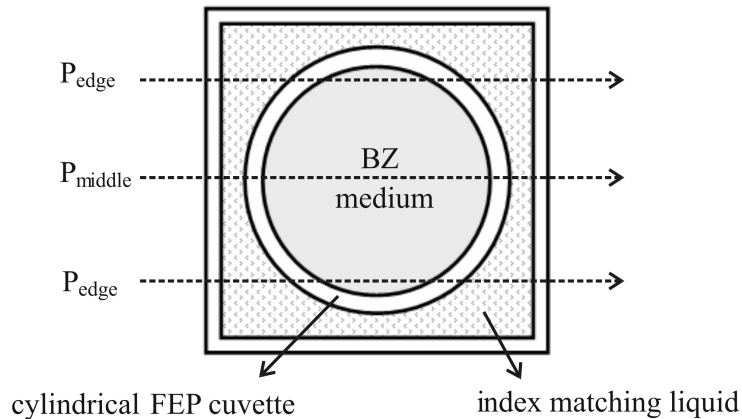
Figure 5.3: Illumination through a horizontral section of the refractive index matching system. To avoid refraction of the illumination, the reaction cuvette (fluorinated ethylene propylene, FEP, cylinder) and the index matching liquid (0.04 g ml^{-1} K$_2$SO$_4$ solution) were chosen to have the same refractive index as that of the BZ medium, i.e., $\eta = 1.34$. Some ferroin was filled into the index mathching liquid to homogenize the optical density across the section.

gives the refractive index $\eta = 1.34$ exactly the same as that of the BZ medium.

Now we consider the illumination through a horizontral section of the reaction cuvette as shown in Fig. 5.3. 3D images of the wave pattern can be reconstructed only when the observed 2D projections of the wave fronts (ferriin, blue) have a good contrast with respect to the background (ferroin, red). It means that the intensity of the illumination should be high enough to give a high value of transmittance at the middle of the section (P$_{\texttt{middle}}$ in Fig. 5.3) where the path length of the light in the BZ medium reaches the maximum value, i.e., the inner diameter of the cuvette. However, a sufficient illumination for the middle of the cuvette causes a saturation of light in the area near the edges of the cuvette (P$_{\texttt{edge}}$ in Fig. 5.3) due to the reduction of the path length towards zero. To get an appropriate transmittance for the whole section of the reaction cuvette, we homogenize the optical density across the section by filling a volume of ferroin into the liquid for matching the refractive index. This way, the reduction of the absorbance in the BZ medium along the distance from the center will be compensated by the absorbance of the ferroin in the index matching liquid. Therefore, the saturation of light in the area near the edges is prevented.
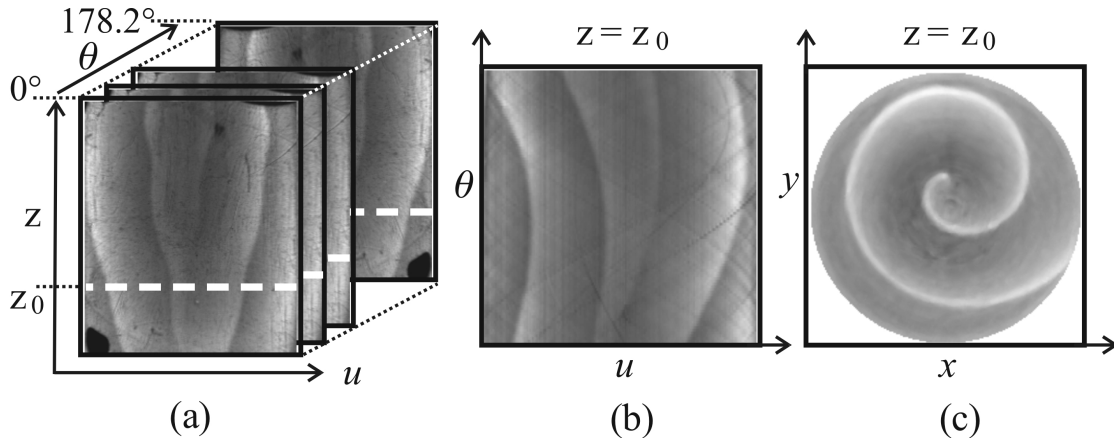
Figure 5.4: Tomographic reconstruction using a convolution technique. 3D Carthesian coordinates (x, y, z) were set for the BZ medium and its reconstructed images. (a) As projected in rotating coordinates (u, v, z), 2D projections (u, z) of the medium correspond to the Radon line integrals at different angles θ (from 0° to 178.2°). As an example, the dashed lines at $z = z_0$ show 1D lines of pixels which were taken to build a sinogram (u, θ) (b). To reduce noise and enhance the image contrast, the sinogram was convoluted with the Shepp-Logan filter before it was used in the reconstruction process to produce (c) a horizontal slice of the scroll wave.

5.4 Tomographic reconstruction

To reconstruct 3D images of a scroll wave, we used a convolution technique of tomographic image reconstruction which is described in the Appendix. For each sample, 250 (25 mm × 10 pixel mm^{-1}) horizontal slices through the scroll wave were reconstructed individually and later stacked to form a 3D volume of pixels.

Figure 5.4 shows an example of a tomographic reconstruction. We set 3D Carthesian coordinates, (x, y, z), for the BZ medium in the cuvette (Fig. 5.1) and its reconstruction [an example of a horizontal reconstructed slice is shown in Fig. 5.4(c)]. Each pixel in the observed projections [Fig. 5.4(a)] corresponds to the Radon integral along a line passing through the medium. To reconstruct a horizontal slice, e.g., at $z = z_0$, lines of pixels [dashed lines at $z = z_0$ in Fig. 5.4(a)] in the 2D projections from all angles of a half rotation (from 0° to 178.2°) were used for the calculation. A stack of these lines of projections [Fig. 5.4(b)] is called a sinogram aor shadowgram. A spatial convolution of the sinogram with the Shepp-Logan filter was performed to reduce noise and enhance the contrast of the re-

constructed image. The reconstructed image [Fig. 5.4(c)] of the filtered sinogram was obtained by using the procedure "RIEMANN" in IDL (IDL: the interactive data language, Research System, Inc.) which performs an inverse discrete Radon tranformation with a linear interpolation.

In experiments using a thin layer of the BZ reaction, wave patterns are generally recorded as grayscale images with a brightness resolution of 256 levels (8 bits) for both presenting purpose and further evaluation of the wave dynamics. For 3D experiments using the tomographic observation, horizontal slices of the reaction volume which are reconstructed and directly saved as 8-bit images can give the details of the wave structure, e.g., a spiral wave [Fig. 5.5(a)]. However, this may create artificial stripes in the whole 3D volume especially in vertical slices as in Fig. 5.5(b). To minimize the occurrence of artificial strips [results as in Fig. 5.5(c)], we reconstructed the horizontal slices (in each individual 3D image) with a higher resolution (32-bit) and stacked them to form a 3D reconstructed set of data (F). Then we searched for the minimum (F_{min}) and maximum (F_{max}) of the data set F. Finally, each pixel of the 32-bit data set $F(i,j)$ was converted to an 8-bit one $f(i,j)$ (to reduce the amount of saved data and for a visualization purposes) by using Eq. (5.1).

$$f(i,j) \;=\; 255\; \frac{F(i,j) - F_{min}}{F_{max} - F_{min}} \tag{5.1}$$

To present the scroll wave, the image contrast was further enhanced by a calculation of the difference between two temporally adjacent samples. This method improves the image contrast and subtracts the background of the images. 3D structures of the scroll wave can be illustrated as isoconcentration surfaces using the marching cube algorithm [116, 117, 118]. To create such a surface of the scroll wave, we used a procedure named "SLICER3" provided in IDL. The difference images and the isoconcentration surfaces are depicted in the Results section.
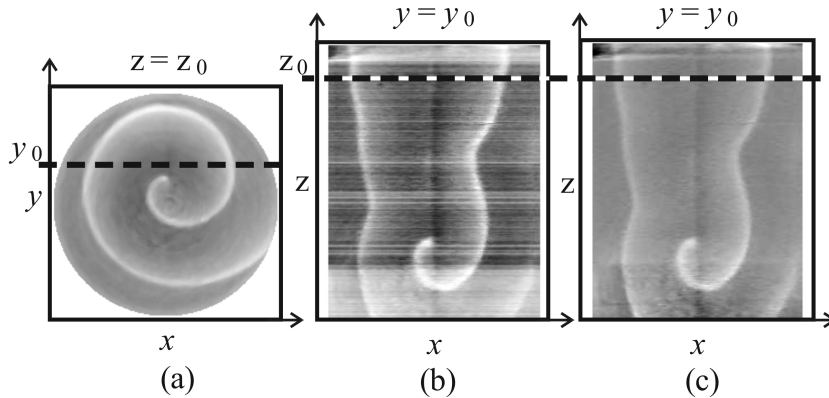
Figure 5.5: 2D slices cutting through a reconstruced scroll wave. If (a) each horizontal slices is reconstructed using 8-bit resolution, artificial stripes will appear in (b) vertical slices. The problem can be avoided as in (c) if the horizontal slices are produced using 32-bit resolution and using a volumewise conversion to 8-bit images. The dashed line $y = y_0$ in (a) and the line $z = z_0$ in (b) and (c) indicate the position of the presented vertical and the horizontal slices, respectively.

5.5   Evaluation of scroll wave filaments

To study the dynamics of a scroll wave in detail, we have developed a software for estimating its filament. Subsequently, we calculated the filament length to characterize the instabilities of the scroll waves.

Since each scroll wave can be viewed as a stack of spiral waves in 2D slices, we defined the filament as the line connecting the centers of spiral cores of the spirals in the slices. The cores, in turn, are the areas which are not invaded by the waves during a single revolution of the spirals [42]. As the images consist of bright wave fronts propagating on a darker background, the core will never be as bright as the wave front at any rotation of the wave. Therefore, the spiral core will appear, in principle, as the darkest region in the superposition of images of the spiral wave completing a single rotation.

However, the situation is more complicated in the real case, since the overlaid images contain some imperfections. These imperfections may be due to light scattering from bubbles produced by the BZ reaction as well as wave fronts that fail to fill up the complete area outside the spiral core [Fig. 5.6(a)]. The latter arise from image acquisitions with discrete delay time which is unavoidable in the experiments.

To evaluate a spiral core, we first estimated the wave period by observing the mean gray level at a small fixed area (5×5 pixel^2) located about one wavelength away from the spiral tip. This mean gray level oscillated with time and it reached a local maximum when the bright wave front entered the observed area. The interval between two adjacent local maxima gives the wave period. We found that the period in the experiment decreased with time (Fig. 6.1 in the next chapter). The images of the spiral wave during a single rotation were overlaid using Eq. (5.2). Each single pixel $s(i, j)$ in the superposition image was determined as the maximum value (max) of the gray level at the same position $f(i, j)$ in the series of n images.

$$s(i, j) \quad = \quad \max\{f_1(i, j), \; f_2(i, j), \; f_3(i, j), \; \ldots, \; f_n(i, j)\} \qquad (5.2)$$

Since the wave fronts are brighter than the background, the spiral core appeared as a dark area. Note that dark areas [their gray level $s \leq 10\%$ of 255, denoted by white envelopes in Fig. 5.6(a)] also appear outside the spiral core due to some imperfections in the images, as described above.

Since a spiral core is a dark area on a bright background, its edge (where the gray level s changes abruptly) can be determined by using an edge detection operator, e.g., gradient operators and second derivative operators. In our case, the Sobel filter, which is a gradient operator, was used. The superposition image [s from Eq. (5.2)] was convoluted [Eq. (5.3)] independently with two gradient filters, to determine the gradients in horizontal (G_x) and vertical (G_y) directions, respectively.

$$G_x = \begin{bmatrix} 1 & 0 & -1 \\ 2 & 0 & -2 \\ 1 & 0 & -1 \end{bmatrix} * s \quad , \quad G_y = \begin{bmatrix} 1 & 2 & 1 \\ 0 & 0 & 0 \\ -1 & -2 & -1 \end{bmatrix} * s \qquad (5.3)$$

Subsequently, the magnitude of the edges in the image, m, was estimated using Eq. (5.4)

$$m(i, j) = \sqrt{G_x^2(i, j) + G_y^2(i, j)} \quad \approx \quad |G_x(i, j)| + |G_y(i, j)| \,. \qquad (5.4)$$
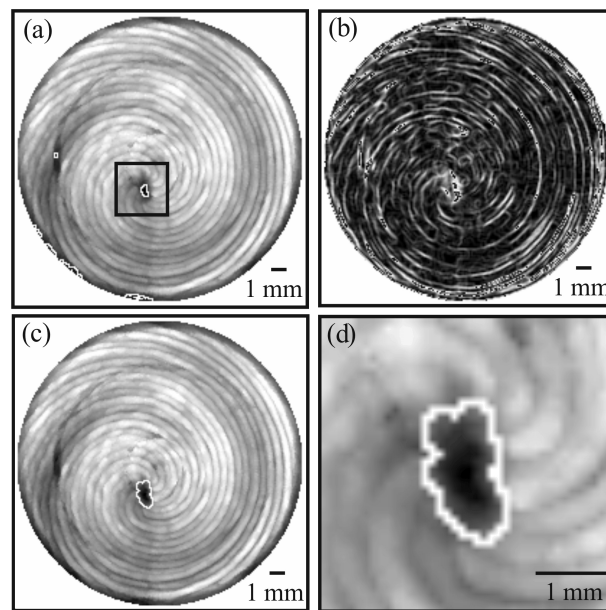
Figure 5.6: Evaluation of spiral core in a 2D slice cutting through a scroll wave. (a) Superposition of spiral wave images during one rotation. The white envelopes show dark areas (with gray level $s \leq 10\%$ of 255) which were also found outside the expected spiral core (in the small rectangle). (b) The edge strength was detected by applying the Sobel filter to the superposition image. (c) The spiral core (i.e. in the white envelope) and (d) its magnification were detected in the evaluation process.

The edge of the core is a loop where the edge magnitude (m) reaches a local maximum. This means that the edge is an envelope of the "ridge" around the core. However, edges of the imperfections may also appear as artifacts in the overlaid image [Fig. 5.6(a)] and in its edge-value image [Fig. 5.6(b)].

To detect the edge of the spiral core correctly, we first exclude the artifacts by considering only the points in a small region of interest [ROI, the rectangles in Fig. 5.6(a)] which contains the spiral cores. Therein, we search for "core seeds" which are located in the ROI and whose gray level $s \leq 10\%$ of the maximal gray level in the ROI. We defined the core seeds whose edge magnitude m is minimum as the initial core and allow the core to grow until the core edge is reached. Step by step, the core grows if the edge magnitude m of the nearest 8-connected neighbors is greater than that of the core – i.e., the edge of growing core climbs to the ridge. With this algorithm, the core growing stops when the magnitude m of all the points along the edge reaches a local maximum. Figure 5.6(c)–(d) shows an edge of a spiral core and its magnification (the white loops) which was successfully detected.

Once the spiral cores in all 2D slices were detected, the centers of the cores can be calculated as the center of mass and connected together for a whole 3D image to form the wave filament. Finally, 3D visualisation of the filament was done and the filament length was calculated as a sum of small line segments connecting all of the spiral core centers.

5.6 Numerical methods

To connect the experimental observations with theoretical analysis of scroll wave instabilities, 3D numerical simulations were performed. The Barkley model [25] [Eq. (5.5)] with the ratio of diffusion coefficients of inhibitor and activator $D_v = 0$ was used because it is the only model where a linear stability analysis of straight scroll waves has been performed [104, 91] and simulation results can thus be related to known instabilities (see section 4.3). As mentioned in section 3.2, the Barkley

model reads:

$$\begin{aligned}
\frac{\partial u}{\partial t} &= -\frac{1}{\epsilon}u(u-1)(u-\frac{v+b}{a}) + \nabla^2 u \\
\frac{\partial v}{\partial t} &= u - v + D_v \nabla^2 v.
\end{aligned} \tag{5.5}$$

For the simulations, the parameters were set as $b = 0.01$, $\epsilon = 0.025$, while a was varied. To mimic the ageing in the experiment, a was decreased step-wise in equidistant steps of $\Delta a = 0.01$ from $a = 0.68$ to $a = 0.56$.

The calculations were performed using an explicit Euler forward integration scheme [26] in a volume of $25.6 \times 25.6 \times 26.0$ (dimensionless units) with zero-flux boundary conditions on the walls. The spatial and temporal resolutions were set as $\Delta x = 0.2$ and $\Delta t = 3.75 \times 10^{-3}$. To study the stability of the scroll waves, small $cos(kz)$ perturbations were added to the scroll waves at the beginning of the simulation [119].

The visualization of the scroll waves was done using Mathematica (Wolfram Research). Isoconcentration contours were ploted at $u = 0.5$ and filament was defined as the intersection of the contours $u = 0.5$ and $v = a/2 - b$ as in reference [26]. As in the experiments, we have measured the filament length in the course of the simulations.

Chapter 6

Results and Discussion

In this chapter, we present the results from experimental and numerical studies of scroll wave instabilities. The dynamics of scroll waves have been observed by optical tomography. By considering the 3D structures of the scroll wave and the filaments evalulated, we interpreted the dynamics of the scroll wave as undergoing two different instabilities, namely 3D meandering and negative line tension instabilities. The 3D simulations using the Barkley model reproduced the qualitative dynamics of the scroll waves found in the experiments.

6.1   Experimental results

The experiments have been done using the BZ reaction with recipe I compiled in table 5.1. To observed the intrinsic dynamics of the scroll waves, the experiments have been conducted in a closed system in which the reaction aged. Feeding fresh chemical solutions continuously has been utilized to avoid ageing of the BZ reaction typically in a thin layer (thickness up to a few millimeters) [46]. However, in a 3D system as used in the present study (25 mm height, 21 mm diameter), feeding would create gradients of chemical concentration which can alter the dynamics of the scroll waves.
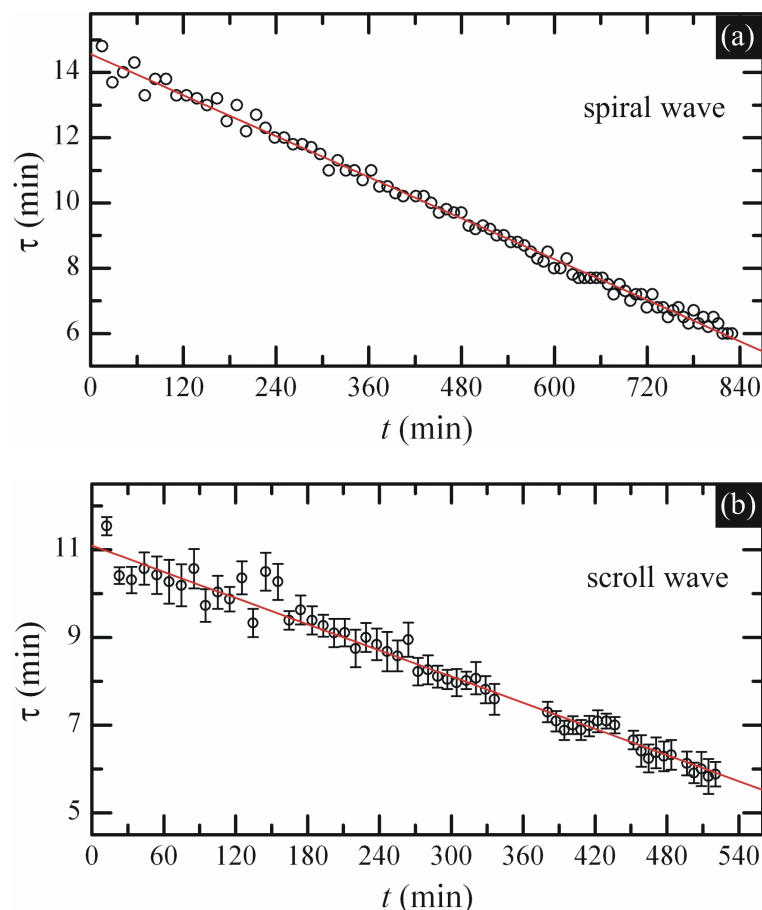
Figure 6.1: Wave period in ageing BZ media in (a) a spiral wave and (b) a scroll wave. Circles and lines represent the measured values and linear regressions, respectively. In (b), the period of the scroll wave was taken as the mean value of the periods of spiral waves in different horizontal slices and ploted with its standard deviation (error bars) which lies in the range of 0.2 – 0.5 min. The initial values of the period in both cases were different due to the faster cooling to a constant temperature at 22°C of the thiner layer. The linear fits show that the decrease rate of the period was 0.01 in both cases.

6.1.1 Ageing of the BZ medium

Ageing of the BZ reaction medium affects the properties of the excitation waves. In a thin layer of medium with the BZ recipe used here, ageing caused a change in the shape of the tip trajectory of a meandering spiral wave [48] [Fig. 3.3(b)]. The ageing also affected the wave period in the 2D as well as the 3D case.

Figure 6.1 shows that both the period of a spiral wave and that of a scroll wave decreased in the course of time. Linear regressions fit well to the measured data and show that the rate of decrease in the period is about 0.01 in both experiments. Note that at the beginning, the period of the spiral wave was higher than that of the scroll wave. This possibly resulted from the difference in the temperature of the system. The two reaction media were prepared using the same method, i.e., their temperature before placing them in the reactors was about $26 - 30°$C. However, the thiner layer was cooled down to the controlled temperature of $22°$C faster causing a temperature difference at the beginning. This is consistent with the observations, where the periods are seen to shorten with higher temperature [120].

6.1.2 Dynamics of scroll wave structures

Full 3D structures of the scroll wave were successfully reconstructed using an optical tomographic technique. The structures formed during an experiment which was lasted about 9 h are shown in (Figs. 6.2 – 6.6). From left to right in these figures, we present a 2D projection (out of 100) of the scroll wave observed by a parallel beam configuration, a stack of six (out of 250) reconstructed tomographic slices, and finally isoconcentration surfaces. A rendering surface of the whole medium shows the outermost structure of the scroll wave. When the outer part is "peeled off", the inner surface is revealed and it reflectes the shape of the filament. We now describe quanlitatively the dynamics of scroll waves and the shape of the wave filaments based on the isoconcentration surfaces. Further details are given after the quantitative evaluation of the filament presented in the next section.

Figure 6.2 shows the scroll wave at the beginning of the experiment. The
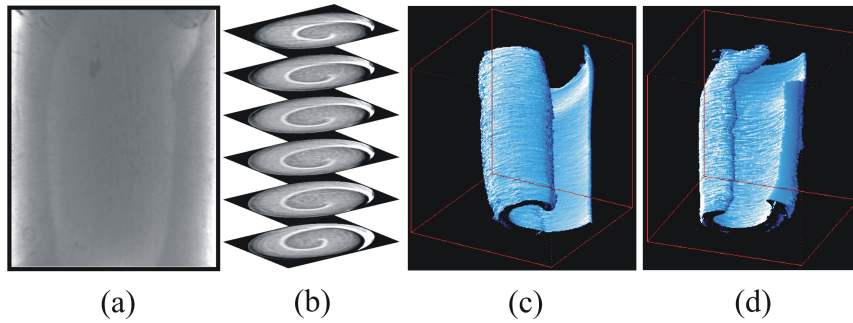
Figure 6.2: Scroll wave in a BZ medium at 12 min. The initiated scroll wave was straight approximately in vertical direction, except for the uppermost part which bent towards the horizontal direction. (a) An observed projection, (b) a stack of six (out of 250) reconstructed tomographic slices; isoconcentration surface of (c) the whole system and (d) the inner cylindrical volume with a diameter of 16 mm. The dimensions of the frames are $21 \times 21 \times 25$ mm^3.
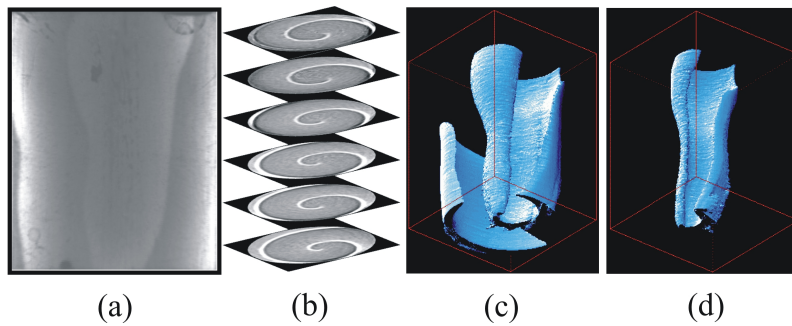
Figure 6.3: Scroll wave at 150 min. The scroll wave aligned to the vertical and the bent part nearly disappeared. The filament and the wave surfaces became moderately wavy in vertical direction. (a) An observed projection, (b) a stack of horizontal slices; isoconcentration surface of (c) the whole system and (d) the inner cylindrical volume with a diameter of 10 mm. Dimensions as in Fig. 6.2.
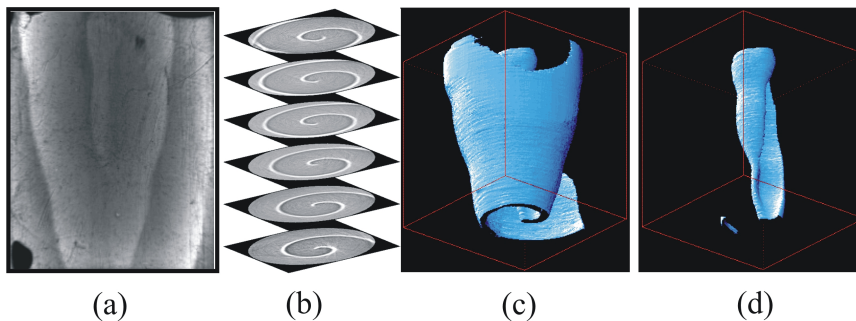
Figure 6.4: Scroll wave at 388 min. The scroll wave was weakly twisted and its filament had a zig-zag form which results in an upward cone shaped isoconcentration contour associated with three small ripples. (a) An observed projection, (b) a stack of horizontal slices; isoconcentration surface of (c) the whole system and (d) the inner cylindrical volume with a diameter of 10 mm. Dimensions as in Fig. 6.2.
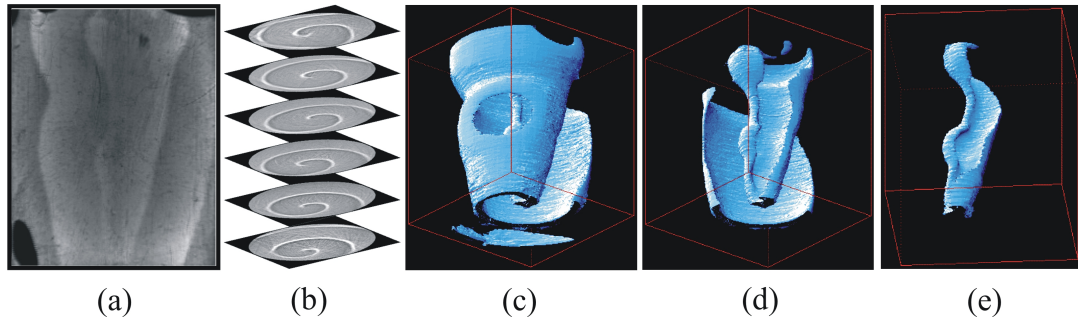
Figure 6.5: Scroll wave at 459 min. The scroll wave became less twisted as the cone shape was less pronounced. The filament has extended leading to pronounced ripples at the wave front. (a) An observed projection, (b) a stack of horizontal slices; isoconcentration surface (c) of the whole system, and the inner cylindrical volumes with a diameter of (d) 16 mm and (e) 8 mm. Dimensions as in Fig. 6.2.
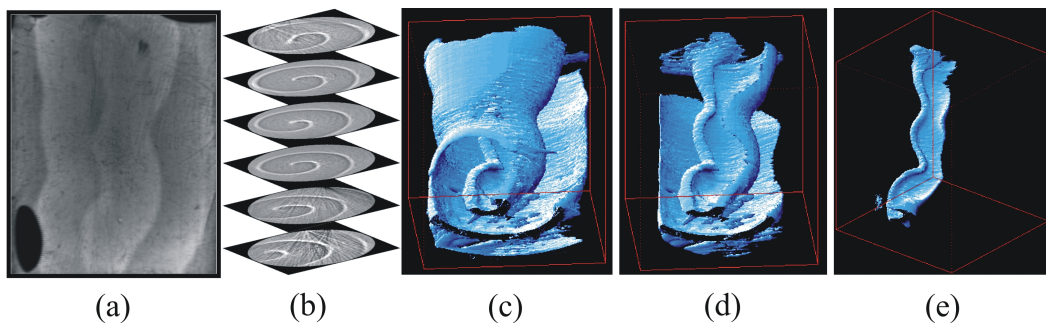
Figure 6.6: Scroll wave at 520 min. The filament has extended leading to pronounced ripples at the wave front. (a) An observed projection, (b) a stack of horizontal slices; isoconcentration surface (c) of the whole system, and the inner cylindrical volumes with a diameter of (d) 16 mm and (e) 8 mm. Dimensions as in Fig. 6.2.

initiated scroll wave is straight throughout almost of its height, except for a small fraction at the top, where the structure bends approximately with a right angle. This bend is unavoidable when the scroll wave is created with the method we used (i.e. under normal atmosphere). During scroll wave initiation, the top surface of the medium interfaced with the atmosphere containing oxygen, which can diffuse into the medium. The oxygen inhibited any wave propagation and created a thin inexcitable layer at the upper part. Soon after the medium was sealed, the oxygen was consumed and the thin layer became excitable. Therefore, the horizontal free edge of wave front under the quiescent layer can propagate into this layer and form the bent part of the scroll wave. This bent part shrunk and straightened as seen in Fig. 6.3 which shows the scroll wave at 150 min. The scroll wave aligned approximately in the vertical direction, however, its surface was wavy.

A twisted wave also developed during the experiment. At 388 min (Fig. 6.4), the scroll wave had the shape of an upward cone, which means that the scroll wave was twisted and the phase of the uppermost spiral was about π ahead of that of the bottom spiral. The zig-zag shaped filament indicates three small ripples on the cone-shaped wave front. The twist rate (ratio between the turn and the height of the system) which is about a half turn of spiral per 4 wavelengths. Numerical simulations using the Oregonator model showed that a twisted wave can cause a straight filament to deform to a helical shaped one if the twist rate is higher than 0.6 turns wavelength^{-1} [93] due to the twist-induced instability. Using this prediction, the twists (rate $\approx 0.5/4 \approx 0.1$ turns wavelength^{-1}) observed in our experiment was very weak so that it may not cause an instability.

An expansion of the filament leading to a snaking shape and more pronounced of the wavy structures on the scroll wave surface was clearly observed late in the experiment as shown in Figs. 6.5 and 6.6. At the same time, the twist of the wave decreased as the upward cone decayed towards a cylindrical form [see (c) in Figs. 6.4 – 6.6].

Even though the surfactant sodium dodecyl sulfate, was used for reducing the CO_2 bubble formation, the bubbles could not be completely supressed and they grew with time in such a long run experiment. Due to light scattering, the bubbles

were noticeable after $\approx$ 6 h and appeared as dark objects at the top and bottom of the observed projections [see (a) in Figs. 6.4 – 6.6] and they disturbed the spiral structure and the isoconcentration surfaces of the scroll wave. In the presented experiment, all the bubbles were fortunatly located near the walls of the reaction cuvette, leaving the bulk medium unperturbed.

6.1.3 Evaluation of scroll wave filament

To analyse in detail the scroll wave dynamics described in the last section, the 3D structures of the scroll wave filaments have been extracted and their temporal development is illustrated in Fig. 6.7. The visualization has been depicted from two perpendicular views for each point in time. The deformation of the filament can be evidently seen from the yz face of the medium while the shape of the filament from the xz face becomes more straight in vertical direction. This indicates that the deformation occurred mainly in a flat plane.

The shape of the scroll wave surfaces and the form of the filaments are not sufficient to distinguish between the scroll wave instabilties induced by 3D meandering and negative line tension. As shown in section 4.3, both can cause a deformation of a straight filament to a zig-zag, wiggle, or snaking shape. However, the 3D meandering instability can be observed when the filament has a positive tension (i.e., in the absence of the negative line tension instability) which stabilizes a zig-zag shaped filament. By contrast, the negative line tension instability would cause an unlimited increase in the filament length with time. To characterize the 3D instabilities in the experiment, the filament length was measured. Figure 6.8 shows the relative filament length L/L_z (the ratio of the filament length L and the height of the medium L_z) in 3 measurements: L_{3D}/L_z (circles), L_{yz}/L_z (triangles), and L_{xz}/L_z (squares). The ratio L_{3D}/L_z represents the filament length measured in 3D while the ratios L_{yz}/L_z and L_{xz}/L_z show, respectively, the lengths of filament projected onto the yz and xz planes (corresponding to the upper and lower rows in Fig. 6.7). Considering the filament length, we devided the observation into 3 intervals: the first 180 min, 180 – 400 min, and after 400 min.
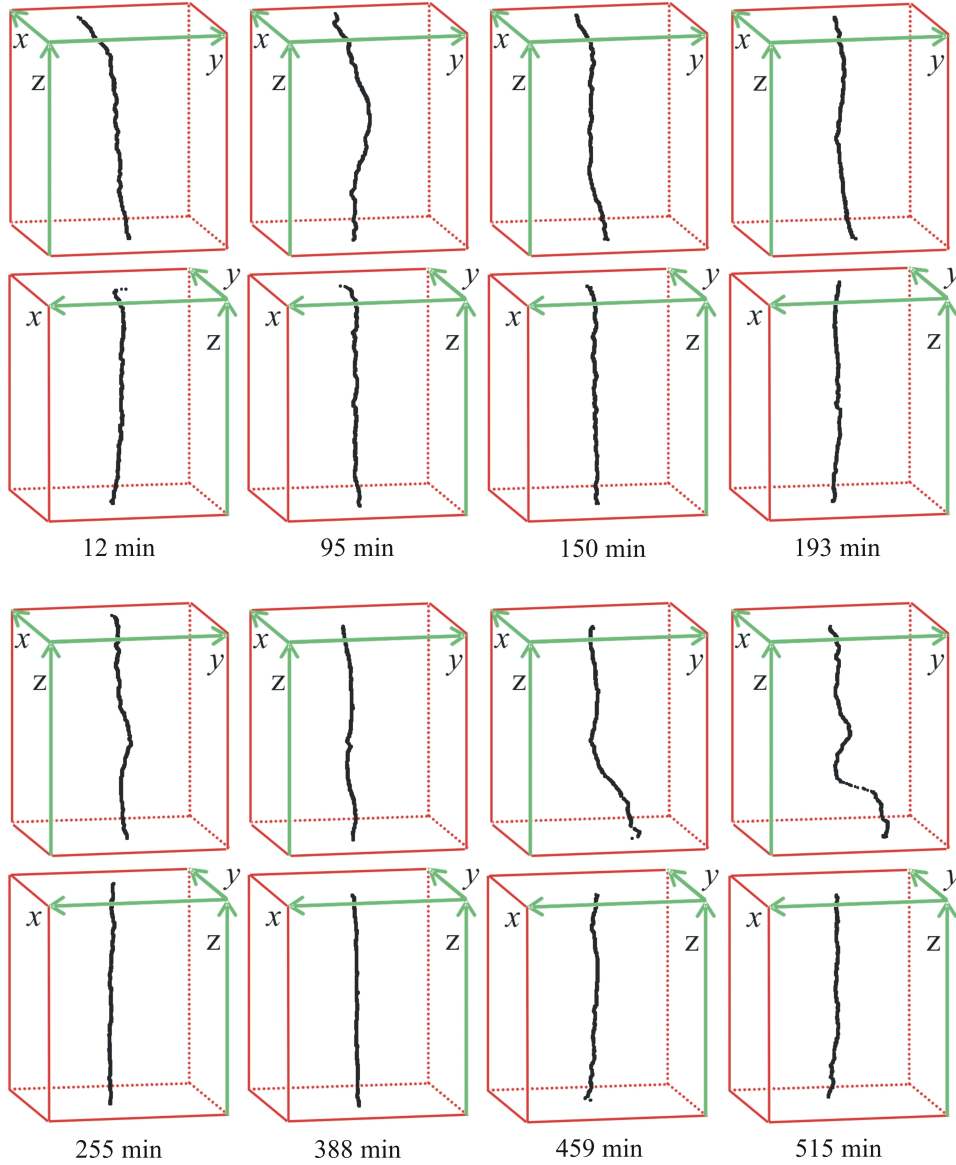
Figure 6.7:   Temporal development of the scroll wave filament in a BZ medium. At each instant, the upper and lower rows present the shape of the filament from the yz and xz faces of the medium. The initial filament (12 min) was slightly tilted from the vertical axis and the uppermost part of the filament curved towards the horizontal. Later (95 – 150 min), this bent part shrunk and straightened. After a transient time of 180 min, the wave filament aligned almost vertically and became zig-zag shaped (193 – 388 min). In the long time limit, however, the filament expanded considerably in the yz face (459 – 515 min). The dimensions of the frames are $21 \times 21 \times 25$ mm^3.
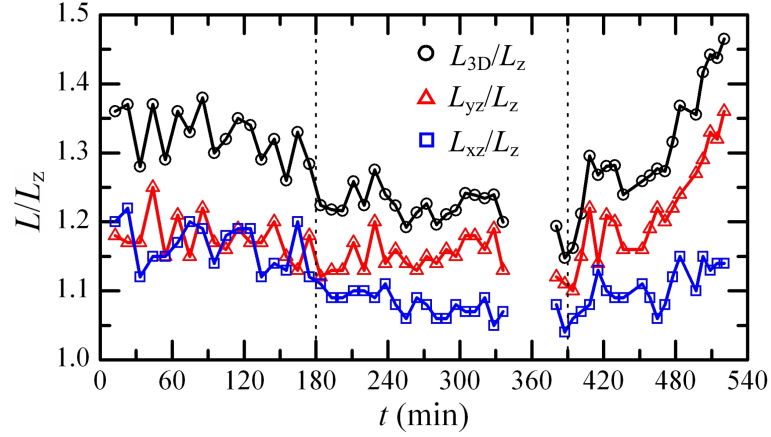
Figure 6.8: Relative filament length of the scroll wave in a BZ medium. L/L_z: the ratio of the filament length L and the height of the medium L_z. Circles (L_{3D}/L_z) represents the relative length measured in 3D, while triangles (L_{yz}/L_z) and squares (L_{xz}/L_z) show the lengths of the filament projected onto the yz and xz planes, respectively. The dashed lines devide the measurments into three intervals: the first 180 min, 180 – 400 min, and after 400 min. In the first $\approx$ 180 min, the relative lengths oscillated and L_{3D}/L_z contracted from 1.35 – 1.2. For $180 < t < 400$ min, L_{3D}/L_z oscillated around $\approx$ 1.2 while L_{xz}/L_z decreased slightly. Finally, in the long term limit, L_{3D}/L_z increased substantially to 1.45 and the increase occurred mainly in a yz plane (L_{yz}/L_z). At $340 < t < 370$ min, the observation was paused for a contrast enhancement purpose (i.e., the illumination intensity and the concentration of ferroin in the index matching liquid were adjusted.). The interval between two points corresponds to the wave period.

At the beginning, the initiated scroll wave exhibited a slightly tilted filament (Fig. 6.7: 12 min), roughly parallel to the vertical axis. Due to the initiation procedure, the uppermost part of the filament curved toward the horizontal, as described in the previous section. During the first 180 min (Fig. 6.7: 12 – 150 min), the filament swung and the curved segment at the top deminished. The filament aligned itself approximately to the vertical axis (Fig. 6.7: 193 min). In this initial period, the relative filament length L_{3D}/L_z shrunk from 1.35 to 1.2 due to the positive line tension of the filament.

For $180 < t < 400$ min, the vertical filament assumed a zig-zag shape moving within a small space around the middle of the medium (in line with predictions for 3D meandering behavior [104, 91]). Note that the zig-zag form (Fig. 6.7: 193 – 388 min) was approximatly flat since the filament looks straight from the xz face. Its relative length L_{3D}/L_z oscillated around ≈ 1.2 while L_{xz}/L_z still decreased. In this interval, the scroll wave was a weakly twisted as mentioned in the last section. The isoconcentration contour in Fig. 6.4 displays some wiggles, which can be explained by the zig-zag shape of the filament.

In the long time limit ($t > 400$ min), the filament has developed a more pronounced modulation (Fig. 6.7: 459 – 515 min) and its length L_{3D}/L_z increased substantially (up to ≈ 1.45). This is an indication of a negative line tension of the filament. The increase in the length and the deformation of the filament shape occurred mainly in the yz plane (L_{yz}/L_z in 6.8 and the upper row in Fig. 6.7: 459 – 515 min).

As the reaction ages during the experiment, the system passes two distinct interesting points. The first of them occurred at $t \approx 180$ min where the tilted filament became vertical. Then ($180 < t < 400$ min), the filament took a zig-zag shape lying in a flat plane. For these first 400 min, the filament had a positive line tension. The filament length tended to be minimized through an adjustment of the tilted filament to the vertical. However, the relative length never reached a minimum value $L_{3D}/L_z = 1$ because the vertical filament also exhibited a flat zig-zag form caused by the 3D meandering behavior. Therefore, these observations describes a 3D meandering instability.

The second interesting point was reached at $t \approx 400$ min. Here the line tension became negative, leading to a considerable and continuous increase in the filament length. Thus, the experiment shows the occurrence of two distinct instabilities, which are corroborated by the numerical simulations presented in the next section.

6.2   Simulation results

The experimental studies were accompanied by 3D numerical simulations which were performed by Gert Lindner and Prof. Markus Bär, Physikalisch-Technische Bundesanstalt, Berlin.

The experimentally observed scroll wave dynamics have been qualitatively reproduced in numerical simulations using the Barkley model [25] with zero diffusion for the inhibitor ($D_v = 0$). A linear instability analysis of a straight scroll wave in this model showed three kinds of scroll wave instabilities as discussed in section 4.3. Therefore, the simulations using the Barkley model provided a connection between the experimental findings and the predicted instabilities. The scenario reported below is generic and also appears in other models with decreasing excitability, including the Oregonator model with $D_v = 0.6$ [58].

As discussed in the last section, the twist of the wave found in the experiment (see Fig. 6.4) was very weak, thus, ruling out a twist-induced instability as the origin of the zig-zag shape. Hence, we started our simulations with a straight untwisted scroll with a small perturbation of the form cos(kz) added and mimicked the ageing of the solution in the experiment by a step-wise decrease in the excitability parameter a. We found a transition from straight scrolls with linear filaments to 3D meandering scrolls with zig-zag shaped filaments as well as a notable stretching of the filament of the scroll wave upon decrease of a (Fig. 6.9). For the reverse simulation protocol (increasing a starting from zig-zag shaped filaments at low values around $a = 0.60$), 3D meandering disappeared at $a_C = 0.68$, roughly in line with the value found in [91].

Similar to the experiment we have measured the filament length in the course of our simulation (Fig. 6.10). During the simulation run, the parameter a has
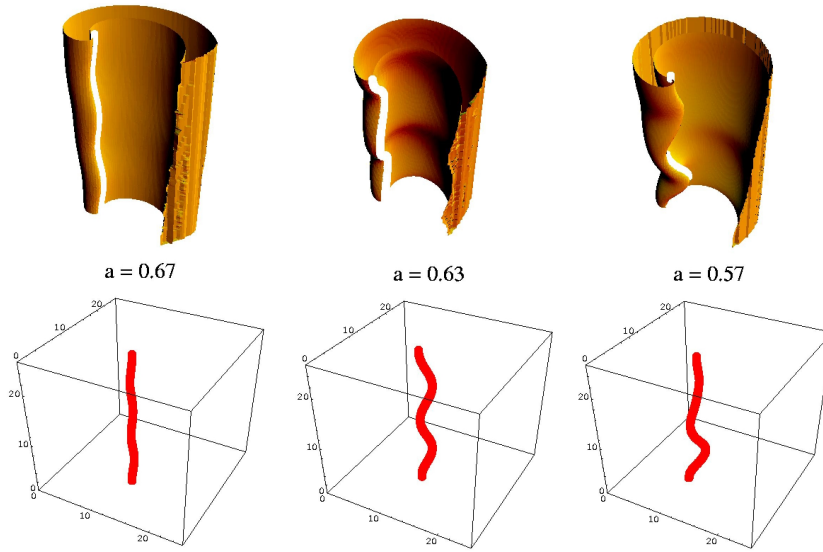
Figure 6.9: Scroll wave surfaces and filaments in the Barkley model. Results for different values of the excitability parameter a, shown are isoconcentration contours ($u = 0.5$) and filament shapes (obtained from the intersection of the contours $u = 0.5$ and $v = a/2 - b$). The left and middle panels show a scroll wave in the 3D meandering regime, the right panel indicates negative line tension and increase in filament length. Parameters: $b = 0.01$, $\epsilon = 0.025$. The volume of the simulation box is $25.6 \times 25.6 \times 26.0$. Numerical parameters: $\Delta x = 0.2$ and $\Delta t = 3.75 \times 10^{-3}$.
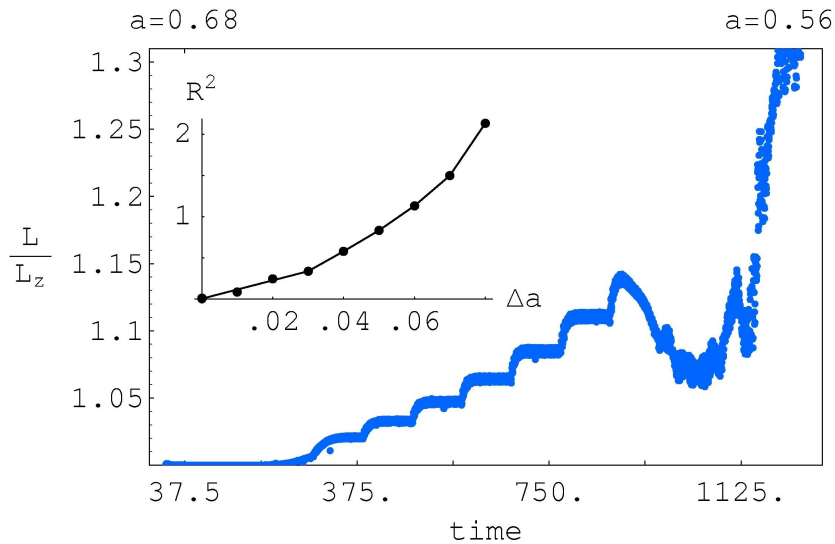
Figure 6.10: Relative filament length of the scroll wave in the Barkley model. The parameter a is decreased in equidistant steps of 0.01 from $a = 0.68$ at $t = 0$ to $a = 0.56$ at $t = 1218$. The inset shows the squared amplitude R^2 of the zig-zag filament vs. the distance Δa to the onset of 3D meandering obtained by a simulation run where a was increased step-wise from $a = 0.60$ to $a = 0.68$.

been decreased step-wise from $a = 0.68$ to $a = 0.56$ in intervals of $\Delta a = 0.01$. We observe a related step-wise change of the filament length as a result of the 3D meandering instability. Stable zig-zag shaped filaments with constant length are formed after short transients after each parameter change. The regular steps disappear below $a = 0.60$ leading to more twisted and initially shorter filaments as well as to irregular oscillations of the filament length. Finally, the filament length increases substantially for $a \leq 0.57$. This phenomenon appears in close vicinity to the negative line tension instability of straight scroll waves found previously at $a \approx 0.565$ [91]. Exploiting the backward run from $a = 0.60$ to $a = 0.68$ with increasing a, we also determined the amplitude R of the 3D meandering instability in dependence on $\Delta a = |a - a_C|$ and found the expected scaling $R^2 \propto \Delta a$ close to the instability (Fig. 6.10, inset).

The simulation results (Figs. 6.9 and 6.10) compared qualitatively well to the experimental findings (Figs. 6.4 – 6.8). After a transient, the scroll wave in the experiment showed initially clear signs of 3D meandering ($t < 400$ min), i.e. a flat moving zig-zag shaped filament with $L/L_z > 1$, but roughly constant. By contrast, the increase of the filament length at long time ($t > 400$ min) is compatible with numerical simulations in the region of negative line tension (Figs. 6.9 and 6.10).

6.3 Summary

We have reported experiments on scroll wave dynamics in an excitable chemical medium using the BZ reaction in an optical tomography setup. Though the reaction was run in a closed container its ageing proceeded only slowly allowing for the observation of different regimes of scroll wave dynamics. Image processing was used to obtain both the isoconcentration surfaces during scroll wave rotation and the approximate shape and length of the scroll wave filaments. These data enabled us to distinguish different characteristic instabilities of straight scroll waves, namely the 3D meandering instability connected with a zig-zag shaped filament and negative line tension instability indicated by a substantial increase in the filament length and a strong bending.

In parallel, numerical simulations show that upon decrease of the excitability (in the experiment due to ageing of the solution) a scroll wave indeed can pass from 3D meandering to a strongly nonlinear regime with irregular length fluctuations and finally a substantial increasing filament length.

Our work shows that optical tomography is capable of detecting instabilities of 3D patterns such as scroll waves. Numerical simulations connect the experiments to the theory of instabilities of scroll waves and suggest a direct relevance of the theory to the dynamics of 3D patterns in the BZ reaction.

Part II

Scroll rings in an advective field

Chapter 7

Methods

In the following sections, we present the methods used in experimental and numerical studies of scroll rings in an advective field. In the experiments, a constant electrical current was applied to the BZ medium while the initial orientation of scroll rings was varied. In the simulations, we used the 2-variable Oregonator model with an additional advective term accounting for a constant electric field.

7.1   Initiation of scroll rings

The BZ medium was prepared according to recipe II of table 5.1 in section 5.1. With this recipe, a 2D system exhibits rigidly rotating spiral waves. Scroll rings were initiated by using a two-layer strategy [101, 48] as shown in Fig. 7.1. Using this method, the unit vector $\mathbf{S}$ ($\mathbf{S}$ is perpendicular to the ring filament and with respect to the sense of spiral rotation, see Fig. 4.11 and section 4.4.1) of the initiated scroll ring is always perpendicular to the interface (the dashed lines in Fig. 7.1) of the two layers. As describted in the next section, an electrical current density $\mathbf{J}$ was applied in a longitudinal direction along the reactor – i.e., $\mathbf{J}$ pointed either to the left or to the right.

For experiments on scroll rings under an applied current described here, we prepared 20 ml of BZ medium (recipe II of table 5.1 in section 5.1). Using the two-layer strategy, two portions of the BZ medium (from the same preparation) were placed in the reactor (as a first and a second layer) at different times while their
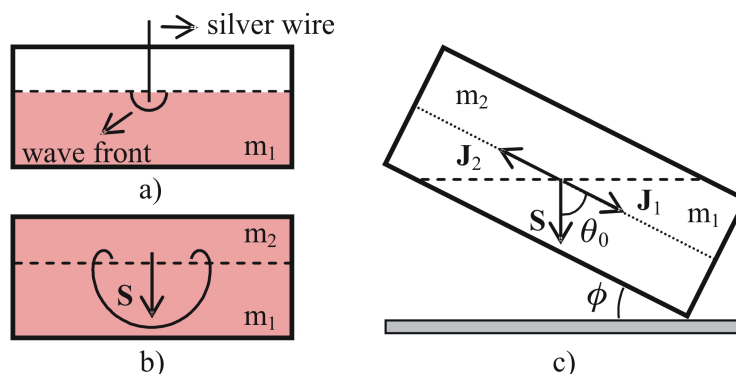
Figure 7.1: Initiation of scroll rings using a two-layer strategy. (a) For an initial orientation $\theta_0 = 90°$, the reactor was set horizontally and it was filled with a first layer m_1 of the BZ medium. A hemispherical wave front was ignited by an Ag wire of 25 mm diameter. (b) When the diameter of the hemispherical font was about $2.5 - 3.5$ mm, a second layer m_2 of the medium was filled at the top of the first layer and subsequently, the circular edge of the hemispherical font curled in to form a scroll ring. The unit vector $\mathbf{S}$ is always perpendicular to the interface (the dashed lines) between m_1 and m_2. (c) Variation of initial orientation θ_0 was achieved by setting the reactor with a tilt angle ϕ with respect to the ground during the initiation. The current density can be applied as either $\mathbf{J}_1$ or $\mathbf{J}_2$ which leads to $\theta_0 = 90° - \phi$ or $\theta_0 = 90° + \phi$, respectively.

temperature were $T = 28 - 30°$C. To do this, the medium was separated into two beakers after the BZ reaction was mixed with agarose ($T = 36°$C). The first beaker of about 10 ml medium was exposed to the room temperature ($T_r = 22 - 23°$C) and a portion of this medium was filled into the reactor as the first layer when it cooled down to $T = 28 - 30°$C. The second portion of the BZ medium (in the second beaker) was kept into a thermal insulator and filled later into the reactor as the second layer.

To initiate a scroll ring with an initial orientation (the angle between $\mathbf{S}$ and $\mathbf{J}$) θ_0 = 90°, the reactor was set horizontally [Fig. 7.1(a) and (b)]. We filled the reactor with a first layer (m_1) of reaction medium ($T = 28 - 30°$C) and then initiated a hemispherical wave front by immersion of an Ag wire of 0.25 mm diameter [Fig. 7.1(a)]. The diameter of the hemispherical front grew with time and when it was about $2.5 - 3.5$ mm, a second layer (m_2) of the medium ($T = 28 - 30°$C) was deposited on the top of the first layer [Fig. 7.1(b)]. The circular edge of the hemispherical front curled in to form a scroll ring. During the initiation, sponteneous waves and bulk oscillations also occurred (as mentioned in section

5.2). A scroll ring with circular filament were obtained only if the second portion of the BZ reaction was poured into the reactor while the initiated hemispherical wave was still unperturbed by any sponteneous waves or bulk oscillations. This limitation caused both the time of growth of the hemispherical front (until the second layer is added) and consequently the scroll ring radius to vary slightly from experiment to experiment.

As in Fig. 7.1(c), the initial orientation θ_0 can be adjusted by setting the reactor with a tilt angle ϕ with respect to the ground during the initiation. The top surface of the first layer aligns horizontally, however, at the tilt angle ϕ with respect to the bottom of the reactor which, in turn, yields a filament plane of the scroll ring that has the angle ϕ with respect to the applied electrical current. The initial orientation θ_0 depends on the direction of applied current density ($\mathbf{J}_1$ or $\mathbf{J}_2$). If the current density points in the same direction as $\mathbf{J}_1$, then $\theta_0 = 90° - \phi$; if $\mathbf{J}_2$ is applied, then $\theta_0 = 90° + \phi$.

7.2 Reactor and observation setup

The influence of an electrical current on the dynamics of scroll rings was studied in a rectangular reactor made from transparent plaxiglas as shown in Fig. 7.2. The BZ medium in a gel was placed in the $12 \times 12 \times 60$ mm^3 reaction volume (BZ) and a scroll ring was initiated as described in the previous section. The longitudinal ends of the reactor chamber were connected to electrolytic compartments (E), which were filled with the BZ reaction of the same composition as that in the main compartment, except for the agarose (i.e., without a gel). The electrolytic compartments were separated from the main reaction chamber by porous glass filters (F) to prevent any perturbation of the scroll ring by gas bubbles formed during electrolysis. The chimneys (C) were utilized to release the bubbles. A constant electrical current was applied via two planar platinum plate electrodes (10×20 mm^2) along the x axis, i.e., pointing from one vertical planar electrode to the other. In most of our experiments, the strength of the current density $J = |\mathbf{J}|$ was set to 40 mA cm^{-2}.
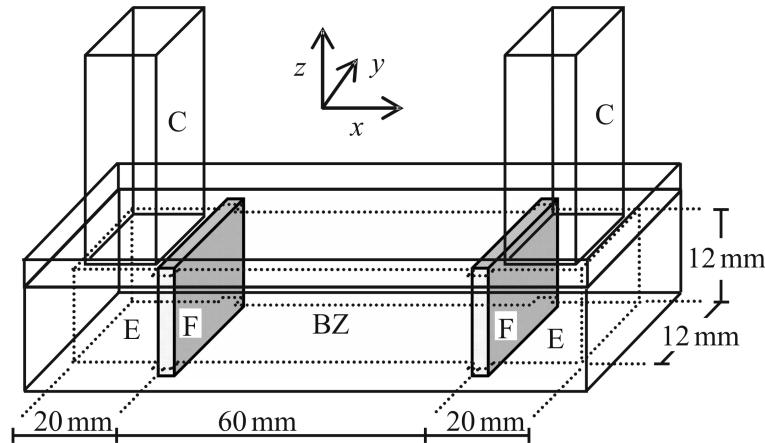
Figure 7.2: Rectangular plexiglas reactor for the study of the dynamics of scroll rings in an electrical current: main volume of $12 \times 12 \times 60$ mm^3 (BZ) for the BZ medium in a gel, electrolytic baths (E) filled with BZ reaction without gel for appling the electrical current via planar platinum electrodes, chimneys (C) for releasing bubbles formed by electrolysis, and porous glass filters (F) preventing the perturbation of the wave structures in the main compartment by gas bubbles that originate at the electrodes.

We observed the dynamics of scroll rings from two perpendicular projections [121] of the wave structures using a single CCD camera as shown in Fig. 7.3. The reactor (BZ) was mounted onto a support and placed into a plexiglass thermostating bath containing water with a constant temperature at 22.0 ± 0.1°C. A mirror was placed with a tilt angle of 45° underneath the reactor allowing a simultaneous observation of the lateral (xz) and vertical (yz) views of the reactor. A white light box (Hama 1634, 2×15 W) was used to illuminate the BZ medium from the side. In contrast to experiments using thin BZ media (0.3 mm thick) [48] where an optical filter (≈ 490 nm) is generally used for image contrast purposes, such an optical filter was not used in the present experiments, since it severely reduces the light intensity and this results in very dark observed projections of such a thick medium (12 mm). As shown in Fig. 7.6, images with a good contrast can be still obtained after image processing was applied.

During the image acquisition, the video signal from the CCD camera (Hamamatsu, C3077) was digitized using a frame grabber card (Pulsar, Matrox, 768×572 pixel^2, 8 bit pixel^{-1}). To reduce noise in the recorded images, a pixelwise temporal averaging of 5 images, which were recorded within 200 ms, was done and
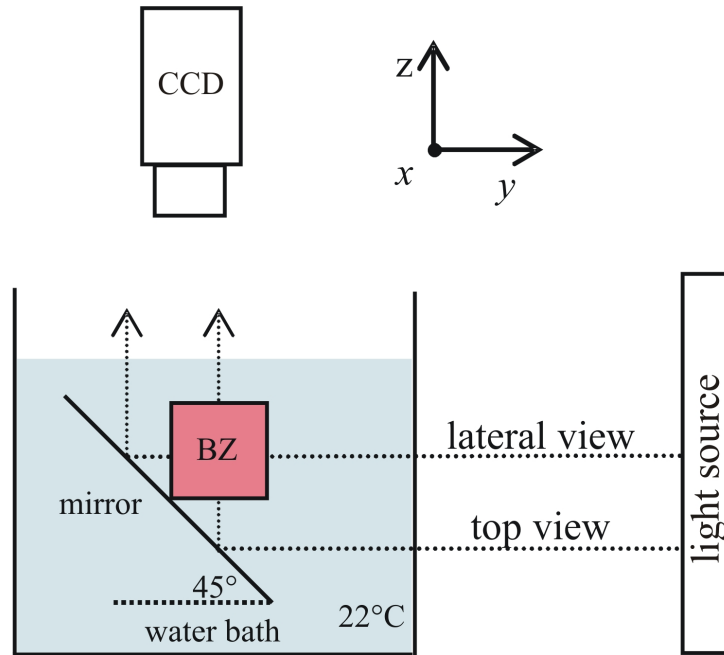
Figure 7.3: Observation setup using a two perpendicular projection technique. The reactor (BZ) was mounted onto a support and placed into a plexiglass thermostating bath at $22.0 \pm 0.1°$C. The reactor was illuminated by a light source placed at one side of the reactor. A 45° tilted mirror fitted underneath the reactor allows a simultaneous observation of the lateral (xz) and top (yz) views of the reactor.

the averaged image was stored permanently. The resolution of the images was adjusted to 0.05 mm pixel^{-1}. The delay time between the stored images was 5 s yielding ≈ 40 images for one wave period of the scroll rings. The software for image acquisition was written in C programming language and the graphic user interface was buit using a graphic language LabView (National Instruments).

7.2.1 Characterization of the reactor

To characterize both the reactor and the electric field inside it, we performed an investigation of the ohmic heating and the homogeneity of electric current in a BZ medium when a constant electrical current was applied to the medium as described in the previous section.

Ohmic heating is unavoidable when a voltage is applied to an ionic solution such as the BZ reaction. We attempted to keep the temperature of the medium at $22.0 \pm 0.1°$C by using a water bath. To monitor the temperature T and its gradient
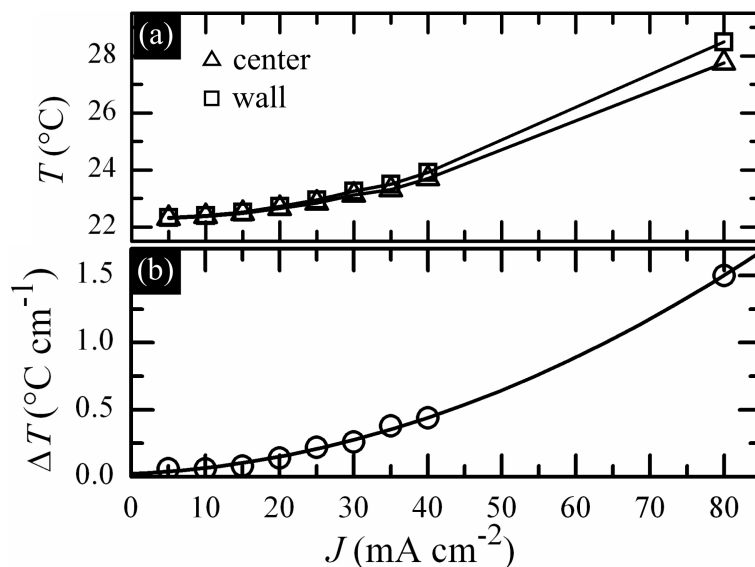
Figure 7.4: Ohmic heating in a BZ medium during an application of electrical current. (a) Temperature T at different applied electrical current densities J. Squares and triangles show the temperature at the center and at an edge of the BZ medium, respectively. The temperature of the water bath was kept constant at $22.0 \pm 0.1°C$. (b) The gradient ΔT of temperature between the center and the edge in (a) (circles). The curve shows a second order polynomial fit of the temperature gradient and the current density.

ΔT in the BZ medium we placed two temperature probes at the center and at an edge of the medium. Even though we immersed the reactor in the water bath, the temperature of the medium at both locations still increased with the strength of the applied current density J as shown in Fig. 7.4(a). The temperature at the edges was lower than that at the center of the medium causing a temperature gradient ΔT which increased gradually with current density J as shown in Fig. 7.4(b). To avoid undesired temperature effects, we performed most of experiments using current densities $J \leq 40$ mA cm^{-2}

The homogeneity of the applied electric current has been tested by measuring the electrical potential in the BZ medium. We measured the electrical potential in the BZ medium for every 5 mm along the 6-cm long medium as shown in Fig. 7.5. At each position (along the x axis), the potential values at 9 points in the same cross section (yz plane) were measured. The electric current density has been set to $J = 10, 20, 30$, and 40 mA cm^{-2} respectively. The minus platinum plate electrode, which was located at the center of an electrolytic bath, was taken as the potential
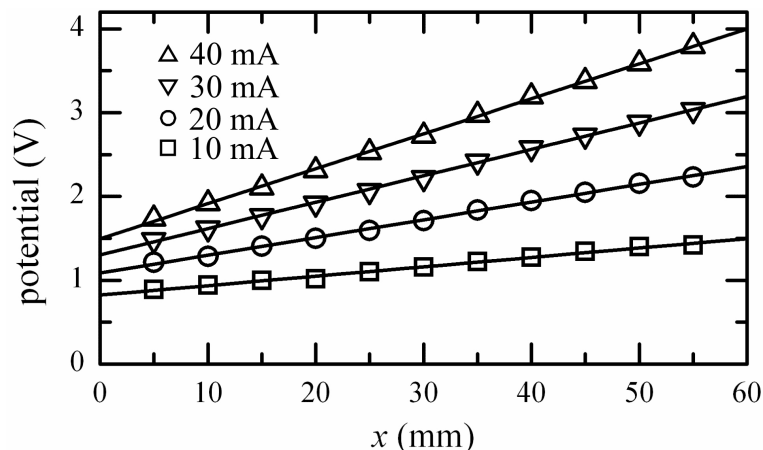
Figure 7.5: Electrical potential along the x axis in a BZ medium. The minus platinum plate electrode was taken as the reference for the potential. The data points show the average potential (calcuated from 9 points) in a yz plane with a standard deviation less than 0.05 V. The strengths of the electric fields can be estimated from the slope of the linear fits (straight lines) as $0.11 \pm 0.0003, 0.21 \pm 0.0003, 0.32 \pm 0.0003$, and 0.42 ± 0.0004 V cm^{-1} at applied electrical current densities J of 10, 20, 30, and 40 mA cm^{-2}, respectively. The temperature of the BZ medium was $22 - 23°$C (room temperature) during the measurements.

reference. To ensure that the probes are correctly located at the desired positions, the reactor was neither sealed nor cooled during the measurements. To avoid too strong heating, we applied the electrical current for 5 s and paused for at least 20 s before the next measurment began. Therefore, the temperature of the BZ medium was at room temperature $(22 - 23°$C$)$ during the measurements. The results show that the potential was homogeneous in a yz plane and it increased linearly along the x axis (Fig. 7.5). Showing that, the applied electrical current density J in the BZ medium was homogeneous.

7.3 Evaluation of scroll rings

We now consider an example of a scroll ring as observed from two perpendicular projections, the top and lateral views, shown in Figure 7.6. The scroll ring was subjected to an electrical current density of $J = 40$ mA·cm^{-2}. The direction of the applied current pointed to the right of the figure. The filament initially lied in a horizontal plane and its unit vector **S** pointed downwards forming a right angle with
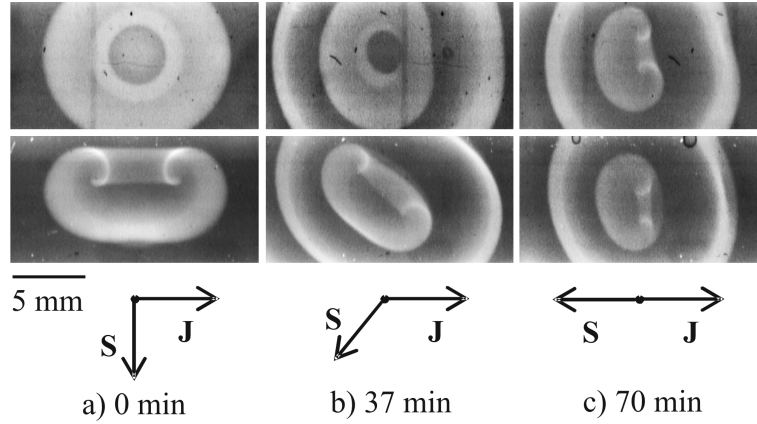
Figure 7.6: Projections of a scroll ring in the BZ reaction under an applied electrical currrent. Top row: top projection, bottom row: lateral projection. The applied current density $J = 40$ mA·cm^{-2} pointed to the right. (a) At the beginning, the unit vector **S** was perpendicular to **J**. The projections of the scroll ring appeared as circles (top view) and two counter-rotating spirals (lateral view). (b) The applied current caused a continuous reorientation of the scroll ring, until (c) **S** was anti-parallel to **J**. The dimensions of the images are 17×8.8 mm^2.

the current density vector **J** [Fig. 7.6(a)]. Hence, the initial scroll ring appeared as circular wave fronts and two counter-rotating spirals in the top and lateral projections, respectively. Due to the effect of the applied current, the filament plane rotated [Fig. 7.6(b) and (c)]. During the reorientation, the shape of wave front near the filament of the scroll ring in the top projection changed from a circle to an ellipse [Fig. 7.6(b)] and finally to two counter-rotating spirals [Fig. 7.6(c)] while the scroll ring in the lateral view appeared as two counter-rotating spirals for the whole experiment. Therefore, the lateral projection was used for evaluation purposes.

To evaluate the dynamics of scroll rings, we determinded the cores of two counter-rotating spirals in the lateral projection by a superposition of an image series taken during one rotation period, which was approximately constant at 200 s, using Eq. (5.2) in section 5.5. The cores are the dark areas never visited by the spiral waves. Figure. 7.7(a), which is a superposition of 7 images of the projection, shows a pair of counter-rotating spiral waves rotating around the cores. The wave fronts disappeared when 40 images were superposed leaving only the cores as shown in Fig. 7.7(b). Unlike 2D experiments [42], the brightness of spiral waves (Fig. 7.6)
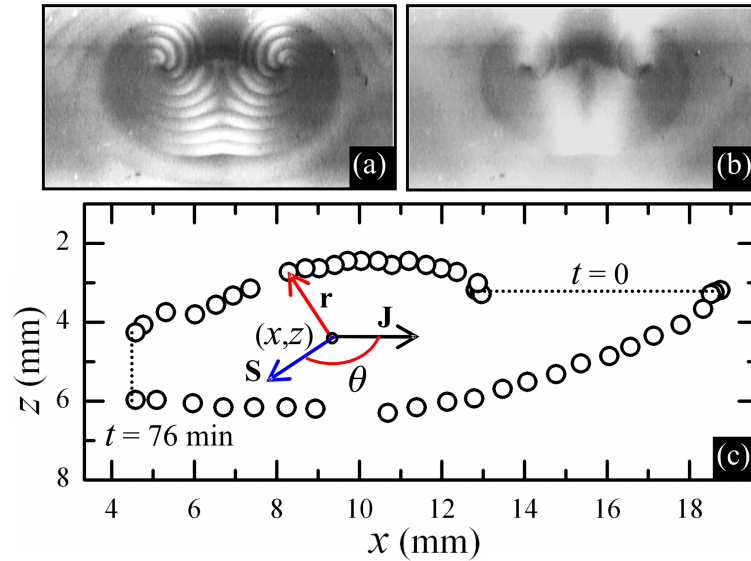
Figure 7.7: Evaluation of the scroll ring dynamics in a BZ medium. (a) and (b) are superpositions of 7 and 40 images of the lateral projection of a scroll ring, respectively. Two small dark regions are the cores around which a pair of spiral waves rotates. (c) The scroll ring was subjected to an applied electrical current density $J = 40$ mA·cm^{-2}. Circles show the positions of the core centers of two counter-rotating spirals in the lateral projection at $t = 0$–76 min. The radius r (i.e., $r = |\mathbf{r}|$) and the center (x, z) of the scroll ring were estimated as half of the distance and the center of mass of a pair of core centers, respectively. The unit vector $\mathbf{S}$ is perpendicular to $\mathbf{r}$ (and accounts for the direction of spiral rotation). The orientation θ is the angle between $\mathbf{S}$ and $\mathbf{J}$.

and of their superpositions [Fig. 7.7(a) and (b)] in the projection of a scroll ring is inhomogeneous. Therefore, the edge of the cores are difficult to be defined exactly.

To simplify the evaluation, the core centers of the two counter-rotating spiral waves were estimated by eye and the straight line connecting them was taken as the diameter of the scroll ring filament as shown in Fig. 7.7(c). This allows the determination of the radius r (i.e., $r = |\mathbf{r}|$), and the center (x, z) of the scroll ring. The unit vector $\mathbf{S}$ is perpendicular to the radius $\mathbf{r}$ (and accounts for the direction of spiral rotation) and finally the orientation θ can be measured.

7.4 Kinematic description

We performed numerical calculations to test whether the reorientation of scroll rings in the experiments follows the theory of local filament dynamics subjected

to the influence of parameter gradients [103, 111] (presented in section 4.4.3). The kinematic description [Eqs. (4.15)–(4.18)] was derived from the assumption that the applied gradient caused a gradient-induced velocity with two components [Eq. (4.14)]. As shown in section 3.3.1, an applied electrical current forces a spiral to drift with a 2-component velocity, however, in a transverse direction to the induced velocity defined in Eq. (4.14). A spiral wave in the xz plane, subjected to a current density J pointing in the x direction, would be forced to drift with a velocity defined as

$$
\begin{aligned}
\mathbf{v} &= -\beta J \mathbf{T} \times \mathbf{X} - \gamma J \mathbf{X} \\
&\equiv \mathbf{v}_z + \mathbf{v}_x,
\end{aligned}
\tag{7.1}
$$

Where $\mathbf{T}$ is the unit vector of the anglular velocity of the spiral wave and $\mathbf{X}$ is a unit vector pointing in the x direction. β and γ are constants and can be calculated as

$$
\beta = \frac{v_z}{J} \quad , \quad \gamma = \frac{v_x}{J}
\tag{7.2}
$$

where $v_z = |\mathbf{v}_z|$ and $v_x = |\mathbf{v}_x|$.

We adjust Eqs. (4.15)–(4.18) in section 4.4.3 to account for our experiments by replacing the gradient g with $-J$ and alternating x and z since the current density $\mathbf{J}$ was applied in the x direction. The dynamical variables of a scroll ring, i.e., the radius r, angle θ, and position (x, z), are influenced by the applied current density J as

$$
\frac{dr}{dt} = -\frac{\alpha}{r} - \beta J \cos\theta
\tag{7.3}
$$

$$
\frac{d\theta}{dt} = \frac{\beta J}{r} \sin\theta
\tag{7.4}
$$

$$
\frac{dz}{dt} = -\frac{\mu}{r} \sin\theta
\tag{7.5}
$$

$$
\frac{dx}{dt} = \frac{\mu}{r} \cos\theta - \gamma J
\tag{7.6}
$$

The coefficients α and μ describe the intrinsic dynamics of the scroll ring and were determined in the absence of any applied electric field while the coefficients β and

γ can be calculated from the drift [Eq. (7.2)] of a spiral wave or a straight scroll wave subjected to an electrical current as described in the next section.

Numerical integrations have been done using a fourth-order Runge-Kutta algorithm. For $dx/dt = f(x)$, the integrated solution at step $n+1$ is given by

$$x_{n+1} = x_n + \frac{1}{6} \left(k_1 + 2k_2 + 2k_3 + k_4 \right) \Delta t \tag{7.7}$$

where x_n is the solution at step n, $k_1 = f(x_n)$, $k_2 = f(x_n + \frac{1}{2}k_1)$, $k_3 = f(x_n + \frac{1}{2}k_2)$ and $k_4 = f(x_n + k_3)$. $\Delta t = 0.01$ min was used as time step for the integration.

7.5 Straight scroll waves in an applied current

The influence of the electrical current on scroll waves with a straight filament was also studied to determine the coefficients β and γ required for the kinematic description of scoll rings [Eqs. (7.3) – (7.6)].

We used the same reactor and setup as in the experiments on scroll rings. A scroll wave with a straight filament lying in a horizontal plane and perpendicular to the current density **J** was initiated using the two-layer strategy. A vertical planar wave front was ignited using Ag wire in the first layer. When the second layer was placed on the top of the first layer, the free edge of the planar wave front at the interface curled in to form a straight scroll wave. In the lateral projection, the scroll wave with a horizontal filement appeared as a spiral wave. As in 2D experiments [73, 71, 74, 70], the scroll waves drifted linearly to the anode (+) with an angle to the electrical current. Therefore, we simply measured the displacement $(\Delta x, \Delta z)$ of the spiral tip (in the lateral projection) for the whole experiments and the two components of the drift velocities v_x and v_z were calculated as $v_x = \Delta x/\Delta t$ and $v_z = \Delta z/\Delta t$. The coefficient β and γ were calculated using Eq. (7.2).

7.6   Simulations

The effects of the applied electrical current were reproducible in 3D numerical simulations using the Oregonator model with an additional advective migration term. As discussed in section 3.3.1, both reduced two- and three-component versions of the model including the advection can reproduce the experimenal results of the electrical field effect on the dynamics of spiral waves in two dimensions.

In our numerical simulations, we used the two-variable Oregonator model with advection terms of both u and v accounting for the electric field E (field strength $E = |\mathbf{E}|$) which was applied in the x direction:

$$
\begin{aligned}
\frac{\partial u}{\partial t} &= \frac{1}{\epsilon}\left(u - u^2 - fv\frac{u - q}{u + q}\right) + D_u\nabla^2 u - M_u E\frac{\partial u}{\partial x}, \\
\frac{\partial v}{\partial t} &= u - v + D_v\nabla^2 v - M_v E\frac{\partial v}{\partial x}.
\end{aligned}
\tag{7.8}
$$

The parameters were chosen as in refs. [56, 70]: $q = 0.002$, $f = 1.4$, $\epsilon = 0.01$, the diffusion coefficients $D_u = 1$ and $D_v = 0.6$, and the ionic mobilities $M_u = -1.0$ and $M_v = 2.0$. In the absence of an electric field, the system exhibits rigidly rotating spirals and contracting scroll rings in 2D and 3D, respectively.

The simulations were performed using an explicit Euler method with a 19-point approximation of the 3D Laplacian [26] and a centered-space approximation of the gradient term. The grid space $\Delta x = 0.2$ and time step $\Delta t = 0.012$ as required for numerical stability $\Delta t \leq (3/8)\,(\Delta x)^2$ [26]. The dimensionless size of the system was $70 \times 40 \times 40$ (corresponding to $350 \times 200 \times 200$ grid points).

Scroll rings with different initial orientations θ_0 were initiated using a similar procedure as in the experimental part: First, a spherical wave front was created by a local perturbation ($u = 1$). When the sphere reached a desired size (radius $r \approx 4-8$), one hemisphere was erased by setting $u = 0$, creating an open edge of the remaining wavefront, which curled in to form a scroll ring. The initial orientation θ_0 depends on the angle of the open edge with respect to the x-axis, i.e., to the vector $\mathbf{E}$ as in the experiments (Fig. 7.1).

Isoconcentration surfaces at $u = 0.15$ have been calculated using the marching

cube algorithm [116, 117, 118]. The filament of the scroll ring was defined as the intersection line of surfaces $u = 0.15$ and $v = 0.0935$ which ensures that $\partial u / \partial t = 0$ on the filament [58]. The center of mass of the filament was taken as the position (x, y, z) of the scroll rings and the radius r was calculated as the average distance from the center to the points along the filament.

To determine the orientation θ with respect to the electric field $\mathbf{E}$, the 3D filament was projected into the xz plane. A horizontal circular filament at the beginning appeared as a straight line in the xz plane. However, the shape of filament deformed during the reorientation. Therefore, a linear regression of the projected filament was taken as the average alignment of the filament before the orientation θ (the angle between the vectors $\mathbf{S}$ and $\mathbf{E}$) was measured as in the experiments (Fig. 7.7).

Chapter 8

Results and Discussion

In this chapter, we present experimental results on the dynamics of scroll rings under an applied electrical current. We start the chapter with a description of the intrinsic dynamics of scroll rings in a BZ medium. Then we consider the influence of the electrical forcing on the orientaion and lifetime of scroll rings. The compliance of scroll ring reorientation with predictions from the kinematic theory of local filament dynamics has been tested. Finally, 3D numerical simulations using the Oregonator model to reproduce the experimental findings are presented.

8.1 Experimental results

8.1.1 Intrinsic dynamics of scroll rings

To study the intrinsic dynamics of scroll rings, we initiated scroll rings whose filament lied in a horizontal plane (see Fig. 7.6: 0 min) so that the scroll rings appeared as circular wave fronts and a pair of counter-rotating spiral waves in the top and lateral projections, respecitively. In the absence of external forcing, the BZ medium used in this study (recipe II of table 5.1) supported self-contracting scroll rings, so the radius of the scroll rings decreased with time [Fig. 8.1(a)]. During the contraction, the scroll rings translated along their symmetric axis, i.e., in the direction of their unit vector $\mathbf{S}$ [Fig. 8.1(b)]. Note that no reorientation occured in this case so the unit vector $\mathbf{S}$ pointed downwards all the time.
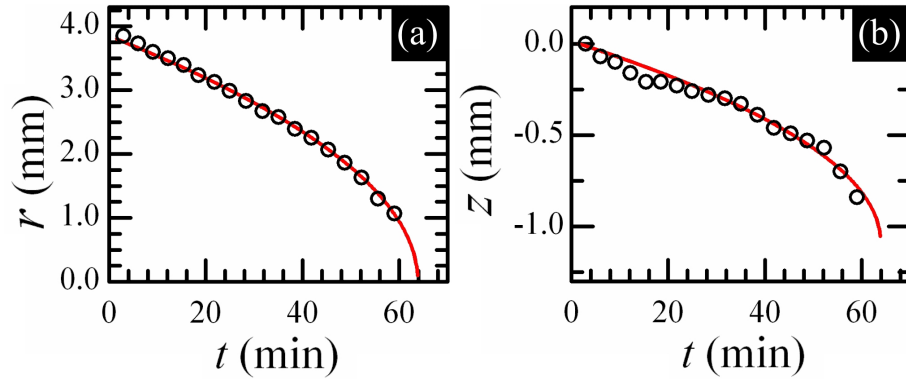
Figure 8.1: Intrinsic dynamics of scroll rings in a BZ medium. In the absence of any external field, the scroll ring contracted so (a) its radius r decreased with time. In parallel, (b) it also drifted along the unit vector **S** which pointed downwards all the times. Circles represent experimental data while curves are derived from numerical calculations of Eq.(8.1) using the fourth-order Runge-Kutta method [Eq. (7.7)] with $\alpha = 0.12$ mm^2 min^{-1}, $\mu = 0.033$ mm^2 min^{-1} and time step $\Delta t = 0.01$ min.

In the theory of local filament dynamics [122, 10, 123, 99] (see section 4.2), the rate of intrinsic contraction and the translational velocity of scroll rings with a uniform circular filament are inversely proportional to their radii, thus yielding the intrinsic dynamics of the radius (r) and the position (z):

$$\frac{dr}{dt} = -\frac{\alpha}{r} \quad , \quad \frac{dz}{dt} = \frac{\mu}{r} \tag{8.1}$$

which implies that

$$r(t) = \sqrt{r_0^2 - 2\alpha t} \quad , \quad z(t) = (z_0 + \frac{\mu}{\alpha}r_0) - \frac{\mu}{\alpha}r(t) \tag{8.2}$$

where α and μ are the intrinsic contraction and the translational constants, respectively. In experiments to measure α and μ, the initial radius r_0 was about $3.0 - 3.8$ mm and the intitial position z_0 was set to zero. Using Eq. (8.2), linear regressions of experimental data yielded $\alpha = 0.12 \pm 0.01$ mm^2 min^{-1} and $\mu = 0.033 \pm 0.003$ mm^2 min^{-1}.
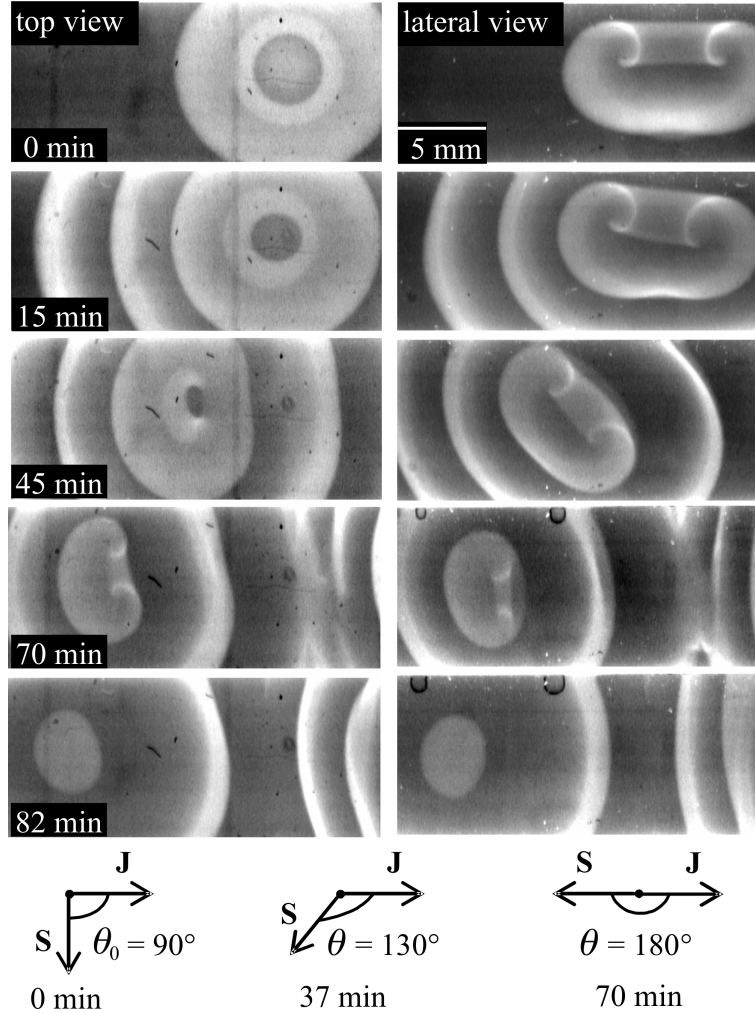
Figure 8.2: Dynamics of a scroll ring in a BZ medium under an applied electrical current. Left column: top projection, right column: lateral projection. The applied current density $\mathbf{J}$ ($J = |\mathbf{J}| = 40$ mA cm^{-2}) pointed to the right. At the beginning (0 min), the unit vector $\mathbf{S}$ was perpendicular to $\mathbf{J}$ ($\theta_0 = 90°$). The projections of the scroll ring appeared as circles (top view) and two counter-rotating spirals (lateral view). The applied current caused a continuous reorientation of the scroll ring leading to an increase in θ from 90° to 180° (0 – 70 min). The pattern in the top projection changed from a circle to an ellipse and to a pair of counter-rotating spirals, respectively, while the lateral view showed two counter-rotatings spiral waves. However, the shape of the two spirals (in the lateral view) deformed due to the reorientation. In the field, the scroll ring drifted to the anode (+), i.e., to the left. Due to the intrinsic contraction, the scroll ring became smaller and subsequently self-annihilated. Finally, spherical waves (82 min) were emitted periodically from the location where the self-annihilation occurred.

8.1.2 Scroll rings under electrical forcing

In this section, we present experiments on the dynamics of scroll rings in a BZ medium under the influence of an applied electrical current. Under these conditions, the scroll rings are subjected to two simultaneous processes, namely an intrinsic contraction and a possible reorientation with respect to the direction of the applied current. Due to the intrinsic contraction, scroll rings may self-annihilate before they reach a stationary alignment. To investigate the dynamics for the entire range of orientations, experiments with various initial orientations were conducted such that the intervals of the initial and final orientations from different experiments overlaped. In most of the experiments the applied current density was kept constant $J = 40$ mA cm^{-2}.

Effect of an applied electrical current

Figure 8.2 shows an example of scroll rings subjected to electrical current of density $J = 40$ mA cm^{-2} as observed from two perpendicular projections, the top and lateral views. The filament initially aligned in a horizontal plane (Fig. 8.2: 0 min) and its unit vector **S** pointed downwards forming a right angle ($\theta_0 = 90°$) with the current density vector **J** which pointed to the right of the figure. Hence, the scroll ring appears as circular wave fronts and two counter rotating spirals in the top and lateral projections, respectively. Due to the applied current, the filament plane turned clockwise about 90° over the whole experiment. (Fig. 8.2: 15 – 70 min). The reorientation was accompanied by a linear drift towards the anode (+) (to the left of the figure) with a rate of 0.17 mm min^{-1}, and a slight downward drift (rate = 0.03 mm min^{-1}). At the end of the experiment, **S** was anti-parallel to **J** (Fig. 8.2: 70 min) before the scroll ring disappeared due to contraction and subsequent self-annihilation.

A deformation of the uniform scroll ring due to the reorientation can be observed from the lateral projection. During the whole experiment, the scroll ring appeared as a pair of spirals in this lateral projection, however, the shape of spirals became asymmetrical. Such a behavior has been observed earlier in experiments
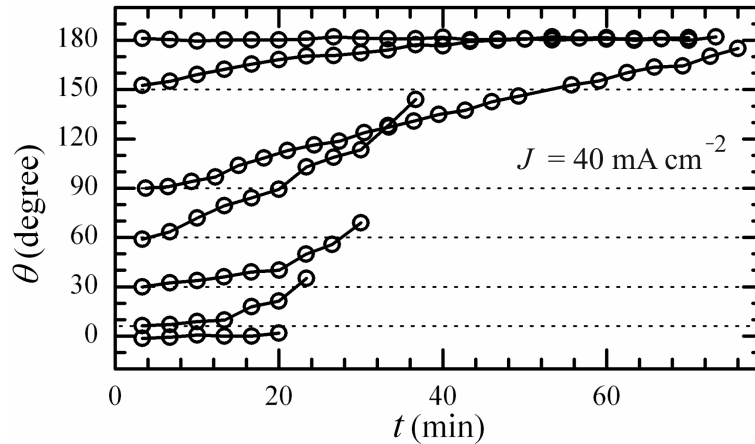
Figure 8.3: Orientation of scroll rings in a BZ medium under an electrical current. The scroll rings were initiated with different initial orientations $\theta_0 = 0°$, 6°, 30°, 60°, 90°, 150°, and 180° while a constant electrical current density of $J = 40$ mA cm^{-2} was applied during the entire experiments. Except for the experiments starting with $\theta_0 = 0°$ and 180°, the external field caused a scroll ring reorientation and the angle always increased towards 180°. During the experiments, the scroll rings contracted and eventually self-annihilated.

using a thin layer of the BZ reaction [71]. Similarly to a self-annihilated spiral pair that is found to create circular waves in 2D experiments [75], the location where the scroll ring self-annihilated acted as a pacemaker emitting spherical wave fronts periodically (Fig. 8.2: 82 min). This was also observed in the experiments without electrical current (section 8.1.2). Thus, the phenomenon occured regardless of the electrical forcing.

Note that the shape of the wave front near the filament of the scroll ring in the top projection changed from a circle to an ellipse and finally to two counter-rotating spirals while the scroll ring in the lateral view appeared as two counter-rotating spirals for the whole experiment. Therefore, the lateral projection was used for evaluation purposes.

Dynamics in dependence of initial orientation θ_0

To study the influence of the electrical current on the scroll rings at other orientations, experiments were performed using different initial angles θ_0. The initial radii r_0 of the scroll rings were about 2.6 – 3.3 mm. Figure 8.3 shows the scroll ring orientation in the experiments with initial angles $\theta_0 = 0°$, 6°, 30°, 60°, 90°,
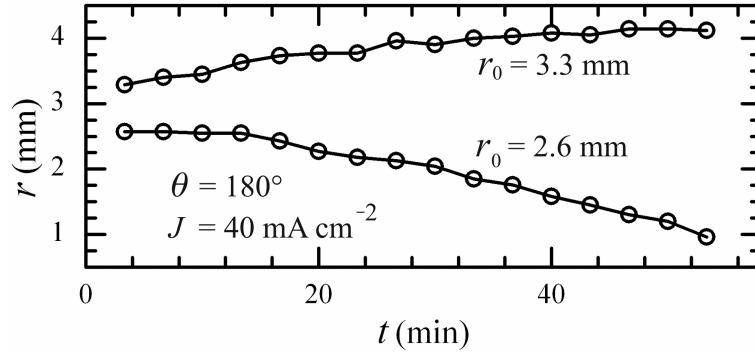
Figure 8.4: Mean radius of scroll rings in the BZ reaction under an applied electrical current. The orientation of the scroll rings was constant at $\theta = 180°$. In the presence of an electrical current density of $J = 40$ mA cm^{-2}, a scroll ring with an initial radius $r_0 = 3.3$ mm expanded while a smaller ring ($r_0 = 2.6$ mm) contracted.

150°, and 180°. In many of these experiments, the scroll rings contracted and self-annihilated while the reorientation was still in progress. By varying θ_0, we have investigated the dynamics of the scroll rings in overlapping ranges of orientation ($6° - 35°$, $30° - 70°$, $60° - 144°$, $90° - 180°$, and $150° - 180°$). For $6° \leq \theta < 180°$, the scroll rings were found to change their orientation. In fact, θ increased towards 180°. When $\theta = 0°$ or $\theta = 180°$, the orientation of the scroll rings remained unchanged. These results indicate that both parallel and anti-parallel orientations ($\theta = 0°$ and 180°) are stationary states. As every angle $\theta \geq 6°$ leads to an increase of θ towards 180°, the anti-parallel orientation of the scroll ring unit vector **S** with respect to the current **J** is a stable solution of the system. By contrast, the parallel orientation is also a stationary solution, however, it represents an unstable stationary state, since small derivations will induce a reorientation of the scroll ring.

Dynamics in dependence of initial radius r_0

In the following, we investigated the dynamics of scroll rings in dependence of their initial radii. To eliminate any effects of the reorientation, the experiments were performed at the stable fixed angle $\theta = 180°$. The initial radius r_0 of the scroll ring was varied while θ and J were kept constant (Fig. 8.4). At $J = 40$ mA cm^{-2}, a small scroll ring with $r_0 = 2.6$ mm still contracted, however, it lasted for a longer time than that in the free running case (no forcing) for the same r_0 (see

table 8.1.2). By contrast, a larger scroll ring with $r_0 = 3.3$ mm expanded. This implies that there must exist an initial radius (2.6 mm $< r_0 <$ 3.3 mm) where the self-contraction of the scroll ring and the expanding effect of electrical forcing are balanced, leading to a persistent scroll ring which neither contracts nor expands – i.e., its radius is invariant.

Lifetime of scroll rings in the electic field

The lifetime of scroll rings was also affected by the electrical current. It can be prolonged or shortened depending on the alignment of the scroll rings in the field [see Eq. (7.3)]. In the absence of external forcing, the lifetime of scroll rings depends only on the initial radius r_0. In theory, it can be calculated from Eq. (8.2) as lifetime $t = r_0^2/(2\alpha)$. Table 8.1.2 shows comparisions of the lifetime of scroll rings for the case of an applied current ($J = 40$ mA cm^{-2}) and for the free-running system ($J = 0$ mA cm^{-2}). In the experiments using $J = 40$ mA cm^{-2}, the initial alignments θ_0 were varied (Fig. 8.3). The initial radius r_0 of the scroll rings were also different ($r_0 = 2.6 - 3.3$ mm) due to a limitations in the scroll ring initiation procedure, as discussed in section 7.1. Therefore, the comparisions of both cases ($J = 40$ mA cm^{-2} and $J = 0$ mA cm^{-2}) have been done for the same initial radius r_0. The contraction of scroll rings, which always occurs in the absence of external forcing, was accelerated by the electrical current when $\theta_0 < 90°$. On the other hand, the lifetime of scroll rings was prolonged when $\theta_0 \geq 90°$ [see Eq. (7.3)]. Here the scroll rings contracted much slower and, for a sufficiently large initial radius, scroll ring expansion could be observed (Fig. 8.4: $r_0 = 3.3$ mm).

Manipulation of a scroll ring

At the end of this section, we show that the scroll rings may be controlled efficiently in their size by using the electrical current. This relies on the fact that the strength and direction of the applied current can be changed within a short time. Figure 8.5 shows the evolution of a scroll ring under a stepwise variation of the electrical current at an anti-parallel orientation ($\theta = 180°$). The plots show the positions of the scroll ring (i.e., the core centers of counter-rotating spiral pair

Table 8.1: Influence of electrical forcing on the lifetime of scroll rings in a BZ medium. The lifetime of scroll rings are compared for the case of an applied electrical current density $J = 40$ mA cm^{-2} and for the free-running system ($J = 0$ mA cm^{-2}). For the experiments with $J = 40$ mA cm^{-2}, the initial radius r_0 of the scroll rings was about $2.6 - 3.3$ mm. The lifetime in the case of $J = 0$ mA cm^{-2} was calculated from the curve in Fig. 8.1(a). [1]The scroll ring expanded.

θ_0	r_0 (mm)	lifetime (min)	
		$J = 40$ mA cm^{-2}	$J = 0$ mA cm^{-2}
0°	2.8	23.3	33.8
6°	3.1	27.1	41.4
30°	3.3	33.2	46.9
60°	3.3	40.0	46.9
90°	3.0	79.3	38.8
150°	2.8	76.7	33.8
180°	2.6	56.0	29.5
180°	3.3	> 54.0[1]	46.9
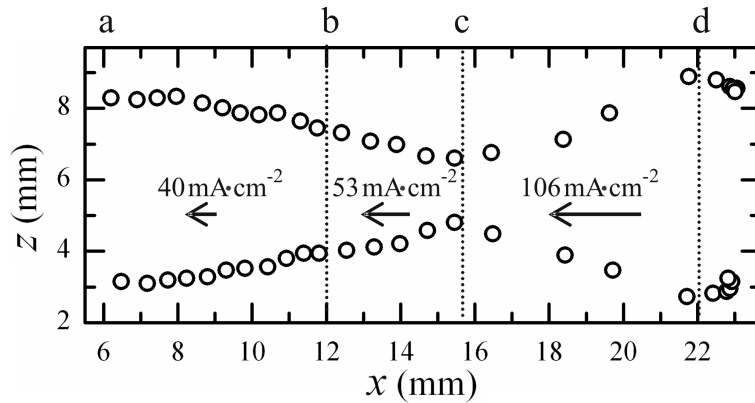
Figure 8.5: Manipulation of a scroll ring by a stepwise variation of the electrical current. Circles show the position of core centers of two counter-rotating spirals in the lateral projection at 200 s intervals. The current density **J** was anti-parallel to the unit vector **S** of the scroll ring (**J** pointed to the left), causing the scroll ring to drift to the right without reorientation. For $0 < t < 37$ min: (a) to (b), J was kept constant at 40 mA cm^{-2} and the scroll ring drifted to the right with decreasing radius. At $t = 37$ min: (b), J was increased to 53 mA cm^{-2}, however, the radius of scroll ring still contracted. Shortly before self-annihilatition occurred, J was increased to 106 mA cm^{-2} at $t = 54$ min: (c). Under this strong applied field, the scroll ring expanded. At $t = 67$ min: (d) the external field was switched off and the scroll ring contracted again at an approximately fixed position.

at 200 s intervals) which drifted to the right of the figure while $\mathbf{J}$ pointed to the left. Starting with $J = 40$ mA cm^{-2} [at (a) in Fig. 8.5], the scroll ring contracted slowly. At $t = 37$ min [at (b) in Fig. 8.5], J was increased to 53 mA cm^{-2} and the ring radius still decreased. When the radius was ≈ 1 mm [at (c) in Fig. 8.5], J was increased drastically to 106 mA cm^{-2}. This strong forcing led to an expansion of the scroll ring. Note that under a weaker field, e.g., $J = 40$ mA cm^{-2}, the scroll ring with $r \approx 1$ mm would self-annihilate in a short time (after about one period). Finally, the current was switched off ($J = 0$ mA cm^{-2}) at $t = 67$ min [at (d) in Fig. 8.5], thus causing the scroll ring to shrink again.

8.1.3 Straight scroll waves under electrical forcing

The dynamics of straight scroll waves in an applied electrical current have been studied to determine the coefficients β and γ which are introduced by the current in the kinematic description of scroll ring dynamics in an applied electrical current, Eqs. (7.3) – (7.6). We created scroll waves with a straight filament lying along the y axis, i.e., in a horizontal plane and perpendicular to the applied current density $\mathbf{J}$ which was in the x direction. The scroll waves simply drifted linearly to the anode ($+$) with an angle to the electric current, as it is also the case for spiral waves [73, 71, 75, 74, 70], and the straight filament remained perpendicular to the applied current all the times. The drift velocity was composed of two components, the anti-parallel velocity ($\mathbf{v}_x$) and the perpendicular velocity ($\mathbf{v}_z$), with respect to the applied current.

Under the current density $J = 40$ mA cm^{-2}, the scroll waves drifted along an inclined path to the anode ($+$) with $|\mathbf{v}_x| = v_x = 0.14 \pm 0.01$ mm min^{-1} and $|\mathbf{v}_z| = v_z = 0.066 \pm 0.004$ mm min^{-1}. The coefficients β and γ were calculated from Eq. (7.2) as $\beta = v_z/J = 0.17 \pm 0.01$ mm^3 min^{-1} mA^{-1} and $\gamma = v_x/J = 0.35 \pm 0.02$ mm^3 min^{-1} mA^{-1}.
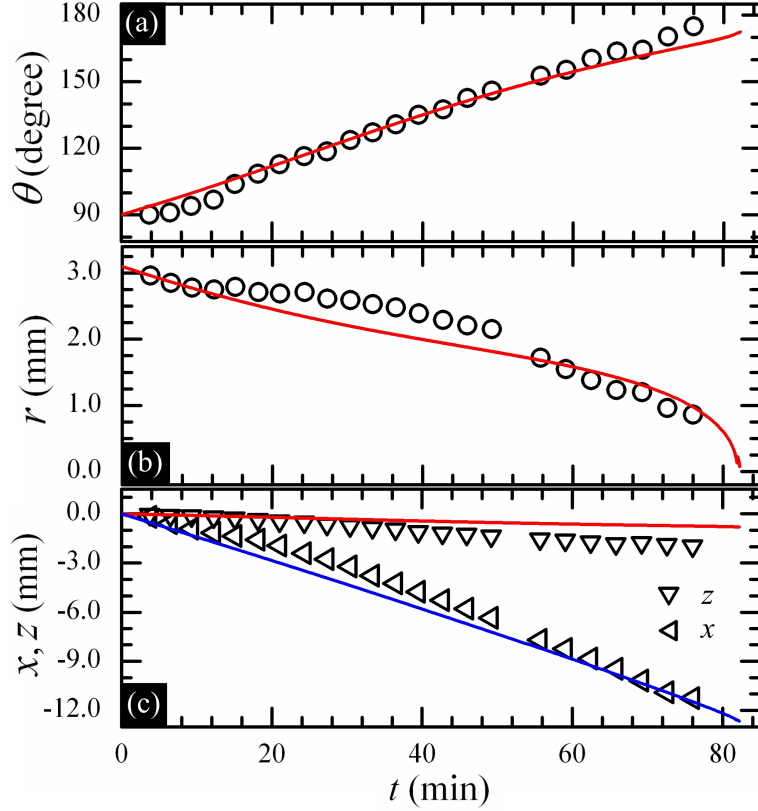
Figure 8.6: Comparision of the dynamics of a scroll ring in a BZ medium under electrical forcing with the calculations of the kinematic description. Data points represent experimental results. Under $J = 40$ mA cm^{-2}, the scroll ring in the BZ medium reoriented and contracted so that (a) the angle θ increased from 90° to 180° and (b) the radius r decreased. (c) The scroll ring also drifted mainly to the anode $(+)$ (x) and slightly downwards (z). Solid lines show numerical calculations of the theory of local filament dynamics under parameter gradients, Eqs. (7.3) – (7.6). Parameters: $\alpha = 0.12$ mm^2 min^{-1}, $\mu = 0.033$ mm^2 min^{-1}, $\beta = 0.17$ mm^3 min^{-1} mA^{-1}, $\gamma = 0.35$ mm^3 min^{-1} mA^{-1}, and $J = 32$ mA cm^{-2}. Initial values of the variables: $r_0 = 3.1$ mm, $\theta_0 = 90°$, $x = z = 0$ mm.

8.2   Kinematic description

Now we consider the compliance of the dynamics of a scroll ring under electrical forcing with the local filament theory modified for parameter gradients [111]. When a scroll ring is subjected to an applied current density J, the dynamical variables of the scroll ring, the radius r, the angle θ, and the position (x, z), are influenced as predicted by Eqs. (7.3) – (7.6) presented in section 7.4.

Figure 8.6 shows comparisions of the experimental results (data points) in the case of $\theta_0 = 90°$ (see Fig. 8.2) and numerical results (solid lines) from the theory Eqs. (7.3) – (7.6). Numerical calculations have been performed using the coefficients accounting for the intrinsic dynamics: $\alpha = 0.12$ mm^2 min^{-1} and $\mu = 0.033$ mm^2 min^{-1} (obtained in section 8.1.2). This yields the coefficients introduced by the electrical current as $\beta = 0.17$ mm^3 min^{-1} mA^{-1} and $\gamma = 0.35$ mm^3 min^{-1} mA^{-1} (see section 8.1.3). The initial values of the variables were set as $r_0 = 3.1$ mm, $\theta_0 = 90°$, $x = z = 0$ mm. The calculations with $J = 32$ mA cm^{-2} were in good agreement with the experimental data.

8.3   Simulation results

To reproduce the dynamics of scroll rings under an electrical forcing found in the experiments, numerical simulations have been performed using the two-variable Oregonator model with an advective term accounting for an applied electric field [Eq. (7.8)]. As in the experiments, the electric field $\mathbf{E}$ was kept constant in the x direction with a field strength $E = |\mathbf{E}| = 0.34$.

Figure 8.7 shows the dynamics of a scroll ring in the simulations using $E = 0.34$ ($\mathbf{E}$ pointed in the x direction, to the right) and the initial angle $\theta_0 = 90°$. For illustration propose, the isoconcentration surfaces of the scroll ring were depicted in colors which depended on the 3D position (x, y, z) while the filament was shown in black. To reveal the inner wave fronts and the filament, the surfaces at $y < 20$ were cut off. As found in the experiments, the scroll ring reoriented, contracted, drifted linearly anti-parallel to the electric filed (rate $= 0.53$) and downwards (rate
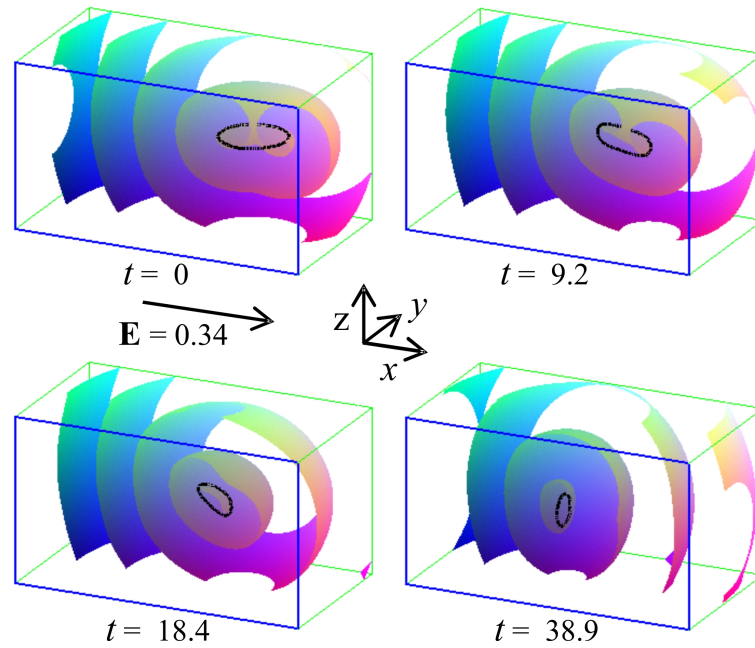
Figure 8.7: Dynamics of a scroll ring in the Oregonator model under an applied electric field. The isoconcentration surfaces are illustrated in position-dependent colors and the filaments are in black. The surface at $y < 20$ was cut off to show the inner wave fronts and the filament. Under $E = 0.34$ (**E** pointed in the x direction), the scroll ring reoriented so the filament plane turned clockwise from horizontal to vertical. The scroll ring also contracted and drifted anti-parallel to **E** and downwards.
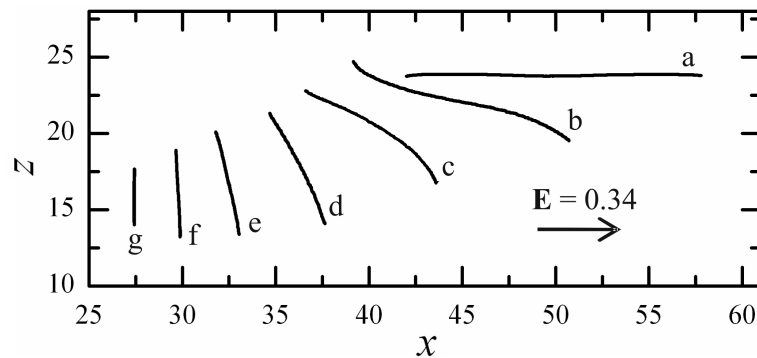
Figure 8.8: The xz projection of scroll ring filaments in the Oregonator model under an applied electric field $E = 0.34$ at $t = 0$, 9.2, 18.4, 27.6, 32.9, 38.9, and 42.3 (a-g). Their shape and orientation changed with time. During the reorientation, the pattern of filament projection changed from an almost straight (a) to wavy (b), and curved line (c, d). Towards the end of the simulations (e-g), the projection pattern returned to a straight line before the scroll ring self-annihilated.

$= 0.21$), and eventually self-annihilated. The scroll ring wave front and the filament were also seen to deform during the reorientation. After the scroll ring disappeared, spherical wave fronts were periodically emitted from the final location of the scroll ring.

To simplify the interpretation, the filament was projected on the xz plane, as shown in Fig. 8.8 so that a circular filament lying in a horizontal plane appeared as a straight line (a) in this projection. During the reorientation, the filament plane deformed from a flat (a) to a wavy (b) and a curved (c, d) plane. Later, the curved plane straightened to a flat plane again (e-g). The xz projection of the closed-loop filament has a straight or a curved line shape implying that the reorientation and the modulation of the filament plane never occurred in the y direction, i.e., the axis of reorientation.

The scroll ring reorientation (under $E = 0.34$) for simulations starting with $\theta_0 = 0°$, $6°$, $20°$, $40°$, $90°$, and $180°$ is shown in Fig. 8.9(a). Except for $\theta_0 = 0°$ and $180°$, the angle θ increased as also found in the experiments (Fig. 8.3). Furthermore, the scroll rings contracted and self-annihilated so that the reorientation can be studied in a limited range of angles for a specific value of θ_0. An advantage of the simulations is that a small initial angle θ_0 can be set precisely. As shown in Fig. 8.9(b), the simulations were performed with θ_0 as small as $1°$ and $2°$ and θ still increased in both cases. The reorientation of scroll rings in the entire interval of angles between $1°$ and $180°$ has been determined in overlapping subset ranges ($1°-4°$, $2°-7°$, $6°-23°$, $20°-52°$, $40°-93°$, and $90°-180°$). The simulations show that the angle θ increased towards $180°$ if $\theta_0 \geq 1°$, thus reproducing the existence of two stationary orientations at $\theta = 0°$ and $\theta = 180°$. As in the experiments, the parallel orientation ($\theta = 0°$) is an unstable stationary state while the parallel alignment ($\theta = 180°$) is stable.

A persistent scroll ring in an advective field could be realized in our simulations. Figure 8.10 shows the instantaneous radii of scroll rings in the simulations starting with different initial radii r_0 while $\theta = 180°$ and $\mathbf{E}$ was kept constant. Note that the plotted radii oscillate around local extrema since the instantaneous filament rotated around a small tube composed of 2D spiral cores. At $E = 0.34$, small scroll
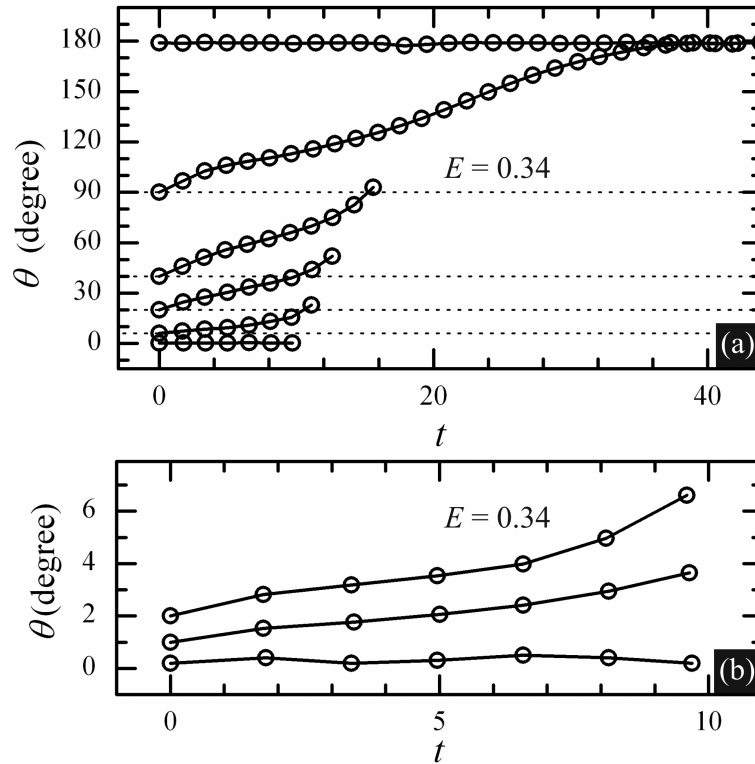
Figure 8.9: Orientation of scroll rings in the Oregonator model under an advective field. The scroll rings were initiated with different initial orientations (a) $\theta_0 = 0°$, $6°$, $20°$, $40°$, $90°$, and $180°$; and (b) $\theta_0 = 0°$, $1°$, and $2°$. A constant electric field ($E = 0.34$) was applied during the simulations. Except for the simulations starting with $\theta_0 = 0°$ and $180°$, the external field caused scroll ring reorientation. For $\theta \neq 0°$, the angle always increases towards $180°$. During the simulations, the scroll rings contracted and eventually self-annihilated.
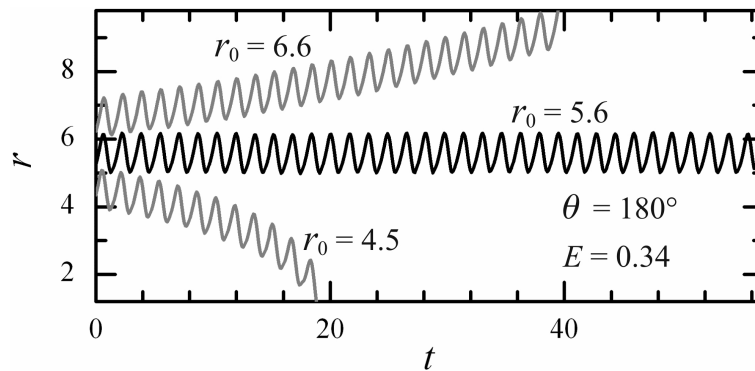
Figure 8.10: Radius of scroll rings in the Oregonator model under an advective field. A constant electric field $E = 0.34$ was applied anti-parallel to the unit vector of the scroll rings ($\theta = 180°$). Depending on their initial mean radius r_0, large scroll rings expanded ($r_0 = 6.6$) while small ones contracted ($r_0 = 4.5$). Furthermore, a balance of self-contraction of the scroll ring and the effect of the electric field led to a persistent scroll ring ($r_0 = 5.6$) whose mean radius was constant. The curves show the instantaneous radii of the scroll rings.
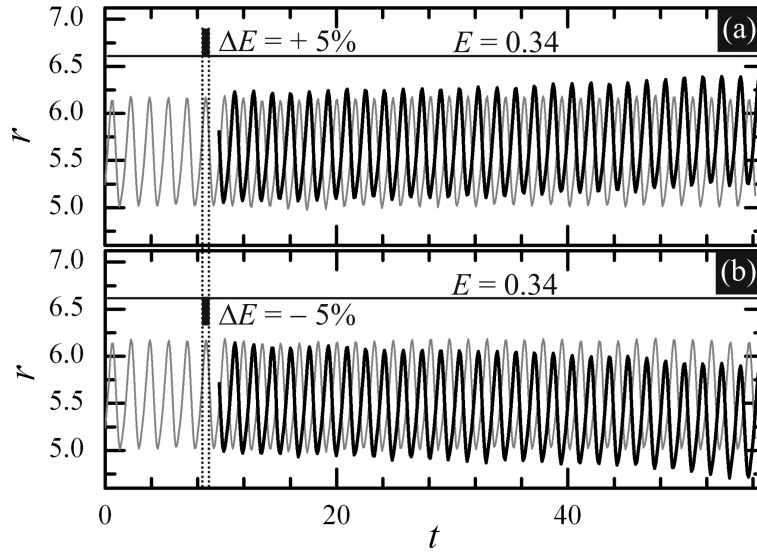
Figure 8.11: Perturbation of a persistent scroll ring in the Oregonator model under an advective field. When small perturbations with (a) $\Delta E = +5\%$ and (b) $\Delta E = -5\%$ were applied for a half of the wave period (black marks at $t \approx 8$), the scroll ring gradually expanded and contracted, respectively. For a purpose of illustration, the plots of the radius (black curves) after the perturbations were artificially shifted for a half of the wave period along the time axis while the radius of the unperturbed traveling scroll ring is depicted as a gray curve.

rings ($r_0 = 4.5$) contracted while large scroll rings ($r_0 = 6.5$) expanded. For $r_0 = 5.6$, a persistent scroll ring travelled with a constant mean radius. However, the persistent scroll ring was unstable to a small perturbation of the electric field. As shown in Fig. 8.11, the radius of the scroll ring gradually increased [Fig. 8.11(a)] or decreased [Fig. 8.11(b)] when a small perturbation of the field strength, $\Delta E = \pm 5\%$, was applied within a half period of rotation. This shows that presistent scroll rings in an applied electric field are intrinsically unstable.

The lifetime of scroll rings in the simulations, shown in table 8.3, was influenced by electrical forcing as found in the experiments (table 8.1.2). In the absence of any electrical field, scroll rings with an initial radius $r_0 = 8$ in our modeling system contracted and disappeared within $t = 23.3$. Under the electric field, the scroll rings last longer when the initial orientation $\theta_0 = 90°$ and $180°$. However, the lifetime of the scroll rings with $\theta_0 = 0°, 1°, 2°, 20°$, and $40°$ was shortened.

Table 8.2: Influence of electrical forcing on the lifetime of scroll rings in the Oregonator model. In the absence of electric field, a scroll ring with an initial radius $r_0 = 8$ contracted and self-annihilated within $t = 23.3$. Under a constant elecric field $E = 0.34$, the lifetime of scroll rings with the same initial size ($r_0 = 8$) was either shortened or prolonged depending on the initial orientation θ_0. [1]The scroll ring expanded.

θ_0	lifetime
$0°, 1°, 2°$	10.9
$6°$	11.4
$20°$	13.0
$40°$	16.1
$90°$	44.2
$180°$	> 45[1]

8.4   Summary

In summary, we have studied the influence of an applied direct electrical current on scroll rings in the BZ reaction. Unless the scroll rings were aligned parallel ($\theta = 0°$) or anti-parallel ($\theta = 180°$) to the applied current, they reoriented towards the anti-parallel orientation. It could be shown that the parallel orientation is an unstable stationary state while the anti-parallel alignment is a stable orientational stationary state.

Numerical calculations using the kinematic theory of the local filament dynamics under parameter gradients [103, 111], agreed well with the experimental results. Similar behavior has also been reported for a system subjected to temperature gradients, thus showing common influences of the electrical current and the gradient of temperature [103] on the dynamics of scroll ring in the BZ reaction.

The effect of the elecrical forcing on the lifetime of scroll rings depended on the orientation of the scroll rings. In comparision to the case of no forcing, the scroll rings with initial orientation $0° \leq \theta_0 < 90°$ had a shorter lifetime while the scroll rings with initial orientation $90° \leq \theta_0 \leq 180°$ stayed longer, in line with Eq. (7.3).

The dynamics of scroll ring radius was investigated at the stable orientation ($\theta = 180°$) in which the lifetime of the scroll rings was prolonged when an electrical

current was applied. Because the self-contraction rate is inversely proportional to the radius and the expanding effect is linear with respect to the applied current at $\theta = 180°$ as proposed in the theory of local filament dynamics in parameter gradients [$dr/dt = -\alpha/r + \beta J$, where α and β are constant, see Eq. (7.3)], an expansion of sufficiently large scroll rings was observed in the presence of electrical forcing.

Manipulation of scroll rings using electrical current was demonstrated in experiments. Unlike the case of temperature gradients, a desired current is applied precisely in a short time. As an example, the strength of an applied current density was increased substantially within a short time to cause a small contracting scroll ring, which otherwise would soon self-annihilate, to survive and expand.

The simulations using the Oregonator model with an advective field reproduced well all the aspects found in the experiments, namely the unstable and stable stationary orientations with respect to the applied field, as well as the shrinkage and growth of the scroll rings as a function of the initial radius in case of the stable stationary orientation. Furthermore, some situations which are difficult to realize in experiments were accomplished in the simulations. First, a scroll ring with an initial angle θ_0 as small as 1° can be initiated precisely in the simulations thus supporting the conclusion that the fixed orientation at $\theta = 0°$ is unstable towards perturbations. Second, a persistent scroll ring subjected to electrical forcing at the stable fixed orientation $\theta = 180°$ requires an exact balance of the intrinsic contraction and the electrical expansion. By keeping the electric field constant and performing a fine adjustment of the scroll ring radius, the balance condition was fulfilled in the simulations leading to a persistent scroll ring travelling in the reaction-diffusion-advection system.

Finally, it is worthwhile to note that we have tested for the homogeneity of the applied electrical current and the temperature gradient due to ohmic heating as shown in section 7.2.1. The current density J in the BZ medium was homogeneous. The ohmic heating was unavoidable in such a thick ionic medium. However, the temperature gradient was small ($0.5°C$ cm^{-1} at $J = 40$ mA cm^{-2}) in comparision to that ($10 - 20°C$ cm^{-1}) used to affect the dynamics of scroll rings [103].

Chapter 9

Conclusion and outlook

Spiral waves and scroll waves of excitation are common in a variety of excitable media. For a given value of the system parameters where spiral waves in two dimensions are stable, scroll waves in a three-dimensional (3D) medium are found to be unstable in various situations. Scroll waves and their instabilities are believed to be the source of some cardiac arrhythmias and fibrillation which potentially lead to a sudden cardiac death.

Three distinguishable instabilities of straight scroll waves in homogeneous media have been predicted in theory and simulations using different models for excitable media. The 3D meandering instability is a restabilization of a straight filament to a helix or a flat zig-zag shape found in simulations using periodic and no-flux boundary conditions, respectively. In the regime of the negative line tension instability, in which the excitability of the system is very low, a linear filament becomes snaking and its length increases in an unlimited manner. When a sufficiently high twist rate is imposed to a straight scroll wave, a twist-induced instability occurs and the straight filament deforms to a stable helix in simulations with periodic boundary conditions.

In Part I of this thesis, the existence of two kinds of scroll wave instabilities, the 3D meandering instability followed by the negative line tension instability, have been shown in experiments using a closed BZ reaction system. Optical tomographic observations were utilized to reconstruct 3D structures of scroll waves

and their filaments. We observed that an initial straight filament deformed to a flat zig-zag line with a roughly constant filament length which is an indication of the 3D meandering instability. Due to the ageing of the BZ reaction, the bending of the filament was more pronounced and the filament length expanded towards the end of the experiments, implying a negative line tension instability. Numerical simulations using the Barkley model, in which the ageing of the BZ reaction was mimicked by a decrease of the excitability, reproduced the qualitative behavior of scroll waves found in the experiments. To our knowledge, the described results represent the first experimental realization of these two types of scroll wave instabilities, corroborating the predictions from theorectical models.

In Part II, we have investigated the dynamics of scroll rings subjected to an applied electrical current in both experiments and simulations. In the absence of external forcing, in our experiments scroll rings contracted and subsequently self-annihilated at approximately the same alignment and location. Under an applied electrical current, a reorientation of the scroll rings occurred until their unit vector aligned antiparallel to the current (the angle between the unit vector of scroll rings and the current $\theta = 180°$) or until they self-annihilated. Therefore, the antiparallel orientation with respect to the applied current is a stable steady state. The other steady orientation is the parallel alignment ($\theta = 0°$), however, it is unstable since a small deviation from this alignment leads to a reorienton. The scroll rings were always found to drift mainly to the anode (+) irrespective to the reorientation. The effect of an applied electrical current on the lifetime of scroll rings depended on the initial alignment (θ_0) of the scroll rings. When $90° \leq \theta_0 \leq 180°$, the scroll rings lasted longer than those in the absence of external field. By contrast, the lifetime was shortened where $0° \leq \theta_0 < 90°$. For the stable steady orientation ($\theta = 180°$), small scroll rings still contracted, however, larger scroll rings expanded at a given strength of electrical current. This indicates the existence of a critical radius (at a fixed electrical current), where persistent scroll rings (i.e., scroll rings of constant radius) should exist. Furthermore, this critical radius r_c separates the domains of shrinking ($r < r_c$) and expanding ($r > r_c$) scroll rings. Our experimental results agreed well with numerical simulations using the Oregonator

model with an additional advective term accounting for an applied electric field. Furthermore, we observed a persistent scroll ring travelling with constant mean radius in the simulations where the electrical induced expansion balanced to the intrinsic contraction of the scroll ring.

In the present thesis, we have experimentally proven the existence of shrinking and expanding scroll rings, as well as their dependence of the applied electrical current. In order to obtain a more quantitative understanding of this phenomenon, we would like to suggest a more systematic study of the exact conditions required for obtaining persitent scroll rings under an electrical current. This requires a study of the scroll ring dynamics at the stable stationary orientation as a function of both the initial radius and the applied electrical current in both experiments and simulations. Such a study may yield a 2-parameter bifurcation diagram, where the location of the critical radius is well defined. Such a quantitative knowledge on the dynamics of scroll rings will open up possibilities for a controlled manipulations of these 3D structures.

Our study of electrical forcing on scroll rings has shown common features of the influence of an applied electrical current and that of temperature gradients and light intensity gradients reported in eariler experiments. In theory, the latter two gradients affect the reaction terms in the reaction-diffusion equations while the electrical current plays a role in an additional advective term, leaving the reaction terms untouched. The advective term represents a convenient target for manipulating scroll rings without affecting the reaction and diffusion parts. This flexibility can be readily exploited in implementations of more complex electrical currents (either in the form of the electrical current or in the geometrical orientation of the electrodes) and even feedback manipulations as typically used for control experiments. These types of manipulations can be easily realized in experiments and in calculations, thus providing the possibility of an elaborate manipulation and control of scroll rings.

Appendix A

Tomography

Tomography is a method for producing an image of an internal 3D structure of an object. By observing the object from many different angles, its image can be reconstructed from these projections. For image reconstruction of a scroll wave in the BZ reaction, we use optical tomography with a parallel-beam technique. With this method, 2D horizontal slices of the scroll wave are reconstructed separately and subsequently stacked into a 3D volume of data. Here, we briefly describe the concept of reconstruction of a single 2D horizontal slice. Details can be found in reference [124].

A.1   Radon transform

In 1917, the mathematician Johann Radon proposed that the cross-section function of an object can be reconstruted from measurments which are line integrals of the function. The function defined by a complete set of the line integrals, i.e., the measured projections, has been named the *Radon transform*.

Consider an object $f(x, y)$ in Fig. A.1(a). To measure its projections at different angles, a rotating coordinate system, uv, arises naturally in parallel-beam geometry. The uv-coordinate system is rotated by an angle θ [Fig. A.1(a)], thus

$$
\begin{aligned}
x &= u\cos\theta - v\sin\theta\ , \\
y &= u\sin\theta + vcos\theta.
\end{aligned} \tag{A.1}
$$
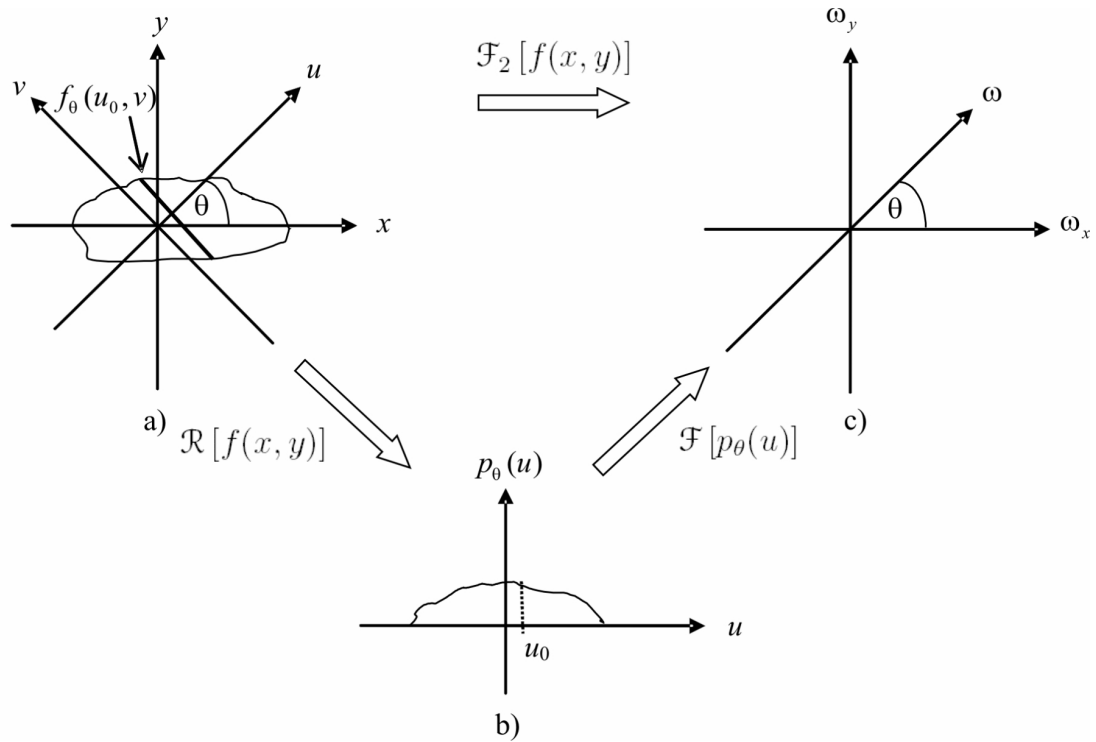
Figure A.1: The Radon transformation and its relation to the Fourier transformation. a) the domain of an observed object and its reconstructed image, (b) the domain of a projection observed at an angle θ, and (c) the Fourier domain.

A projection $p_\theta(u)$ (i.e., the measured data) of $f(x,y)$ is defined as a line integral passing through the object at an angle θ, i.e., the Radon transform, $\mathcal{R}\left[f(x,y)\right]$,

$$\mathcal{R}\left[f(x,y)\right] = p_\theta(u) = \int_{-\infty}^{\infty} f_\theta(u,v)\, dv \tag{A.2}$$

where $f_\theta(u,v)$ is a representation of the object with respect to the uv coordinates.

A.2 The projection slice theorem

An important relation between the Radon transform and the Fourier transform in tomography is known as the *projection slice theorem* which states that the 1D Fourier transform of the projection $p_\theta(\theta,u)$ is a slice of the 2D Fourier transform

of the object $f(x, y)$ [Fig. A.1(c)]. The 2D Fourier transform of $f(x, y)$ is

$$\mathcal{F}_2\left[f(x, y)\right] = F(\omega_x, \omega_y) = \int\limits_{-\infty}^{\infty} \int\limits_{-\infty}^{\infty} f(x, y) \exp\left[-j(\omega_x x + \omega_y y)\right] dx dy. \qquad (A.3)$$

By changing variables in Eq.(A.3), using Eq.(A.1) and the Jacobian determinant

$$dx dy = \begin{vmatrix} \frac{\partial x}{\partial u} & \frac{\partial y}{\partial u} \\ \frac{\partial x}{\partial v} & \frac{\partial y}{\partial v} \end{vmatrix} du dv \qquad (A.4)$$

then finding $F(\omega_x, \omega_y)$ at

$$\omega_x = \omega \cos\theta \quad \text{and} \quad \omega_y = \omega \sin\theta \qquad (A.5)$$

we will give the projection slice theorem as

$$F_\theta(\omega) = \int\limits_{-\infty}^{\infty} \int\limits_{-\infty}^{\infty} f(u, v) \, dv \, \exp\left[-j\omega u\right] du \qquad (A.6)$$

or

$$F_\theta(\omega) = \mathcal{F}\left[p_\theta(u)\right]. \qquad (A.7)$$

This means that the 1D Fourier transform of the projection at angle θ is the slice of the 2D Fourier transform of the object at the angle θ, as shown in Fig. A.1.

A.3   Fourier reconstruction technique

At this point, it is possible to reconstruct the image, $f(x, y)$, by using the 2D inverse Fourier transform,

$$\begin{aligned} f(x, y) &= \mathcal{F}_2^{-1}\left[F(\omega_x, \omega_y)\right] \\ &= \frac{1}{(2\pi)^2} \int\limits_{-\infty}^{\infty} \int\limits_{-\infty}^{\infty} F(\omega_x, \omega_y) \exp\left[j(\omega_x x + \omega_y y)\right] d\omega_x d\omega_y. \end{aligned} \qquad (A.8)$$

Rewriting Eq. (A.8) in terms of polar coordinates in both space and frequency domains, using Eqs. (A.4), (A.9), and (A.10),

$$x = r \cos \phi \ \ \text{and} \ \ y = r \sin \phi \tag{A.9}$$

$$\cos \theta \cos \phi + \sin \theta \sin \phi = \cos(\theta - \phi) \tag{A.10}$$

and then changing limit of the integral and using modified polar coordinates,

$$\int_{-\infty}^{\infty} \int_{-\infty}^{\infty} \ldots d\omega_x d\omega_y \ = \ \int_{0}^{2\pi} \int_{0}^{\infty} \ldots \omega \, d\omega d\theta \ = \ \int_{0}^{\pi} \int_{-\infty}^{\infty} \ldots |\omega| \, d\omega d\theta \tag{A.11}$$

yields

$$f(r, \phi) \ = \ \frac{1}{(2\pi)^2} \int_{0}^{\pi} \int_{-\infty}^{\infty} F(\omega, \theta) \exp \left[j\omega r \cos(\theta - \phi) \right] |\omega| \, d\omega d\theta \tag{A.12}$$

Equation (A.12) requires continuous projection data. However, in practice the projections are taken at discrete sampling points and therefore interpolation in the frequency domain is necessary. Using this technique, the image can be reconstructed by the following steps:

1. measure the projections, $p_\theta(u)$, from $\theta = 0$ to $\theta = \pi$;

2. perform the 1D Fourier transformation of the projections [using Eq. (A.7)] to get $F(\omega, \theta)$;

3. perform the 2D inverse Fourier transformation of $F(\omega, \theta)$ [using Eq. (A.12)] to get the image.

A.4 Convolution technique of reconstruction

By regrouping Eq. (A.12) and using the convolution property of the Fourier transform, the convolution version of image reconstruction can be obtained. This can eliminate the step of computing the 1D Fourier transform of the projections and the subsequent 2D inverse Fourier transform. Therefore, using this technique, there

is no need to interpolate in frequency domain. Equation (A.12) can be rewritten
as

$$f(r, \phi) \;\;=\;\; \frac{1}{2\pi} \int_0^\pi \tilde{p}\,[\theta, r\cos(\theta - \phi)]\, d\theta, \qquad\qquad \text{(A.13)}$$

where

$$\tilde{p}(\theta, u) \;\;=\;\; \frac{1}{2\pi} \int_{-\infty}^\infty F_\theta(\omega)|\omega|\,\exp(j\omega u)\, d\omega \;\;=\;\; \mathcal{F}^{-1}\left[F_\theta(\omega)|\omega|\right]. \qquad \text{(A.14)}$$

From Eq. (A.7) and the convolution property of the Fourier transform,

$$\mathcal{F}^{-1}\left[\mathcal{F}[p]\mathcal{F}[h]\right] \;\;=\;\; p * h, \qquad\qquad \text{(A.15)}$$

the inverse Fourier transform in Eq. (A.14) can be viewed as the filtered projection,

$$\tilde{p}(\theta, u) \;\;=\;\; p_\theta(u) * h(u) \;\;=\;\; \int_{-\infty}^\infty p_\theta(u')\, h(u - u')\, du', \qquad \text{(A.16)}$$

where the filtering function is

$$h(u) \;\;=\;\; \mathcal{F}^{-1}\left[|\omega|\right] \;\;=\;\; \frac{1}{2\pi} \int_{-\infty}^\infty |\omega|\,\exp(j\omega u)\, d\omega \qquad \text{(A.17)}$$

Using this technique, the image can be reconstructed by

1. measuring the projections, $p_\theta(u)$, from $\theta = 0$ to $\theta = \pi$;

2. applying the filter $h(u)$ to the the projections using Eq. (A.16) to get $\tilde{p}(\theta, u)$;

3. back projecting $\tilde{p}(\theta, u)$ using Eq. (A.13) to get the image.

A.5 Inverse discrete Radon transformation

With a finite number of equispaced projections, Eq. (A.13) is approximated by the summation

$$f(r, \phi) \quad = \quad \frac{1}{2M} \sum_{i=1}^{M} \tilde{p}\left[\theta_i, r\cos(\theta_i - \phi)\right]. \tag{A.18}$$

This summation is referred as backprojection averaging, since the convoluted projection ($\tilde{p}$) is defined only at a finite number of $\tilde{p}\left[\theta_i, r\cos(\theta_i - \phi)\right]$ at each θ_i needs interpolation.

To reconstruct the 3D structure of the scroll waves in our experiments, we have have utilized the sofeware provided in IDL (IDL: the interactive data language, Research System, Inc.). To reduce noise and enhance the constrast of the reconstruction, a spatial convolution of the observed projections with the Shepp-Logan filter [replacing $|\omega|$ in Eq. (A.17) by $|\omega|\sin(\omega)/(\omega))$] was performed before the images were reconstructed by using the reconstruction procedure "RIEMANN" provided in IDL. The reconstructed image $f(m, n)$, where (m, n) is the discrete position of (x, y), is calculated from the inverse discrete Radon transformation with a linear interpolation:

$$f(m, n) = \Delta\theta \sum_{i} \left[(1 - w)\tilde{p}\left(\theta_i, \lfloor u \rfloor\right) + w\tilde{p}\left(\theta_i, \lfloor u \rfloor + 1\right)\right], \tag{A.19}$$

where

$$w \quad = \quad u - \lfloor u \rfloor, \quad u \quad = \quad \sqrt{2}\left(m\cos\theta_i + n\sin\theta_i\right). \tag{A.20}$$

and $\lfloor \ \rfloor$ indicates flooring to the nearest lower integer.

References

[1] A.M. Turing. The chemical basis of morphogenesis. *Phil. Trans. Roy. Soc. Lond. B*, 237:37–72, 1952.

[2] S. Nettesheim, A. von Oertzen, H.H. Rotermund, and G. Ertl. Reaction diffusion patterns in the catalytic CO-oxidation on Pt(110): Front propagation and spiral waves. *J. Chem. Phys.*, 98:9977–9985, 1993.

[3] A.T. Winfree. Spiral waves of chemical activity. *Science*, 175:634–636, 1972.

[4] J. Lechleiter, S. Girard, E. Peralta, and D. Clapham. Spiral calcium wave propagation and annihilation in *xenopus laevis* oocytes. *Science*, 252:123–126, 1991.

[5] F. Siegert and C.J. Weijer. Digital image processing of optical density wave propagation in *dictyostelium discoideum. J. Cell Sci*, 93:325–335, 1989.

[6] M.A. Dahlem and S.C. Müller. Self-induced splitting of spiral-shaped spreading depression waves in chicken retina. *Exp. Brain Res.*, 115:319–324, 1997.

[7] S.C. Müller, T. Mair, and O. Steinbock. Traveling waves in yeast extract and in cultures of *dictyostelium discoideum. Biophys. Chem.*, 72:37–47, 1998.

[8] U. Storb, C.R. Neto, M. Bär, and S.C. Müller. A tomographic study of desynchronization and complex dynamics of scroll waves in an excitable chemical reaction with a gradient. *Phys. Chem. Chem. Phys.*, 5:2344–2353, 2003.

[9] D. Stock and S.C. Müller. Three-dimensional reconstruction of scroll waves

in the Belousov-Zhabotinsky reaction using optical tomography. *Physica D*, 96:396–403, 1996.

[10] J.P. Keener. The dynamics of three-dimensional scroll waves in excitable media. *Physica D*, 31:269–276, 1988.

[11] J.J. Tyson and S.H. Strogatz. The differential geometry of scroll waves. *Int. J. Bif. Chaos*, 1:723–744, 1991.

[12] J.J. Tyson and J.P. Keener. Spiral waves dynamics. In: Chemical waves and patterns, edited by R. Kapral and K. Showalter. *Kluwer Academic Publishers, London*, pages 93–118, 1994.

[13] A.T. Winfree. Electrical turbulence in three-dimensional heart muscle. *Science*, 266:1003–1006, 1994.

[14] R.A. Gray, A.M. Pertsov, and J. Jalife. Spatial and temporal organization during cardiac fibrillation. *Nature (London)*, 392:75–78, 1998.

[15] F. Fenton and A. Karma. Vortex dynamics in three-dimensional continuous myocardium with fiber rotation: Filament instability and fibrillation. *Chaos*, 8:20–47, 1998.

[16] F. Fenton, E.M. Cherry, H M. Hastings, and S.J. Evans. Multiple mechanisms of spiral wave breakup in a model of cardiac electrical activity. *Chaos*, 12:852–892, 2002.

[17] V.I. Krinsky, V.N. Biktashev, and A.M. Pertsov. Autowave approachs to the cessation of autowave arrhythmias. *Ann. N. Y. Acad. Sci.*, 591:232–246, 1990.

[18] A.S. Mikhailov and K. Showalter. Control of waves, patterns and turbulence in chemical systems. *Phys. Rep.*, 425:79–194, 2006.

[19] F. Fenton. Website. `http://arrhythmia.hofstra.edu`.

[20] A.V. Panfilov and J.P. Keener. Re-entry in three-dimensional Fitzhugh-Nagumo medium with rotational anisotropy. *Physica D*, 84:545–552, 1995.

[21] W.J. Rappel. Filament instability and rotational tissue anisotropy: A numerical study using detailed cardiac models. *Chaos*, 11:71–80, 2001.

[22] F. Fenton and A. Karma. Fiber-rotation-induced vortex turbulence in thick myocardium. *Phys. Rev. Lett.*, 81:481–484, 1998.

[23] S. Setayeshgar and A.J. Bernoff. Scroll waves in the presence of slowly varying anisotropy with application to the heart. *Phys. Rev. Lett.*, 88:028101, 2002.

[24] J.N. Weiss, Z. Qu, P. Chen, S. Lin, H. S. Karagueuzian, H. Hayashi, A. Garfinkel, and A Karma. The dynamics of cardiac fibrillation. *Circulation*, 112:1232–1240, 2005.

[25] D. Barkley. A model for fast computer simulation of waves in excitable media. *Physica D*, 49:61–70, 1991.

[26] M. Dowle, R.M. Mantel, and D. Barkley. Fast simulations of waves in three-dimensional excitable media. *Int. J. Bif. Chaos*, 7:2529–2545, 1997.

[27] R. FitzHugh. Impulses and physiological states in theoretical models of nerve membrane. *Biophys. J.*, 1:445–466, 1961.

[28] J. Nagumo, S. Arimoto, and S. Yoshikawa. An active pulse transmission line simulating nerve axon. *Proc IRE.*, 50:2061–2070, 1962.

[29] J.M. Flesselles, A. Belmonte, and V. Gáspár. Dispersion relation for waves in the Belousov-Zhabotinsky reaction. *J. Chem. Soc. Faraday Trans.*, 94:851–855, 1998.

[30] A.F. Taylor, V. Gáspár, B. R. Johnson, and S.K. Scott. Analysis of reaction-diffusion waves in the ferroin-catalysed Belousov-Zhabotinsky reaction. *Phys. Chem. Chem. Phys.*, 1:4595–4599, 1999.

[31] V.S. Zykov. Analytical evaluation of the dependence of the speed of an excitation wave in a two-dimension excitable medium on the curvature of its front. *Biophysics*, 25:906–911, 1980.

[32] J.P. Keener and J.J. Tyson. Spiral waves in the Belousov-Zhabotinskii reaction. *Physica D*, 21:307–324, 1986.

[33] P. Foerster, S.C. Müller, and B. Hess. Curvature and propagation velocity of chemical waves. *Science*, 241:685–687, 1988.

[34] J.J. Tyson and J.P. Keener. Singular perturbation theory of traveling waves in excitable media. *Physica D*, 32:327–361, 1988.

[35] B.P. Belousov. A periodic reaction and its mechanism, In Sbornik Referatov po Radiatsionni Meditsine. *Moscow: Medgiz*, pages 145–147, 1958.

[36] A.M. Zhabotinsky. Periodic process of the oxidation of malonic acid in solution (study of the kinetics of Belosouv's reaction). *Biofizika*, 9:306–311, 1964.

[37] L. Kuhnert. Photochemische Manipulation von chemischen Wellen. *Naturwissenschaften*, 73:96–97, 1986.

[38] M. Jinguji, M. Ishihara, and T. Nakazawa. Primary process of illumination effect on the $Ru(bpy)_3SO_4$-catalyzed Belousov-Zhabotinsky reaction. *J. Phys. Chem.*, 96:4279–4281, 1992.

[39] R.J. Field, E. Körös, and R.M. Noyes. Oscillations in chemical systems. II. Thorough analysis of temporal oscillations in the bromate-cerium-malonic acid system. *J. Am. Chem. Soc.*, 94:8649–8664, 1972.

[40] R.J. Field and R.M. Noyes. Oscillations in chemical systems. IV. Limit cycle behavior in a model of a real chemical reaction. *J. Chem. Phys.*, 60:1877–1884, 1974.

[41] J.J. Tyson and P.C. Fife. Target patterns in a realistic model of the Belousov-Zhabotinsky reaction. *J. Chem. Phys.*, 73:2224–2237, 1980.

[42] S.C. Müller, T. Plesser, and B. Hess. The structure of the core of the spiral wave in the Belousov-Zhabotinsky reaction. *Science*, 230:661–663, 1985.

[43] T. Plesser, S.C. Müller, and B. Hess. Spiral wave dynamics as a function of proton concentration in the ferroin-catalyzed Belousov-Zhabotinsky reaction. *J. Phys. Chem.*, 94:7501–7507, 1990.

[44] G.S. Skinner and H.L. Swinney. Periodic to quasiperiodic transition of chemical spiral rotation. *Physica D*, 48:1–16, 1991.

[45] Zs. Nagy-Ungvárai, J. Ungvárai, and S.C. Müller. Complexity in spiral wave dynamics. *Chaos*, 3:15–19, 1993.

[46] G. Li, Q. Ouyang, V. Petrov, and H.L. Swinney. Transition from simple rotating chemical spirals to meandering and traveling spirals. *Phys. Rev. Lett.*, 77:2105–2108, 1996.

[47] N. Manz, B.T. Ginn, and O. Steinbock. Meandering spiral waves in the 1,4-cyclohexanedione Belousov-Zhabotinsky system catalyzed by $Fe[batho(SO_3)_2]_3^{4-/3-}$. *J. Phys. Chem. A*, 107:11008–11012, 2003.

[48] C. Luengviriya, U. Storb, M.J.B. Hauser, and S.C. Müller. An elegant method to study an isolated spiral wave in a thin layer of a batch Belousov-Zhabotinsky reaction under oxygen-free conditions. *Phys. Chem. Chem. Phys.*, 8:1425–1429, 2006.

[49] V.S. Zykov. *Simulation of Wave Processes in Excitable Media.* Manchester University Press, Manchester, 1987.

[50] S. Grill, V. S. Zykov, and S.C. Müller. Spiral wave dynamics under pulsatory modulation of excitability. *J. Phys. Chem.*, 100:19082–19088, 1996.

[51] A.T. Winfree. Scroll-shaped waves of chemical activity in three dimensions. *Science*, 181:937–939, 1973.

[52] S.C. Müller and T. Plesser. Spiral waves dynamics. In: Chemical waves and patterns, edited by R. Kapral and K. Showalter. *Kluwer Academic Publishers, London*, pages 57–92, 1994.

[53] A.T. Winfree. Varieties of spiral wave behavior: An experimentalist's approach to the theory of excitable media. *Chaos*, 1:303–334, 1991.

[54] A.T. Winfree, S. Caudle, G. Chen, P. McGuire, and Z. Szilagyi. Quantitative optical tomography of chemical waves and their organizing centers. *Chaos*, 6:617–626, 1996.

[55] T. Bánsági and O. Steinbock. Nucleation and collapse of scroll rings in excitable media. *Phys. Rev. Lett.*, 97:198301, 2006.

[56] W. Jahnke, W.E. Skaggs, and A.T. Winfree. Chemical vortex dynamics in the Belousov-Zhabotinsky reaction and in the two-variable oregonator model. *J. Phys. Chem.*, 93:740–749, 1989.

[57] W. Jahnke and A.T. Winfree. A survey of spiral wave behaviors in the oregonator model. *Int. J. Bif. Chaos*, 1:445–466, 1991.

[58] S. Alonso, F. Sagués, and A.S. Mikhailov. Negative tension instability of scroll waves and Winfree turbulence in the Oregonator model. *J. Phys. Chem. A*, 110:12063–12071, 2006.

[59] D. Barkley. Spiral-wave dynamics in a simple model of excitable media: The transition from simple to compound rotation. *Phys. Rev. A*, 42:2489–2492, 1990.

[60] D. Barkley. Linear stability analysis of rotating spiral waves in excitable media. *Phys. Rev. Lett.*, 68:2090–2093, 1992.

[61] D. Barkley. Euclidean symmetry and the dynamics of rotating spiral waves. *Phys. Rev. Lett*, 72:164–167, 1994.

[62] D. Barkley. Spiral waves dynamics. In: Chemical waves and patterns, edited by R. Kapral and K. Showalter. *Kluwer Academic Publishers, London*, pages 163–189, 1994.

[63] R. Feeney, S. L. Schmidt, and P. Ortoleva. Experiments on electric field-BZ chemical wave interactions: Annihilation and the crescent wave. *Physica D*, 2:536–544, 1981.

[64] H. Ševčíková and M. Marek. Chemical waves in electric field. *Physica D*, 9:140–156, 1983.

[65] M. Pornprompanya, S.C. Müller, and H. Ševčíková. Pulse waves under an electric field in the Belousov-Zhabotinsky reaction with pyrogallol as substrate. *Phys. Chem. Chem. Phys.*, 4:3370–3375, 2002.

[66] H. Ševčíková, J. Kosek, and M. Marek. Splitting of 2D waves of excitation in a direct current electric field. *J. Phys. Chem.*, 100:1666–1675, 1996.

[67] H. Ševčíková, M. Marek, and S.C. Müller. The reversal and splitting of waves in an excitable medium caused by an electrical field. *Science*, 257:951–954, 1992.

[68] M. Pornprompanya, H. Ševčíková, and S.C. Müller. Multiple reversals of pulse waves in an excitable medium resulting from switching the polarity of dc electric field. *Chem. Phys. Lett.*, 375:364–368, 2003.

[69] V. Pérez-Muñuzuri, R. Aliev, B. Vasiev, and V.I. Krinsky. Electric current control of spiral wave dynamics. *Physica D*, 56:229–234, 1992.

[70] B. Schmidt and S.C. Müller. Forced parallel drift of spiral waves in the Belousov-Zhabotinsky reaction. *Phys. Rev. E*, 55:4390–4393, 1997.

[71] O. Steinbock, J. Schütze, and S.C. Müller. Electric-field-induced drift and deformation of spiral waves in an excitable medium. *Phys. Rev. Lett.*, 68:248–251, 1992.

[72] V. Pérez-Muñuzuri, B. Vasiev, V. Pérez-Villar, and V.I. Krinsky. Super-spiral structure in excitable media. *Nature*, 353:740–742, 1991.

[73] K.I. Agladze and P. De Kepper. Influence of electric field on rotating spi-ral waves in Belousov-Zhabotinsky reaction. *J. Phys. Chem.*, 96:5239–5242, 1992.

[74] A.P. Muñuzuri, V.A. Davydov, V. Pérez-Muñuzuri, M. Gómez-Gesteira, and V. Pérez-Villar. General properties of the electric-field-induced vortex drift in excitable media. *Chaos, Solitons & Fractals*, 7:585–595, 1996.

[75] J. Schütze, O. Steinbock, and S.C. Müller. Forced vortex interaction and annihilation in an active medium. *Nature*, 356:45–46, 1992.

[76] A.P. Muñuzuri, M. Gómez-Gesteira, V. Pérez-Muñuzuri, V.I. Krinsky, and V. Pérez-Villar. Mechanism of the electric-field-induced vortex drift in ex-citable media. *Phys. Rev. E*, 48:R3232–R3235, 1993.

[77] V. Krinsky, E. Hamm, and V. Voignier. Dense and sparse vortices in excitable media drift in opposite directions in electric field. *Phys. Rev. lett*, 76:3854–3857, 1996.

[78] H. Henry. Spiral wave drift in an electric field and scroll wave instabilities. *Phys. Rev. E*, 70:026204, 2004.

[79] J.J. Taboada, A.P. Muñuzuri, V. Pérez-Muñuzuri, M. Gómez-Gesteira, and V. Pérez-Villar. Spiral breakup induced by an electric current in a Belousov-Zhabotinsky medium. *Chaos*, 4:519–524, 1994.

[80] O. Kheowan and S.C. Müller. Control of spiral waves in excitable media. *J. Appl. Math. Comp.*, 164:373–390, 2005.

[81] S. Grill, V. S. Zykov, and S.C. Müller. Feedback-controlled dynamics of meandering spiral waves. *Phys. Rev. Lett.*, 75:3368–3371, 1995.

[82] O. Kheowan, C. Chan, V.S. Zykov, O. Rangsiman, and S.C. Müller. Spiral wave dynamics under feedback derived from a confined circular domain. *Phys. Rev. E*, 64:03520, 2001.

[83] S. Naknaimueang, M.A. Allen, and S.C. Müller. Spiral wave dynamics under feedback via an equilateral triangular sensory domain. *Phys. Rev. E*, 74:066209, 2006.

[84] A.T. Winfree and S.H. Strogatz. Singular filaments organize chemical waves in three dimensions: I. Geometrically simple waves. *Physica D*, 8:35–49, 1983.

[85] A.T. Winfree and S.H. Strogatz. Singular filaments organize chemical waves in three dimensions: II. Twisted waves. *Physica D*, 9:65–80, 1983.

[86] A.T. Winfree and S.H. Strogatz. Singular filaments organize chemical waves in three dimensions: III. Knotted waves. *Physica D*, 9:333–345, 1983.

[87] A.T. Winfree and S.H. Strogatz. Singular filaments organize chemical waves in three dimensions : IV. Wave taxonomy. *Physica D*, 13:221–233, 1984.

[88] A.T. Winfree and S.H. Strogatz. Organizing centres for three-dimensional chemical waves. *Nature*, 311:611–615, 1984.

[89] A.V. Panfilov and A.N. Rudenko. Two regimes of the scroll ring drift in the three-dimensional active media. *Physica D*, 28D:215–218, 1987.

[90] S. Alonso and A.V. Panfilov. Negative filament tension in the Luo-Rudy model of cardiac tissue. *Chaos*, 17:015102, 2007.

[91] H. Henry and V. Hakim. Scroll waves in isotropic excitable media: Linear instabilities, bifurcations and restabilized states. *Phys. Rev. E*, 65:046235, 2002.

[92] S. Alonso, R. Kähler, A.S. Mikhailov, and F. Sagués. Expanding scroll rings and negative tension turbulence in a model of excitable media. *Phys. Rev. E*, 70:056201, 2004.

[93] C. Henze, E. Lugosi, and A.T. Winfree. Helical organizing centers in excitable media. *Can. J. Phys.*, 68:683–710, 1990.

[94] B. Echebarria, H. Henry, and V. Hakim. Nonequilibrium ribbon model of twisted scroll waves. *Phys. Rev. Lett*, 93:098301, 2006.

[95] B.J. Welsh and J. Gomatam. Diversity of three-dimensional chemical waves. *Physica D*, 43:304–317, 1990.

[96] A.M. Pertsov, R.R. Aliev, and V.I. Krinsky. Three-dimensional twisted vortices in an excitable chemical medium. *Nature*, 345:419–421, 1990.

[97] S. Mironov, M. Vinson, S. Mulvey, and A.M. Pertsov. Destabilization of three-dimensional rotating chemical waves in an inhomogeneous BZ reaction. *J. Phys. Chem.*, 100:1975–1983, 1996.

[98] T. Bánsági and O. Steinbock. Negative filament tension of scroll rings in an excitable system. *Phys. Rev. E*, 76:045202(R), 2007.

[99] V.N. Biktashev, A.V. Holden, and H. Zhang. Tension of organizing filaments of scroll waves. *Phil. Trans. R. Soc. Lond. A*, 347:611–630, 1994.

[100] S. Alonso, F. Sagués, and A.S. Mikhailov. Taming Winfree turbulence of scroll waves in excitable media. *Science*, 299:1722–1725, 2003.

[101] W. Jahnke, C. Henze, and A.T. Winfree. Chemical vortex dynamics in three-dimensional excitable media. *Nature*, 336:662–665, 1988.

[102] K.I. Agladze, R.A. Kocharyan, and V.I. Krinsky. Direct observation of vortex ring collapse in a chemically active medium. *Physica D*, 49:1–4, 1991.

[103] M. Vinson, S. Mironov, S. Mulvey, and A.M. Pertsov. Control of spatial orientation and lifetime of scroll rings in excitable media. *Nature*, 386:477–480, 1997.

[104] H. Henry and V. Hakim. Linear stability of scroll waves. *Phys. Rev. Lett*, 85:5328–5331, 2000.

[105] I. Aranson and I. Mitkov. Helicoidal instability of a scroll vortex in three-dimensional reaction-diffusion systems. *Phys. Rev. E*, 54:4556–4559, 1998.

[106] A. Rusakov, A.B. Medvinsky, and A.V. Panfilov. Scroll waves meandering in a model of an excitable medium. *Phys. Rev. E*, 72:022902, 2005.

[107] R.R. Aliev and A.V. Panfilov. A simple two-variable model of cardiac excitation. *Chaos, Solitons & Fractals*, 7:293–301, 1996.

[108] V.N. Biktashev. Evolution of twist of an autowave vortex. *Physica D*, 36:167–172, 1989.

[109] J. Ungvárai and Zs. Nagy-Ungvárai. Effect of oxygen on the dispersion relation of BZ waves. *Models in Chem.*, 135:393–400, 1998.

[110] A.F. Taylor, B.R. Johnson, and S.K. Scott. Effect of oxygen on wave propagation in the ferroin-catalysed Belousov-Zhabotinsky reaction. *J. Chem. Soc., Faraday Trans.*, 94:1029–1033, 1998.

[111] M. Vinson and A.M. Pertsov. Dynamics of scroll rings in a parameter gradient. *Phys. Rev. E*, 59:2764–2771, 1999.

[112] R.R. Aliev and A.B. Rovinsky. Spiral waves in the homogeneous and inhomogeneous Belousov-Zhabotinsky reaction. *J. Phys. Chem.*, 96:732–736, 1992.

[113] T. Amemiya, P. Kettunen, S. Kádár, T. Yamaguchi, and K. Showalter. Formation and evolution of scroll waves in photosensitive excitable media. *Chaos*, 8:872–878, 1998.

[114] T. Amemiya, S. Kádár, P. Kettunen, and K. Showalter. Spiral wave formation in three-dimensional excitable media. *Phys. Rev. Lett*, 77:3244–3247, 1996.

[115] A.T. Winfree. Numerical and chemical experiments on filament motion. In: Spatio-temporal organization in non-equilibrium systems edited by S.C. Müller and T. Plesser. *Projekt-Verlag, Dortmund*, pages 270–273, 1992.

[116] W. Lorensen and H. Cline. Marching cubes: A high resolution 3D surface construction algorithm. *Comput. Graph.*, 21:163–169, 1987.

[117] H. Cline, W. Lorensen, S. Ludke, C. Crawford, and B. Teeter. 2 algorithms for the 3-dimensional reconstruction of tomograms. *Med. Phys.*, 15:320–327, 1988.

[118] C. Montani, R. Scateni, and R. Scopigno. A modifed look-up table for implicit disambiguation of marching cubes. *Visual Comput.*, 10:353–355, 1994.

[119] C. Luengviriya, U. Storb, G. Lindner, S.C. Müller, M. Bär, and M.J.B. Hauser. Scroll wave instabilities in an excitable chemical medium. *Phys. Rev. Lett.*, 100:148302, 2008.

[120] P.M. Wood and J. Ross. A quantitative study of chemical waves in the Belousov-Zhabotinsky reaction. *J. Chem. Phys.*, 82:1924–1936, 1985.

[121] A.M. Pertsov, M. Vinson, and S.C. Müller. Three-dimensional reconstruction of organizing centers in excitable chemical media. *Physica D*, 63:233–240, 1993.

[122] A.V. Panfilov, A.N. Rudenko, and V.I. Krinskii. Vortical rings in three-dimensional active media with diffusion over two components. *Biofizika*, 31:850–854, 1986.

[123] J.P. Keener and J.J. Tyson. The dynamics of scroll waves in excitable media. *SIAM Rev.*, 34:1–39, 1992.

[124] A.G. Lindgren and P.A. Rattey. The inverse discrete radon transform with applications to tomographic imaging using projection data. *Adv. Electron. Electron Phys.*, 56:359–410, 1981.

Curriculum Vitae

Personal Details

Name:	Chaiya Luengviriya
Date of Birth:	15 February 1973
Place of Birth:	Bangkok, Thailand
Nationality:	Thai

School education

1986–1988:	Upper Primary school, Wat Putthabucha, Bangkok, Thailand
1989–1991:	Upper Secondary school, Bangmodwittaya, Bangkok, Thailand

University education

1992-1999:	Study of physics: Kasetsart University, Bangkok, Thailand
1996:	Bachelor of Science (Physics)
1999:	Master of Science (Physics)
	Title of thesis : The gap ratio of the d-wave superconductors
1999-2002:	Lecturer, Physics Department, Kasetsart University, Bangkok, Thailand
2002-2008:	Ph.D. project: Biophysics Group, Otto-von-Guericke University, Magdeburg, Germany
	Title of thesis : Dynamics of three-dimensional excitation waves